High Resolution Electron Microscopy of Biological Systems

Miriam Dowle

A thesis submitted to
the University of Birmingham for the
degree of DOCTOR OF PHILOSOPHY

Physical Sciences of Imaging for the Biomedical
Sciences (PSIBS) Doctoral Training Centre
University of Birmingham

June 2014

Abstract

This thesis demonstrates the relevance of advanced transmission electron microscopy (TEM) techniques such as aberration corrected scanning transmission electron microscopy (STEM) to the study of biological samples. By developing the application of these techniques to biologically relevant systems, this study shows how advanced EM can be an effective tool by providing insight into the structure of biological systems at the highest (i.e. atomic) resolutions.

High angle annular dark field (HAADF) STEM has been used to gain insight into the core structure and iron loading mechanisms of the iron storage protein, ferritin. The iron content of ferritin was quantified using size-selected gold clusters as a mass balance, the first application of this technique to a biological sample.

Preliminary structural studies of a novel colorectal cancer therapy have been undertaken, where polymeric alginate molecules chelate chemotoxic luminal iron in the colon. In particular the nano-structures built when alginates bind iron under physiological conditions have been established and investigated for the first time, using HAADF-STEM.

Finally using TEM, it has been revealed for the first time the structures formed, and morphology changes induced, when proteins are encapsulated by membrane mimicking nano-discs.

Acknowledgements

I would like to thank the following people:

My supervisors, Prof Richard Palmer, Prof Michael Overduin, Dr Martyn Chidgey and Prof Roy Johnston for their guidance and support throughout this project. Prof Mike Hannon, Prof Chris Thomas and Dr Josephine Bunch for continued support through PSIBS.

Dr Zhi Wei Wang, who provided me with my initial STEM training and many interesting discussions, for which I am truly grateful. Dr Kenton Arkill, who improved my image analysis understanding tremendously and provided invaluable support towards the end of my PhD. Dr Feng Yin and Ray Hu who both prepared the size-selected clusters used in the work presented in Chapter 4 and Dr Ziyou Li for many useful discussions.

Dr Chris Tselepsis and Prof Zoe Pikramenou, for their collaboration towards the work presented in Chapter 5. Richard Horniblow, who not only prepared samples for analysis but also took time to (very patiently) explain his work.

Dr Tim Knowles not only for sample preparation, but also useful discussion and support throughout the work presented in Chapter 6. Dr Thomas Sharp and Judith Mantell at the University of Bristol for demonstrating TEM, cryo-TEM and biological preparation techniques.

All the students and staff of NPRL and PSIBS not only for support with science but also regular coffee breaks. In particular, Ruth Chantry, Penelope Rodriguez-Zamora, Dongsheng He, Tian Pan, Andrew Palmer, Rory Steven, Jamie Guggenheim, Hector Basevi, Richard Williams, Alan Race, James Brown, Ting Yue and Laura Rowley.

Finally, I would like to thank my friends and family, for everything.

Contents

Author Contributions

The author performed all the electron microscopy imaging and analysis presented in this thesis. The author also prepared all the specimens for imaging using the various methods described, and wrote this thesis in its entirety.

The size-selected clusters used in Chapter 4 were prepared by Dr Feng Yin and Ray Hu from the Nanoscale Physics Research Laboratory (NPRL), University of Birmingham.

All biological material preparation for the Alginate work in Chapter 5 was performed by Richard Horniblow (RH) from the School of Cancer Sciences, University of Birmingham. The confocal microscopy and circular dichroism results included for reference were also performed by RH.

All biological materials preparation for the SMALPs work in Chapter 6 was performed by Dr Tim Knowles from the School of Cancer Sciences, University of Birmingham.

List of Figures

List of Abbreviations

EM	Electron Microscopy
STEM	Scanning Transmission Electron Microscopy
SEM	Scanning Electron Microscopy
TEM	Transmission Electron Microscopy
HAADF	High Angle Annular Dark Field
BF	Bright Field
FEG	Field Emission Gun
EELS	Electron Energy Loss Spectroscopy
EDX	Energy Dispersive X-ray Spectroscopy
SAXS	Small Angle X-ray Spectroscopy
NMR	Nuclear Magnetic Resonance
DLS	Dynamic Light Scattering
CD	Circular Dichroism
AFM	Atomic Force Microscopy
MRI	Magnetic Resonance Imaging
DI	De-ionised
SMALP	Styrene Maleic Acid Lipid Particle

Chapter 1

Introduction

In the biological sciences, understanding the function of a system often first requires understanding the structure. With electron microscopy [1] it is possible to image structures down to atomic precision. This thesis addresses the broad theme of developing the use of high resolution electron microscopy for investigating structure in biological systems, focusing on three different biological examples:

1. the iron storage protein ferritin
2. iron-chelating alginates for bowel cancer therapy
3. nano-discs encapsulating membrane proteins

These three systems all function on the nano-metre scale and control the environment around them, thus, gaining additional understanding of their structure at the sub-nanometre scale will provide significant advantages in developing routes to manipulating biological systems at the nanoscale.

The human body's ability to manage the supply of iron is an essential biological process, into which much research has taken place [2, 3]. The first system, ferritin, is a natural protein which manages iron storage in the body [4], whereas the second, based on alginates, is an artificial solution currently in development to sequester free luminal iron in the bowel and thus reduce

the risk of bowel cancer, the second biggest cause of cancer mortality in the UK [5]. Both systems work to encapsulate free iron into aggregates at the nano-scale to regulate the surrounding environment; iron chelating alginates are being developed into a future drug therapy for bowel cancer, with initial clinical trials in the planning stage. Drug development is also the key focus for the third system. The solubilisation of membrane proteins is a key process in drug design, as they make up the majority of conventional drug targets [6]. The nano-disc method of capture [7], which simulates a membrane environment, is therefore a useful step towards simplifying the initial development process.

In terms of the structure of the rest of this thesis, first a general background chapter is presented (Chapter 2), covering electron microscopy applied to biological molecules and advanced techniques within the field. This is then followed by an experimental techniques chapter (Chapter 3), giving details of the equipment, sample preparation techniques and data analysis protocols used to acquire the results presented. The three subsequent results chapters (Chapters 4-6) each contain an introduction and literature review concerning the relevant biological topic, followed by the results obtained and their interpretation. The last chapter (Chapter 7) summarises the conclusions of the work as a whole with a focus on the principal results and further experimental work that could be carried out in the future. A separate list of references is included at the end of each chapter containing the relevant literature for that particular area.

References

[1] A. A. Sousa and R. D. Leapman. Development and application of STEM for the biological sciences. *Ultramicroscopy*, 2012.

[2] R. L. Nelson. Iron and colorectal cancer risk: human studies. *Nutrition reviews*, 59(5):140–148, 2001.

[3] J. F. Collingwood, A. Mikhaylova, M. Davidson, C. Batich, W. J. Streit, J. Terry, and J. Dobson. In situ characterization and mapping of iron compounds in alzheimer's disease tissue. *Journal of Alzheimer's Disease*, 7(4):267–272, 2005.

[4] G. C. Ford, P. M. Harrison, D. W. Rice, J. M. A. Smith, A. Treffry, J. L. White, and J. Yariv. Ferritin: design and formation of an iron-storage molecule. *Philosophical Transactions of the Royal Society of London. B, Biological Sciences*, 304(1121):551–565, 1984.

[5] A. Jemal, F. Bray, M. M. Center, J. Ferlay, E. Ward, and D. Forman. Global cancer statistics. *CA: a cancer journal for clinicians*, 61(2):69–90, 2011.

[6] A. M. Seddon, P. Curnow, and P. J. Booth. Membrane proteins, lipids and detergents: not just a soap opera. *Biochimica et Biophysica Acta (BBA)-Biomembranes*, 1666(1):105–117, 2004.

[7] T.J. Knowles, R. Finka, C. Smith, Y.P. Lin, T. Dafforn, and M. Overduin. Membrane proteins solubilized intact in lipid containing nanoparticles bounded by styrene maleic acid copolymer. *Journal of the American Chemical Society*, 131(22):7484–7485, 2009.

Chapter 2

Background

In this chapter, electron microscopy as a tool for imaging biological samples at the highest resolution will be introduced. The challenges associated with biological samples will also be discussed along with the advanced techniques used in this research.

'Biological imaging' encompasses a wide range of techniques that rely on a number of physical phenomena. These range in application from medical diagnostic tools such as X-ray, magnetic resonance imaging (MRI) [1] and positron emission tomography (PET) [2], to functional analysis of 'live' organisms using fluorescence microscopy [3]. More detailed structural determination by nuclear magnetic resonance (NMR) [4], atomic force microscopy (AFM) [5] and X-ray diffraction [6] can also be performed. Electron microscopy can resolve fixed structures on an atomic scale and is often complementary to other techniques, for example the movement of molecules within a cellular environment can be monitored using light microscopy and then the detailed structure of the molecule itself can be interrogated using electron microscopy. Electron microscopy offered some of the first insights into cell architecture [7, 8] - a pivotal moment in the understanding of biological systems that has laid the way for many more discoveries [9].

Figure 2.1 shows an electron micrograph presented in one of the early papers discussing electron microscopy sample preparation procedures by Palade *et. al.* [8]. This rat liver cell section was

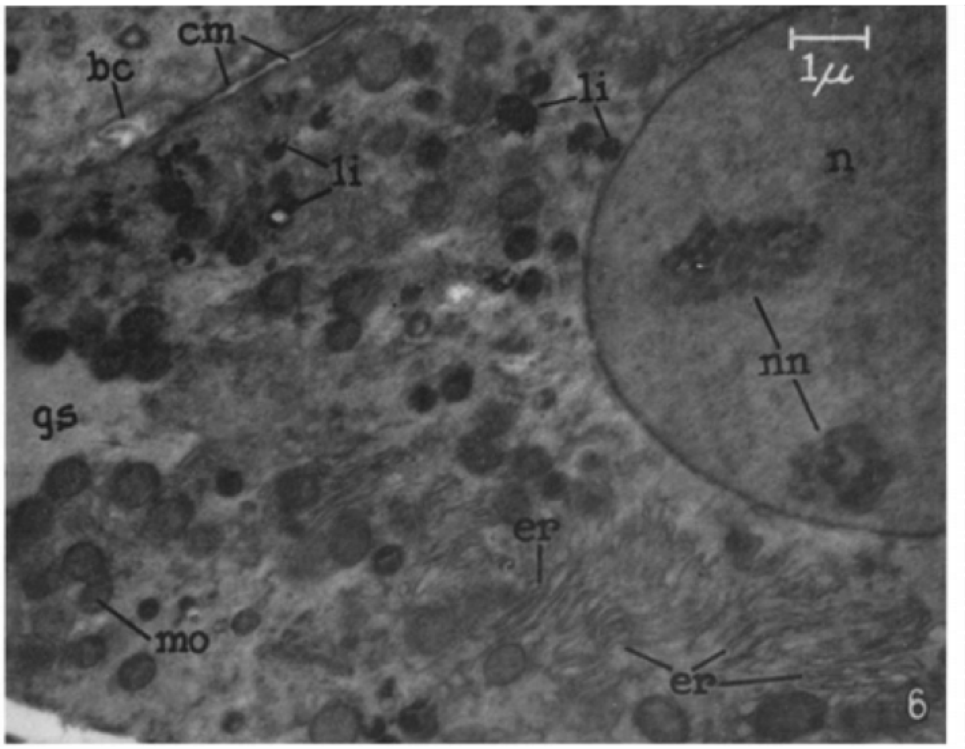

Figure 2.1: This figure, reproduced from [8], reveals rat liver cell architecture using an TEM. Tissue blocks were fixed with osmium and sectioned with a glass knife. The nucleus (n), lipid inclusions (li), mitochondria (mo), bile capillary (bc), elongated structures (er), ground substance (gs) and cell membrane (cm) are all highlighted.

prepared by fixing small blocks of tissue in osmium and then slicing using a glass knife. The images were taken at 3,000 X magnification using a transmission electron microscope (TEM) and recorded on a plate. Images could then be enlarged post acquisition. In the figure, several key features of the rat liver architecture are highlighted. The nucleus (n), lipid inclusions (li), mitochondria (mo), bile capillary (bc), elongated structures (er), ground substance (gs) and cell membrane (cm) can all be localised. Such images provided much more detailed information about structures previously only visualised with light microscopy.

For comparison, in figure 2.2 a high resolution electron microscopy image is presented, in which single atoms can be identified. This is a scanning transmission electron microscope (STEM) image of galium nitride with false colour added to highlight the different intensities within the

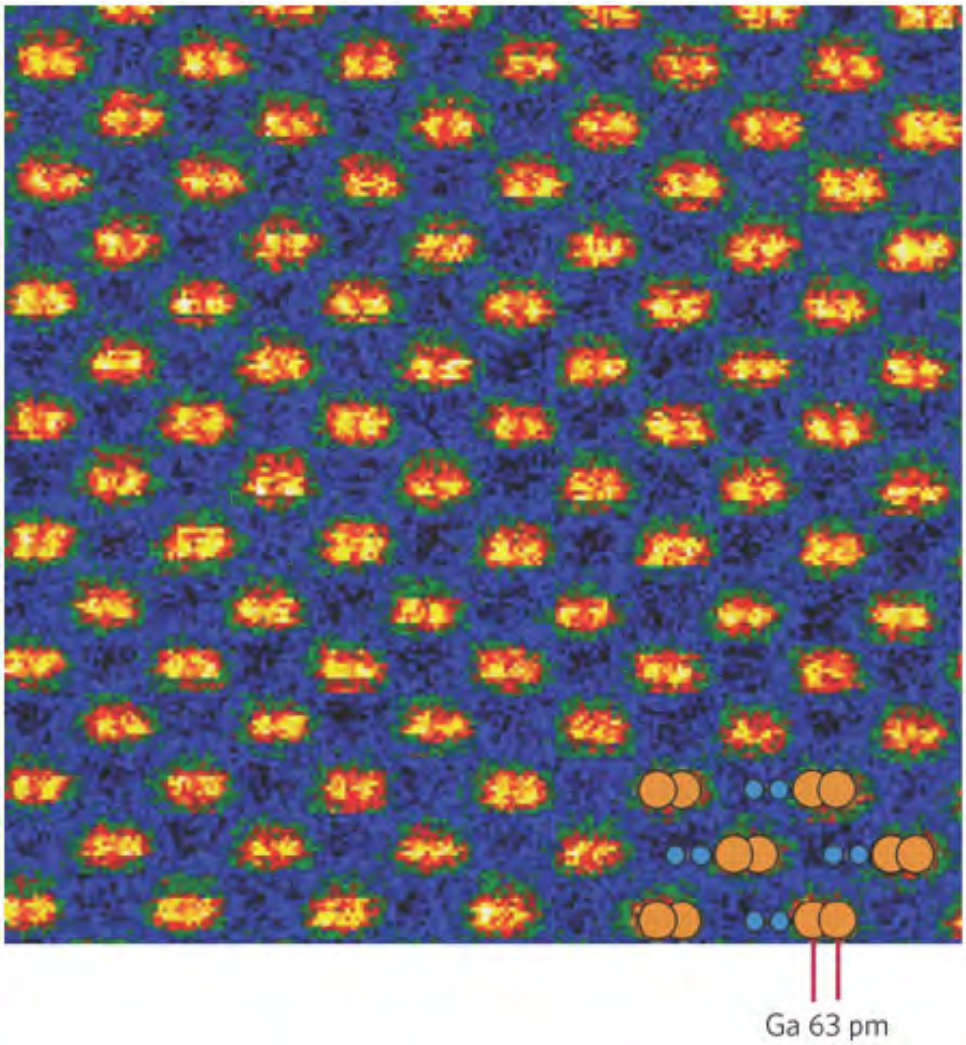

Figure 2.2: This figure reproduced from [10] reveals sub angstrom level electron microscopy of GaN. A separation of 0.63 nm between the Ga atoms is highlighted, the small blue circles highlight the N atoms.

image. It is useful to compare the scale bars between figure 2.2 and 2.1 in order to see how far the technique has advanced in terms of resolution. This ultra-high resolution image is captured with digital sensors and benefits from the correction of spherical aberration in the imaging system. This thesis seeks the advantages that may be gained from applying these advances to the investigation of structure in biological systems. In this chapter the techniques used in this study will be discussed, along with the background of the development of the field and the current state of the art.

2.1 Imaging with Electrons

The rayleigh criterion for light microscopy states that the smallest distance that can be measured (ie. the maximum resolution), δ is

$$\delta = \frac{0.61\lambda}{\mu sin\beta} \tag{2.1}$$

where λ is the wavelength of the incident radiation, μ is the refractive index of the viewing medium and β is the semi angle of collection of the magnifying lens [11]. Since $\mu sin\beta$ can be equated to unity in a visible light microscope, the smallest distance that can be measured is 0.61λ. In the early 20^{th} century, Louis de Broglie suggested that electrons had wave-like characteristics, with electron wavelength (λ, nm) related to its energy (E, eV), via

$$\lambda = \frac{1.22}{E^{1/2}} \tag{2.2}$$

For example, for a 200keV electron, λ = 0.0025nm, which is smaller than the diameter of an atom. The smallest theoretical distance that can be resolved by an electron microscope, δ, is

$$\delta = \frac{1.22\lambda}{\beta} \tag{2.3}$$

So, it follows that if electrons are used as the imaging radiation, a microscope capable of mea-

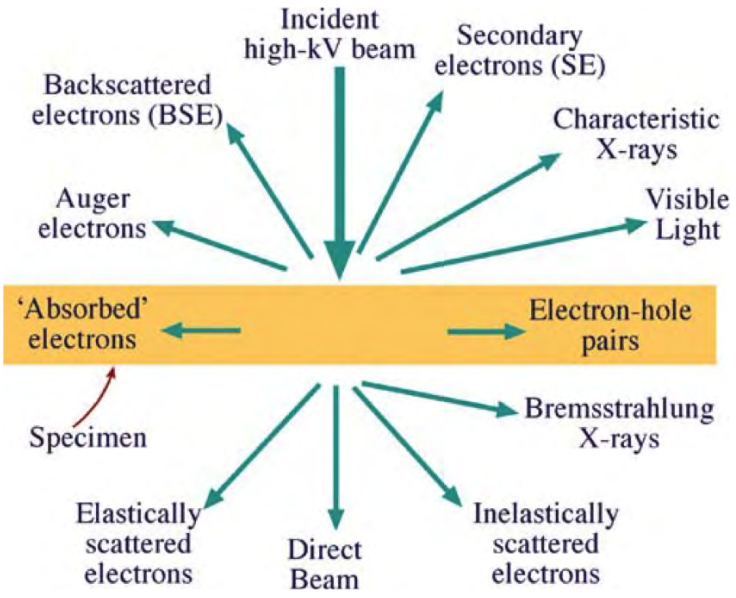

Figure 2.3: Electrons can interact with matter in a variety of different ways, methods have been developed to analyse the various signals which can broadly be divided into two, those that are transmitted through the sample and those that scatter back from the sample. (Figure reproduced from [11])

suring distances on an atomic scale is possible [11]. In 1932, Knoll and Ruska developed the first electron microscope [12].

Electrons interact with matter via several pathways, a schematic of which can be seen in figure 2.3. When an electron source is directed at a specimen, the different electron interactions and the signals resulting from them can provide complementary information about a sample, and different methods have been developed to take advantage of this. The two principle techniques are scanning electron microscopy (SEM) and transmission electron microscopy (TEM). Broadly, SEM analyses the signals that are emitted from the surface of the specimen and TEM analyses those that are transmitted through the specimen.

In the work presented in this thesis, the principal electron microscopic technique used is TEM. This can achieve higher resolution imaging than SEM, but requires more rigorous sample preparation in that any sample must be thin enough for a sufficient number of electrons to pass through

the sample. The principles of TEM are discussed in more detail in the following sections.

A third variation of electron microscope has been developed, based on transmitted electrons, called the scanning transmission electron microscope (STEM) and was first introduced in the early 1970s by Crewe *et. al.* [13]. Instead of a broad, stationary beam, the electron beam is scanned across the sample and the transmitted, scattered electrons detected pixel-by-pixel with scintillators located below the sample in the microscope column. The smaller probe size allows smaller samples to be interrogated and Crewe *et. al.* demonstrated its potential by imaging single heavy atoms on a carbon substrate for the first time.

In STEM two main signals are detected, the 'dark' and 'bright' field. The dark field signal is derived from electrons that interact with atoms in the sample and are scattered with a high angle, this scattering is proportional to the atomic number (z) of the sample and so is also known as z-contrast imaging. The scattered electrons are collected by an annular detector sitting below the sample, hence the technique being called annular dark field (ADF) and if the collection angles are large enough, high angle annular dark field (HAADF). The electrons that are scattered to small forward angles travel through to the bright field (BF) detector that sits in the middle of the annular detector. The STEM was originally intended for the biological sciences as a 'mass mapper' [13] but it has mainly been utilised for imaging the high atomic number samples common in the material sciences. Its popularity has further increased with the advent of aberration correction which has improved the resolution to, in some cases, sub angstrom ranges [14]. This is discussed in more detail in section 2.3.3.

Before discussing the advanced techniques such as aberration corrected STEM utilised in the work presented in this thesis, conventional biological electron microscopy and the sample preparation associated with it will be discussed in order to provide contextual background to the work.

2.2 Conventional Biological TEM

There are three major challenges inherent in analysing biological material in an electron microscope [15]:

1. Biological samples are electron senstive, and easily damaged by a high-energy electron beam

2. Electrons are weakly scattered from the light elements (C, N, O) that make up the vast majority of biological samples

3. Biological samples cannot 'survive' within the high-vacuum conditions of an electron microscope

Despite these obstacles, the potential of electron microscopy to resolve atomic distances has driven biological scientists to devise methods to overcome them and therefore image their samples at the highest resolution. The following sections will describe these methods in detail.

2.2.1 Negative Staining

This technique is a well established method of increasing the amount of electron scatter from a biological sample [15]. In short, a metallic salt such as uranyl acetate is used to coat the sample on an EM grid. The stain surrounds the sample and a 'negative' image is produced. Since there is less stain where the sample resides than on a blank area of grid surrounding it, the detected electron energy is higher from the areas surrounding the sample, and so a negative image of the sample is formed. Negative staining is the default biological electron microscopy technique, and many different stains and protocols have been developed to suit varying samples or imaging conditions [16].

There are several drawbacks with using negative stain to increase the contrast of a sample. One is that it tends to inflate the size of the sample by around 20Å(the size of uranyl acetate crys-

tals), as the stain surrounds the edge. This means that although it is easier to visualise structure it is important to take the effect of the stain into account when performing size quantification. Different stains also react differently depending on the type of sample, for example some do not work with lipids. This means features can be missed if the correct stain is not chosen. As a result of these limitations, although negative staining is a very popular technique in biosciences, it is mainly used in conjunction with complementary structural techniques which can often be performed in the hydrated state (light microscopy, dynamic light scattering), some of which are discussed in the biological introductions to Chapters 4,5 and 6.

2.2.2 Gold Labelling

A more specific contrast enhancing technique is gold labelling, where gold nano-particles are coated with protein, antibodies or other ligands which specifically attach to biological targets [17, 18]. When introduced to a sample they attach onto the target, allowing the low atomic number biological molecule to be easily located in the TEM by the contrast generated by the attached gold nanocluster [19]. Sousa *et. al.* [20] have investigated the use of ultra-small (11 atoms and 1.4nm diameter) gold clusters as localisation aids. It was found that the smaller gold particles were ideal in that their size meant they interacted less with the surrounding environment and smaller targets could be found within a larger structure, however their size meant they were difficult to localise using TEM and so bright field STEM (discussed in detail below) was suggested instead due to its higher resolution capabilities. Dynamic studies of gold labelled molecules can also be performed using light microscopy prior to TEM imaging (correlative microscopy) [21]. This combines the advantages of dynamic imaging in physiological conditions from fluorescent microscopy with the detailed structural insight provided by TEM.

2.2.3 Sample Fixing

In order to stabilise samples under electron radiation and within the vacuum, a number of techniques have been developed. These include embedding a sample in resin, freeze fracture and etching [15]. Traditionally, these are used to visualise macrostructures such as cell architecture as large sections can be prepared and analysed. The samples are made by sectioning with a ultra microtome to a thickness of between 70 and 100nm. Staining can also be introduced into the embedding media to increase the contrast from features within the sample.

For liquid samples, such as proteins in a buffer solution, it is straight forward to prepare the grid via a method known as 'drop casting' [11]. A small amount of sample (normally around 5 μl) is dropped onto a carbon coated electron microscopy grid and left to dry in air. This is the method used in this research, as all samples are either proteins or small molecules in a buffer solution. There are some drawbacks of this technique, mainly crystallisation of the buffer solution during the drying process. This was encountered during the work presented in this thesis and the protocols developed to avoid it are discussed in chapter 5.

2.2.4 Chemical Characterisation

Elemental characterisation is useful for samples where more than one element is used in the preparation, and particularly for organically produced particles that may have interaction with many different processes and be contaminated with unwanted elements. Electron diffraction is a useful tool in the materials sciences as crystals with long range order diffract electrons and thus can be characterised by the resulting electron diffraction pattern [22]. This technique is not so reliable for short-range structures or biological samples which do not exhibit such crystal structure.

In figure 2.3 it can be seen that one of the signals reflected from the surface of the sample

is characteristic x-rays. When a beam electron interacts with an atom in the sample, enough energy can be transferred to release electrons from the inner shell, causing an electron from a higher shell to drop in energy into the hole created and release an x-ray which is characteristic of the sample. The x-ray signal can be analysed and provide elemental composition information using a technique called energy dispersive x-ray (EDX) analysis. EDX detectors can be found in both SEMs and TEMs and in both cases the detector is placed above the sample [11].

2.2.5 TEM Basics

TEM and STEM can usually be performed using the same microscope, since they both analyse the signal from electrons transmitted through a sample. This means that the basic instrument components are the same, and these are discussed below. For a more detailed description of the instruments used for the research presented in this thesis please see the Experimental Methods (Chapter 3).

An Electron Microscope

A basic schematic of a transmission electron microscope set up in both TEM and STEM mode can be seen in figure 2.4. The shared components are pre-specimen lenses, electron source and sample stage. The main difference is in the post-specimen set up, with TEM requiring post-specimen lenses and a CCD camera to acquire an image and STEM needing electron detectors to collect the scattered electrons and form an image sequentially.

All the components of the microscope need to be contained within a vacuum and the whole system is often known as the 'column'. In order to maintain a suitable vacuum within the microscope column, a pressure of around 10^{-6}mbar needs to be sustained [11]. This is achieved by using several different vaccuum pumps at different stages in the system, mainly ion and diffusion [23]. A sample holder is used to secure the grid within the microscope column through

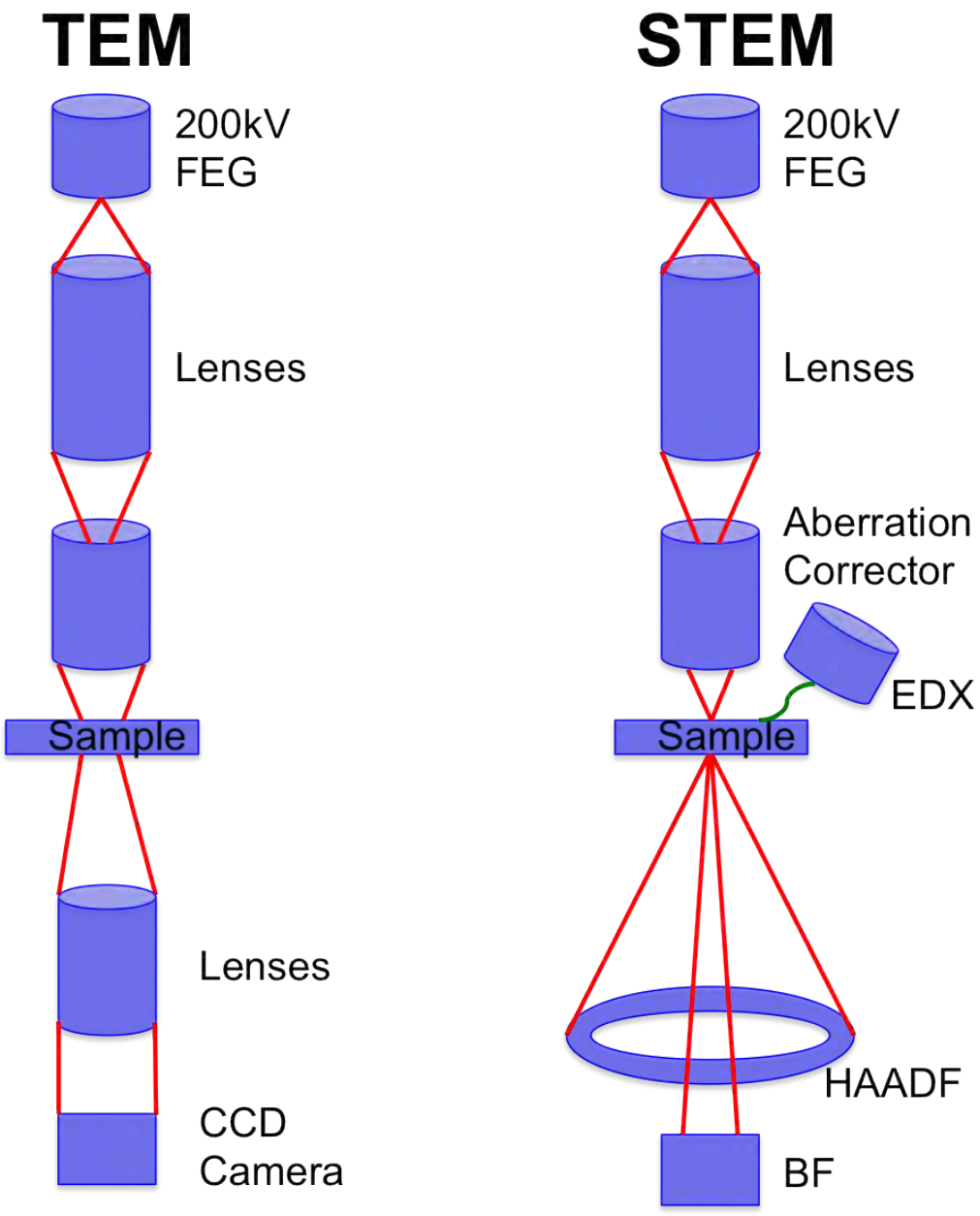

Figure 2.4: Basic schematic of an electron microscope operating in TEM and STEM mode. In TEM, a broad beam is used to illuminate the sample and post-specimen lenses form the image. In STEM, a narrow beam is scanned over the sample and the transmitted, scattered electrons are detected sequentially to build an image.

a load lock mechanism. It is the only part of the microscope that is handled by the user, and varies slightly between manufacturers. The grid is secured within a metal holder which is able to tilt to a certain angle within the confines of the column.

Optical analogies are often used to describe the principles underpinning electron microscopy. In electron microscopes, magnetic lenses are used to focus and direct the electron beam towards the sample, where in optical systems glass lenses focus the light rays. Magnetic lenses are comprised of two components: a polepiece and a coil [11]. The polepiece is a piece of magnetic material, normally iron with a hole drilled through the centre and the coil of copper wire surrounds the polepiece. When a current is passed through the coil, a magnetic field is generated in the central hole in the polepiece. This field can be used to control the electron path within the lens, by varying the current. When focusing an electron microscope, one is actually adjusting the current through the electron lenses.

The image capture device used depends on the type of electron microscopy being performed. For TEM a CCD (charge-coupled device) camera is used to collect the image forming electrons at the image plane of the electron beam [11]. STEM image collection is performed using a scintillator and is discussed in further detail below.

Sample Preparation

To prepare a sample for TEM (or STEM) it must be suitably thin ($<$500nm) to allow enough electrons to pass through the sample [15]; this often involves milling of bulk samples in embedded media. Samples are almost always mounted onto a copper grid, 3mm in diameter that can be inserted into the sample holder of the microscope. These grids can be bare or covered in a sample support material. This support material is usually made of a light atomic number to minimise signal from it. Amorphous carbon is the most common support material used, due to the ease of production and low atomic number, and is used throughout the work presented in

this thesis.

2.3 Advanced TEM Techniques for Biology

Most advanced techniques working at the resolution limit avoid the use of negative staining because this can conceal substructure. Henderson presents a comprehensive review [24] in which he concludes that electrons have the biggest potential for this type of imaging in comparison to neutrons or X-rays. In the work presented in this thesis, advanced and developing techniques are used to image biological molecules at the highest resolution. Two techniques are focused on in this section: aberration corrected STEM and cryo-TEM. These are contrasting techniques, with one more commonly applied to materials science or chemically produced samples and the other originating from the biological sciences and its need for imaging specimens in solution.

2.3.1 HAADF and BF STEM

Scanning transmission electron microscopy (STEM) was developed several decades ago [13], although only recently, with the advent of aberration correction, has the technique has come into its own [25]. The application of aberration correction in the biological sciences is rare. The main reason for this is the use of TEM in bioscience is relatively low resolution imaging to determine location of targets within wider cell architecture, which aberration correction would not be needed for and in fact would be a hinderence as the field of view is not wide enough. As opposed to standard bright field TEM, the electron beam is reduced to a small probe (around an angstrom in diameter) which is then rastered across a selected area of the sample and the image is built up on a sequential, pixel-by-pixel basis. When the beam electrons interact with the sample, they are scattered. These different signals are collected by two detectors, an annular scintillator that collects those electrons scattered with high angles (HAADF) and a standard scintillator that collects the scattered electrons by low angles (BF). When electrons interact with

matter, there are two types of scattering, incoherent or coherent.

The BF signal is a coherent signal that relies on phase contrast, it is therefore more sensitive to samples with lower atomic numbers, such as the carbon substrate of TEM grids or biological samples. The BF-STEM signal gained is similar to a conventional TEM image and is harder to interpret as the phase contrast means the signal is not directly proportional to atomic number or thickness.

The HAADF signal and can be described as being incoherent. This means that HAADF-STEM images are more straightforward to interpret and the signal is not affected by phase changes. This means the signal is directly proportional to atomic number (Z) as in equation 2.4 and can be used for quantitative study as discussed in detail below.

$$I \sim z^{\alpha} \tag{2.4}$$

The scattering coefficient n in equation 2.4 varies depending on the microscope and imaging conditions set up, in particular the inner collection angle of the HAADF detector. For example, for the conditions used in the work presented in this thesis, i.e. an inner collection angle of 62mrad and an outer collection angle of 164 mrad, the coefficient has been measured to be 1.46 $\pm$ 0.18 [26].

In STEM the post-specimen lenses are only used to direct the beam to be collected, pixel-by-pixel by the scintillator counts of either the HAADF or BF detector. The annular, HAADF, detector can be adjusted in order to collect different angles of scattered electrons. This is performed by changing the 'camera length' of the detector by adjusting the configuration of the lenses, effectively changing the theoretical height of the detector. The bright field detector is fixed and collects those electrons that are scattered through low angles.

The most common application was originally using the STEM for 'mass mapping' of individual

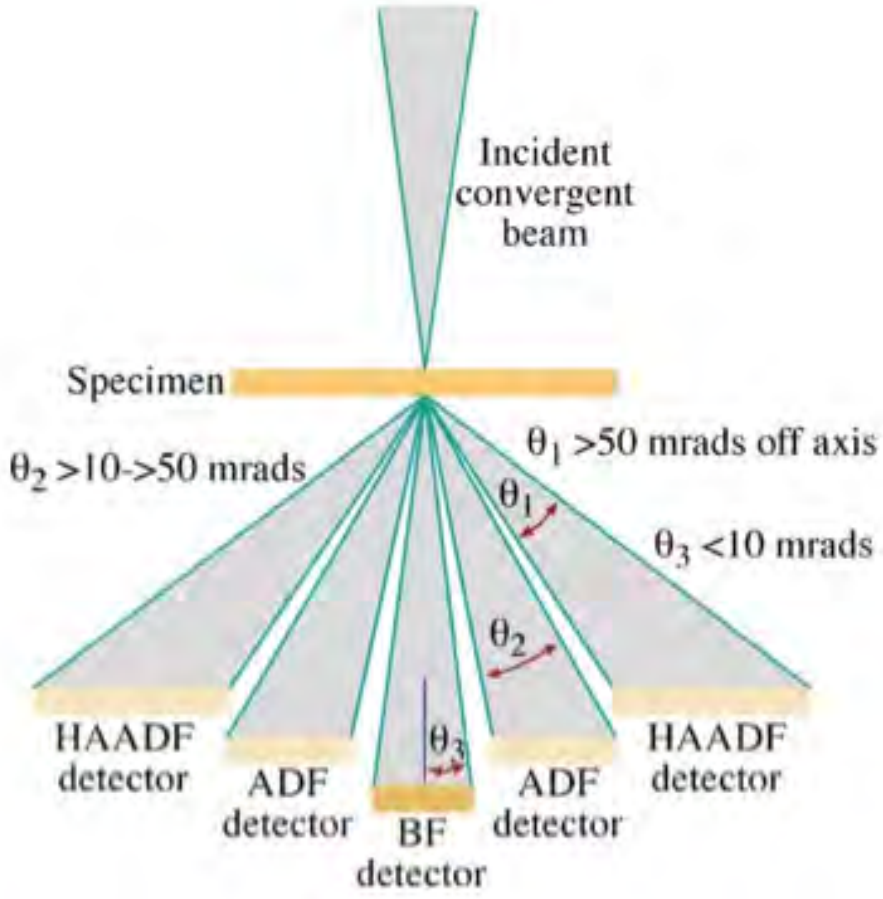

Figure 2.5: The scattering of transmitted electrons and their detectors in STEM mode. Highly scattered electrons are proportional to the atomic number of the sample and are detected by annular detectors, depending on the angle either the ADF or HAADF detector. Lower angled scattered electrons provide phase contrast and are detected by the bright field detector. (Figure reproduced from [11])

proteins, as discussed below. Recent reviews [27, 28] have identified areas where the technique could thrive. Namely tomography of thick sections and low dose studies, discussed below.

One of the disadvantages of electron microscopy in general is the energy dose transferred to the sample from the electron beam. This can be damaging to sensitive materials such as biological samples and in some cases can completely destroy them. So called 'low-dose' [29] or 'gentle STEM' [30] has therefore been investigated as a method to image sensitive samples. This can be achieved via a number of methods: lowering the gun current, accelerating voltage or pixel dwell time. If successful, this could allow routine structural study of biological samples in the STEM, especially if combined with new supports such as graphene oxide [31] which improve contrast of unstained specimens.

One of the advantages of STEM is that there is no need for strong post-specimen lenses which can introduce the further chromatic aberrations that arise in conventional TEM. This means that it is possible to image thicker (in the micrometre range) sections and so to study biological specimens in a wider cellular context, as demonstrated by Leapman *et. al.* [32] using bright field tomography. The quality of the images obtained is comparable with that of conventional TEM tomography.

Liquid STEM is an emerging technique and ferritin has been used as a protein standard to assess the validity of the technique [33]. Ferritin was introduced into a liquid cell engineered from silicon nitride windows that can hold several microlitres of protein in solution. It was found that ferritin cores could be localised and imaged, especially when locally bound to one side of the silicon window. Whole cells can also be imaged [34], whereas in conventional S/TEM they must be sectioned in order to be thin enough for the electrons to pass through. This technology has huge potential for biological imaging if the protocols can be refined, particularly to reduce sample drift and radiation damage [35].

It has also been suggested that HAADF-STEM has potential for imaging polymer systems [36, 37] which share similarities with biological systems in that they are both organic, i.e. carbon based and beam sensitive. This is discussed in more detail in Chapter 5.

$Pb_{12}Sr0_8Fe_2O_5$ has been used as a test sample to demonstrate the use of quantitative STEM for structure and composition determination [38]. This is done at an atomic scale, where the difference between different atomic columns in the material can be seen as a difference in the z-contrast HAADF-STEM image. For a truly quantitative determination of the composition of each column, a model and image simulation must be used in order to gain an absolute value. This is only realistic for well known samples with little contamination and resistance to high electron doses.

2.3.2 Mass Measurement with HAADF-STEM

Due to the relatively straightforward imaging mechanism and interpretation, many quantitative studies of both chemical and biological samples have been achieved using HAADF-STEM techniques. Protein mass measurement with STEM is a long-standing technique, usually utilising tobacco mosaic virus as a mass standard [39, 40] and most often used to calculate the 'mass-per-length' of fibrous proteins [41]. The sample is normally unstained, freeze dried and repeatedly water washed. The error in the technique ranges from 3 - 10 % [42]. Quantitative mass measurement has also been performed without a mass standard [43] at a 300kV accelerating voltage using cross section calibrations. One example is that of GroEL, where STEM was used to determine the ratios of different stoichiometries of the molecules present [44].

A novel mass measurement technique has been developed in the NPRL using size-selected gold nano-clusters as a mass standard. Size-selected clusters (discussed in chapter 3) are ideal for use as mass balances in STEM, as the high angle annular dark field (HAADF) intensity is size-dependent and a monotonic mass-intensity relationship (equation 2.4) has been found for gold

clusters up to 6,500 atoms per cluster [45, 46]. Size-selected clusters can be manufactured with high mass resolution, imaged alongside the sample and the integrated intensities can be compared whilst taking into account the calibrated α value in the Z^{α} dependence, recently calibrated for the microscope in the NPRL [26]. It has been demonstrated that this technique is effective for chemically prepared nanoparticles [47], but until now, has not been applied to biological molecules. Most recently this has been applied to catalyst particles [48] to ascertain the number of palladium atoms in each particle and the morphology changes induced by different preparation procedures. To the authors knowledge, this variation of mass mapping in the STEM has never been used to calculate the metal content of a protein and this is the subject of the study presented in chapter 4.

2.3.3 Aberration Correction

Just as in optical microscopy, lens aberrations are the major obstacle to achieving the highest resolutions. It is for this reason that aberration correctors have been developed for electron microscopes. There are two principle aberrations present in a lens - chromatic and spherical. Chromatic aberrations occur when the response of the lens is dependent on electron wavelength. Spherical aberrations are where the response of the lens varies across it, meaning electrons which hit it in different places are focused to a different point (see figure 2.6) [49]. At present, spherical aberration correctors are the most common in use and although chromatic aberration correctors do exist, they are still in a developmental phase.

Aberration correctors [50] are basically additional hexapole lenses which introduce non-rotational symmetry to the path of the electrons. Their proper alignment and stability is essential to achieve the highest resolutions. This involves an iterative correction procedure, more details of which can be found in Chapter 3. Microscopes can be either double or probe corrected. This depends on whether their principal operating mode is TEM or STEM. In TEM, as there are pre and post specimen lenses, double correction is needed. Whereas in STEM, only pre-specimen lenses are

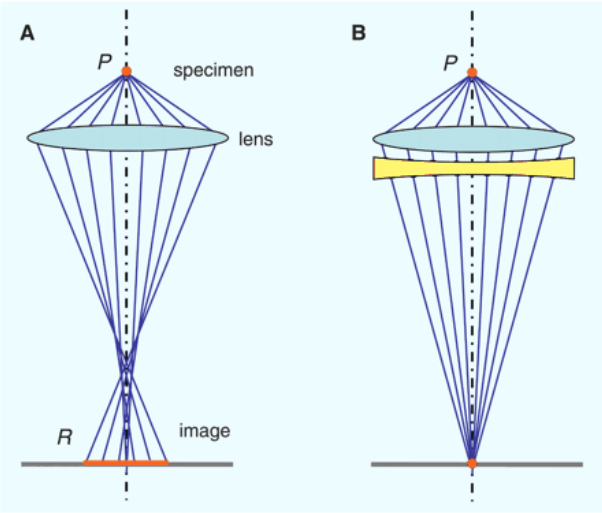

Figure 2.6: A spherical aberration corrector improves the resolution of a microscope by applying an electromagnetic field in order to focus all the electrons into the same place (B), instead of those that have passed through the edge of the lens being focused in a different place to the central ones (A). Figure reproduced from [49]

used and so a single, probe corrector is installed.

Chromatic aberration is an issue with TEM, since the electrons leaving the sample all have different energy and so if the post specimen lenses behave differently with different energy/wavelength, the signal will be affected. This means that uncorrected TEM images cannot be quantified in the same way as HAADF-STEM images.

Atomic resolution is now routine in the materials sciences, where target samples are often a high atomic number and resistant to sustained electron dose. For example Krivanek *et al.* [51] demonstrated atomic level imaging and chemical characterisation as illustrated in figure 2.7. This shows a HAADF-STEM image of a boron nitride monolayer with corresponding intensity profiles demonstrating the ability to distinguish different elements from the HAADF intensity.

In terms of biological samples, there have been studies showing that aberration correction does not improve image quality significantly for biological systems because of the other limiting fac-

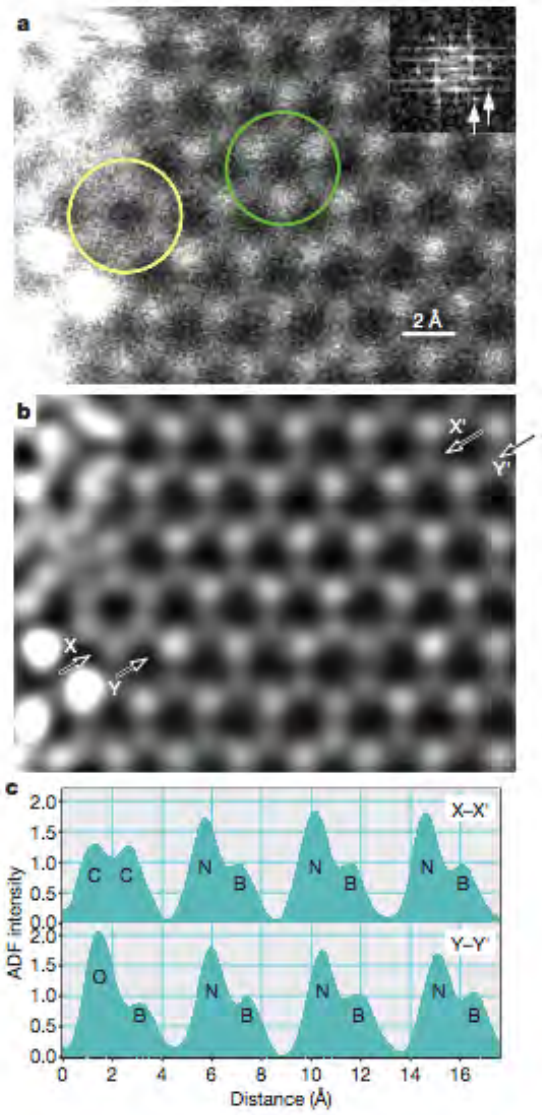

Figure 2.7: This figure reproduced from [51] shows atomic level imaging and chemical characterisation of a boron nitride monolayer using HAADF-STEM. The boron and nitrogen atoms can be distinguished (a) based on their filtered (b) HAADF-STEM intensity profile (c).

tors such as sample stability [52]. However, more recently aberration correction has been used for some samples and it seems it could be relevant for certain cases. Quantitative analysis has also revealed advantages in using aberration corrected STEM in the bright field mode [53].

Evans *et al.* [54] present a study of organic specimens, as an analogy to biological samples, using aberration corrected TEM. As this was a proof-of-concept study, silicon and paraffin were used as examples of organic, dose sensitive materials. Working at cryo temperatures allowed a resolution of 0.16nm to be achieved with direct imaging at low doses, which is a significant improvement on standard TEM resolutions.

Single walled carbon nanotubes, which are beam sensitive and low in atomic number and so analogous to biological samples, have been localised within cell sections with HAADF-STEM imaging and HAADF-STEM 3D tomography [55] using an aberration corrected instrument. The dose implications for these sensitive materials have also been discussed [56].

2.3.4 Cryo TEM

As discussed, biological samples must be fixed in some way in order to enter the vacuum. For small molecules such as proteins, conformation usually changes during procedures such as negative stain. Cryogenic TEM has been developed as a method to immobilise biological molecules in a hydrated state which can be maintained within the vacuum of an electron microscope [57]. The challenge of freezing biological material with a standard protocol is that the formation of ice crystals at best deforms and at worst destroys the sample. This will be even more noticeable at the small scale examined in TEM imaging, and so non-crystalline, vitreous ice is formed through rapid plunge freezing.

Samples are vitrified by plunge freezing into liquid ethane cooled down to liquid nitrogen temperatures (77k), forming non-crystalline ice. The faster cooling rate of ethane is more appropriate than liquid nitrogen. This is then transferred into the microscope with a specially engineered holder (more details in Chapter 3) and the temperature maintained with a liquid nitrogen cooled dewar.

This technique was pioneered by Jacques Dubochet in the late 1980's [58]. This was the first time anyone had viewed a vitrified biological specimen within the electron microscope, with the main breakthrough being the realisation that a high defocus value was needed to visualise low electron contrast material [59]. This was the start of a new era in biological electron microscopy where high resolution close to that achieved by materials scientists was possible for sensitive biological molecules.

Due to the highly damaging nature of the electron beam, a low electron dose imaging protocol must be used in order to gain viable images. This technique has been used for high resolution structural biology to resolve the three dimensional atomic structure of various proteins. In order to do this a technique called single particle cryo EM must be carried out. A large number of proteins are imaged ($>$5000), and because they can be assumed to be randomly orientated in the

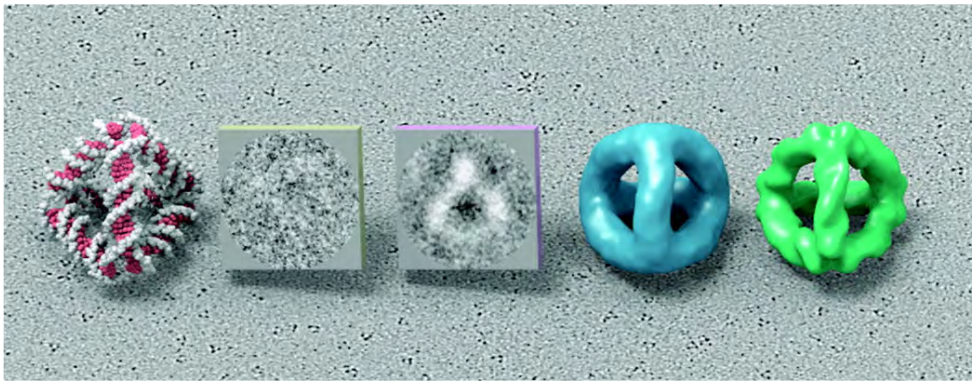

Figure 2.8: This figure from [61] shows atomic level imaging of the DNA helix using cryo-EM. The atomic models shown in the foreground are achieved by averaging the thousands of cryo-EM images shown in the background.

ice, the images can be classed into different orientations and treated like a tomographic tilt series. Although an image of a single protein seems inconclusive, when combined with thousands and analysed this way the results can be extremely informative. A comprehensive review of the imaging protocol and image reconstruction techniques has been presented by Orlova *et. al.* [60].

Near-atomic resolution has been reached by exploiting the icosahedral symmetry of viral proteins [62]. The DNA nanostructure has been studied at high resolution using cryo-TEM [61]. The DNA helix is visible with cryo-EM reconstruction and focal series, as illustrated in figure 2.8. This background of the figure shows some of the thousands of molecules needed for averaging to reconstruct and refine a model for the DNA. The fore-figure furthest to the right shows the refined helix structure.

2.3.5 Cryo-TEM Tomography

An alternative method to obtain a three dimensional image of biological molecules in the electron microscope is tomography. Electron tomography follows the same principles as that used in other imaging modalities (such as X-ray computed tomography). Projections of the same object are taken at a range of angles surrounding the object [63]. This is done in the electron

microscope by tilting the specimen as the beam is fixed. The three-dimensional reconstruction is then based on the central slice theorem which states that 'a projection at a given angle is a central section through the Fourier transform of that object' [64], hence, performing an inverse Fourier transform on the collated Fourier transformed projections results in the reconstruction of the object in three dimensions. This has been done on cell sections as room temperature for the desmosome [65], resulting in a revelation in the understanding of the interaction of intermediate filaments and the rest of the cell. Cryo-STEM tomography of whole, unstained vitrified cells has also recently been demonstrated [66].

Tomography of single molecules is possible through cryo-TEM but is more challenging as the sample is more delicate and the dose is higher per unit area of the sample, however, this has been performed on large molecules such as the herpes simplex virus [67] and immunoglobulins [68].

The reconstruction of the slices can be a computationally demanding process. It is helpful if there are reference points in the images which can be used to aid in registration between slices, these are known as fiducial markers. In electron microscopy, a highly electron scattering object is most useful as a fiducial marker, as it can easily be detected in an image; gold nanoparticles are ideal for this purpose [20].

2.4 Summary

The principals behind electron microscopy have been explained, along with the specific challenges relating to biological samples. Advanced techniques have also been described, focusing on those used in the research contributing to this thesis and examples have been given of the current work in the field. Aberration corrected STEM is not widely used in the biological sciences despite its high resolution capabilities. In the subsequent chapters of this thesis, bio-

logical research is presented that has been furthered by the use of aberration corrected STEM which could not have been achieved with conventional TEM. In the final results chapter, work is presented towards imaging single proteins encapsualted by nano-discs using a combination of cryo-TEM, negative stain and nano-gold labelling.

References

[1] G. B. Frisoni, N. C. Fox, C. R. Jack, P. Scheltens, and P. M. Thompson. The clinical use of structural MRI in alzheimer disease. *Nature Reviews Neurology*, 6(2):67–77, 2010.

[2] H. Quigley, S. J. Colloby, and J. T. O'Brien. PET imaging of brain amyloid in dementia: a review. *International journal of geriatric psychiatry*, 26(10):991–999, 2011.

[3] D. Toomre and J. Bewersdorf. A new wave of cellular imaging. *Annual review of cell and developmental biology*, 26:285–314, 2010.

[4] O. F. Lange, P. Rossi, N. G. Sgourakis, Y. Song, H W Lee, J. M. Aramini, A. Ertekin, R. Xiao, T. B. Acton, G. T. Montelione, et al. Determination of solution structures of proteins up to 40 kda using CS-Rosetta with sparse nmr data from deuterated samples. *Proceedings of the National Academy of Sciences*, 109(27):10873–10878, 2012.

[5] A. J. Katan and C. Dekker. High-speed AFM reveals the dynamics of single biomolecules at the nanometer scale. *Cell*, 147(5):979–982, 2011.

[6] H. D. T. Mertens and D. I. Svergun. Structural characterization of proteins and complexes using small-angle X-ray solution scattering. *Journal of structural biology*, 172(1):128–141, 2010.

[7] K. R. Porter, A. Claude, and E. F. Fullam. A study of tissue culture cells by electron microscopy methods and preliminary observations. *The Journal of experimental medicine*, 81(3):233–246, 1945.

[8] G. E. Palade. A study of fixation for electron microscopy. *The Journal of Experimental Medicine*, 95(3):285–298, 1952.

[9] A. J. Koster, J. Klumperman, et al. Electron microscopy in cell biology: integrating structure and function. *Nature Reviews Molecular Cell Biology*, 4(9; SUPP):SS6–SS9, 2003.

[10] D. A. Muller. Structure and bonding at the atomic scale by scanning transmission electron microscopy. *Nature materials*, 8(4):263–270, 2009.

[11] D.B. Williams and C.B. Carter. *Transmission electron microscopy: a textbook for materials science*. Springer, 2009.

[12] M. Knoll and E. Ruska. Das elektronenmikroskop. *Zeitschrift für Physik A Hadrons and Nuclei*, 78(5):318–339, 1932.

[13] A. V. Crewe, J. Wall, and J. Langmore. Visibility of single atoms. *Science*, 168(3937):1338–1340, 1970.

[14] P. E. Batson, N. Dellby, and O. L. Krivanek. Sub-ångstrom resolution using aberration corrected electron optics. *Nature*, 418(6898):617–620, 2002.

[15] D. E. Chandler and R. W. Roberson. *Bioimaging: current concepts in light and electron microscopy*. Jones & Bartlett Publishers, 2009.

[16] B. S. Weakly. *Electron Diffraction: An Introduction for Biologists*. Churchill Livingstone, 2 edition, 1981.

[17] M. Horisberger and J. Rosset. Colloidal gold, a useful marker for transmission and scanning electron microscopy. *Journal of Histochemistry & Cytochemistry*, 25(4):295–305, 1977.

[18] S. Thobhani, S. Attree, R. Boyd, N. Kumarswami, J. Noble, M. Szymanski, and R. A. Porter. Bioconjugation and characterisation of gold colloid-labelled proteins. *Journal of immunological methods*, 356(1):60–69, 2010.

[19] Y. He, G. J. Jensen, and P. J. Bjorkman. Nanogold as a specific marker for electron cryotomography. *Microscopy and Microanalysis*, 15(03):183–188, 2009.

[20] A. A. Sousa, M. A. Aronova, Y. C. Kim, L. M. Dorward, G. Zhang, and R. D. Leapman. On the feasibility of visualizing ultrasmall gold labels in biological specimens by STEM tomography. *Journal of structural biology*, 159(3):507–522, 2007.

[21] R. S. Polishchuk, E. V. Polishchuk, P. Marra, S. Alberti, R. Buccione, A. Luini, and A. A. Mironov. Correlative light-electron microscopy reveals the tubular-saccular ultrastructure of carriers operating between golgi apparatus and plasma membrane. *The Journal of cell biology*, 148(1):45–58, 2000.

[22] D. L. Misell and E. B. Brown. *Electron Diffraction: An Introduction for Biologists*, volume 12 of *Practical Methods in Electron Microscopy*. Elsevier, 1987.

[23] Jeol. *JEM-2100F Manual*. Jeol, 1 edition, 2009.

[24] R. Henderson. The potential and limitations of neutrons, electrons and X-rays for atomic resolution microscopy of unstained biological molecules. *Quarterly reviews of biophysics*, 28:171–171, 1995.

[25] S. J. Pennycook. Seeing the atoms more clearly: STEM imaging from the crewe era to today. *Ultramicroscopy*, 123:28–37, 2012.

[26] Z. W. Wang and R. E. Palmer. Intensity calibration and atomic imaging of size-selected Au and Pd clusters in aberration-corrected HAADF-STEM. In *Journal of Physics: Conference Series*, volume 371, page 012010. IOP Publishing, 2012.

[27] A. A. Sousa and R. D. Leapman. Development and application of STEM for the biological sciences. *Ultramicroscopy*, 2012.

[28] S. A. Müller, D. J. Müller, and A. Engel. Assessing the structure and function of single biomolecules with scanning transmission electron and atomic force microscopes. *Micron*, 42(2):186–195, 2011.

[29] J. P. Buban, Q. Ramasse, B. Gipson, N. D. Browning, and H. Stahlberg. High-resolution low-dose scanning transmission electron microscopy. *Journal of electron microscopy*, 59(2):103–112, 2010.

[30] O. L. Krivanek, N. Dellby, M. F. Murfitt, M. F. Chisholm, T. J. Pennycook, K. Suenaga, and V. Nicolosi. Gentle STEM: ADF imaging and EELS at low primary energies. *Ultramicroscopy*, 110(8):935–945, 2010.

[31] J. P. Patterson, A. M. Sanchez, N. Petzetakis, T. P. Smart, T. H. Epps III, I. Portman, N. R. Wilson, and R. K. O'Reilly. A simple approach to characterizing block copolymer assemblies: graphene oxide supports for high contrast multi-technique imaging. *Soft Matter*, 8(12):3322–3328, 2012.

[32] A. A. Sousa, A. A. Azari, G. Zhang, and R. D. Leapman. Dual-axis electron tomography of biological specimens: Extending the limits of specimen thickness with bright-field STEM imaging. *Journal of structural biology*, 174(1):107–114, 2011.

[33] J. E. Evans, K. L. Jungjohann, P. C. K. Wong, P-L Chiu, G. H. Dutrow, I. Arslan, and N. D. Browning. Visualizing macromolecular complexes with¡ i¿ in situ¡/i¿ liquid scanning transmission electron microscopy. *Micron*, 43(11):1085–1090, 2012.

[34] N. De Jonge, D. B. Peckys, G. J. Kremers, and D. W. Piston. Electron microscopy of whole cells in liquid with nanometer resolution. *Proceedings of the National Academy of Sciences*, 106(7):2159–2164, 2009.

[35] P Abellan, TJ Woehl, LR Parent, ND Browning, JE Evans, and I Arslan. Factors influencing quantitative liquid (scanning) transmission electron microscopy. *Chemical Communications*, 50(38):4873–4880, 2014.

[36] E. Sourty, S. van Bavel, K. Lu, R. Guerra, G. Bar, J. Loos, et al. High-angle annular dark field scanning transmission electron microscopy on carbon-based functional polymer systems. *Microscopy and Microanalysis*, 15(3):251, 2009.

[37] J. Loos, E. Sourty, K. Lu, G. de With, and S. v. Bavel. Imaging polymer systems with high-angle annular dark field scanning transmission electron microscopy (HAADF- STEM). *Macromolecules*, 42(7):2581–2586, 2009.

[38] G. T. Martinez, A. Rosenauer, A. De Backer, J. Verbeeck, and S. Van Aert. Quantitative composition determination at the atomic level using model-based high-angle annular dark field scanning transmission electron microscopy. *Ultramicroscopy*, 137:12–19, 2014.

[39] A. Engel and C. Colliex. Application of scanning transmission electron microscopy to the study of biological structure. *Current opinion in biotechnology*, 4(4):403–411, 1993.

[40] S. A. Muller and A. Engel. Biological scanning transmission electron microscopy: imaging and single molecule mass determination. *CHIMIA International Journal for Chemistry*, 60(11):749–753, 2006.

[41] C. Colliex and C. Mory. Scanning transmission electron microscopy of biological structures. *Biology of the Cell*, 80(2):175–180, 1994.

[42] S. A. Müller and A. Engel. Structure and mass analysis by scanning transmission electron microscopy. *Micron*, 32(1):21–31, 2001.

[43] A. A. Sousa and R. D. Leapman. Quantitative STEM mass measurement of biological macromolecules in a 300 kV TEM. *Journal of microscopy*, 228(1):25–33, 2007.

[44] A. Engel, M. K. Hayer-Hartl, K. N. Goldie, G. Pfeifer, R. Hegerl, S. Muller, A. C. da Silva, W. Baumeister, and F. U. Hartl. Functional significance of symmetrical versus asymmetrical GroEL-GroES chaperonin complexes. *Science*, 269(5225):832–836, 1995.

[45] Z. Y. Li, N. P. Young, M. Di Vece, S. Palomba, R. E. Palmer, A. L. Bleloch, B. C. Curley, R. L. Johnston, J. Jiang, and J. Yuan. Three-dimensional atomic-scale structure of size-selected gold nanoclusters. *Nature*, 451(7174):46–48, 2007.

[46] N. P. Young, Z. Y. Li, Y. Chen, S. Palomba, M. Di Vece, and R. E. Palmer. Weighing supported nanoparticles: Size-selected clusters as mass standards in nanometrology. *Physical review letters*, 101(24):246103, 2008.

[47] Z. W. Wang, O. Toikkanen, F. Yin, Z. Y. Li, B. M. Quinn, and R. E. Palmer. Counting the atoms in supported, monolayer-protected gold clusters. *Journal of the American Chemical Society*, 132(9):2854–2855, 2010.

[48] D. Pearmain, S. J. Park, Z. W. Wang, A. Abdela, R. E. Palmer, and Z. Y. Li. Size and shape of industrial Pd catalyst particles using size-selected clusters as mass standards. *Applied Physics Letters*, 102(16):163103–163103, 2013.

[49] K. W. Urban. Studying atomic structures by aberration-corrected transmission electron microscopy. *Science*, 321(5888):506–510, 2008.

[50] CEOS website. *http://www.ceos-gmbh.de/*. CEOS, 2014.

[51] O. L. Krivanek, M. F. Chisholm, V. Nicolosi, T. J. Pennycook, G. J. Corbin, N. Dellby, M. F. Murfitt, C. S. Own, Z. S. Szilagyi, M. P. Oxley, et al. Atom-by-atom structural and chemical analysis by annular dark-field electron microscopy. *Nature*, 464(7288):571–574, 2010.

[52] A. Ziegler, B. Rockel, R. Hegerl, B. Freitag, U. Lücken, and J. M. Plitzko. Aberration-corrected microscopy for structural biology applications. *Journal of Microscopy*, 233(1):170–177, 2009.

[53] K. Sader, A. Brown, R. Brydson, and A. Bleloch. Quantitative analysis of image contrast in phase contrast STEM for low dose imaging. *Ultramicroscopy*, 110(10):1324–1331, 2010.

[54] J. E. Evans, C. Hetherington, A. Kirkland, L-Y Chang, H. Stahlberg, and N. Browning. Low-dose aberration corrected cryo-electron microscopy of organic specimens. *Ultramicroscopy*, 108(12):1636–1644, 2008.

[55] A. E. Porter, M. Gass, K. Muller, J. N. Skepper, P. A. Midgley, and M. Welland. Direct imaging of single-walled carbon nanotubes in cells. *Nature Nanotechnology*, 2(11):713–717, 2007.

[56] M. H. Gass, A. E. Porter, J. S. Bendall, K. Muller, J. N. Skepper, P. A. Midgley, and M. Welland. Cs corrected STEM EELS: Analysing beam sensitive carbon nanomaterials in cellular structures. *Ultramicroscopy*, 110(8):946–951, 2010.

[57] J. Dubochet, M. Adrian, J-J Chang, J. Lepault, and A. W. McDowall. Cryoelectron microscopy of vitrified specimens. In *Cryotechniques in Biological Electron Microscopy*, pages 114–131. Springer, 1987.

[58] M. Adrian, J. Dubochet, J. Lepault, and A. W. McDowall. Cryo-electron microscopy of viruses. 1984.

[59] C. Mory, C. Colliex, and J. M. Cowley. Optimum defocus for STEM imaging and microanalysis. *Ultramicroscopy*, 21(2):171–177, 1987.

[60] E. V. Orlova and H. R. Saibil. Structural analysis of macromolecular assemblies by electron microscopy. *Chemical reviews*, 111(12):7710–7748, 2011.

[61] T. Kato, R. P. Goodman, C. M. Erben, A. J. Turberfield, and K. Namba. High-resolution structural analysis of a DNA nanostructure by cryoEM. *Nano letters*, 9(7):2747–2750, 2009.

[62] X. Zhang, E. Settembre, C. Xu, P. R. Dormitzer, R. Bellamy, S. C. Harrison, and N. Grigorieff. Near-atomic resolution using electron cryomicroscopy and single-particle reconstruction. *Proceedings of the National Academy of Sciences*, 105(6):1867–1872, 2008.

[63] J. Frank. *Electron tomography: methods for three-dimensional visualization of structures in the cell*. Springer Verlag, 2006.

[64] P. A. Midgley and M. Weyland. 3D electron microscopy in the physical sciences: the development of Z-contrast and eftem tomography. *Ultramicroscopy*, 96(3):413–431, 2003.

[65] W. He, P. Cowin, and D.L. Stokes. Untangling desmosomal knots with electron tomography. *Science*, 302(5642):109, 2003.

[66] S. G. Wolf, L. Houben, and M. Elbaum. Cryo-scanning transmission electron tomography of vitrified cells. *Nature methods*, 11(4):423–428, 2014.

[67] K. Grunewald, P. Desai, D.C. Winkler, J.B. Heymann, D.M. Belnap, W. Baumeister, and A.C. Steven. Three-dimensional structure of herpes simplex virus from cryo-electron tomography. *Science*, 302(5649):1396, 2003.

[68] L. Bongini, D. Fanelli, F. Piazza, P. De Los Rios, S. Sandin, and U. Skoglund. Freezing immunoglobulins to see them move. *Proceedings of the National Academy of Sciences of the United States of America*, 101(17):6466, 2004.

Chapter 3

Experimental Methods

In this chapter the imaging, spectroscopy, quantitative analysis and sample preparation techniques used in the course of the subsequent three results chapters will be described in detail. Scanning transmission electron microscopy (STEM) was used for two of the results chapters, whereas the third chapter is based on transmission electron microscopy (TEM). The sample preparation for both is similar and so is discussed first.

3.1 Electron Microscopy Sample Preparation

As discussed in Chapter 2, in order to be interrogated by TEM, samples must be thin and ideally less than 500nm. This necessitates the support for the sample to be as thin as possible in order to maximise space for the sample. The most common support is a small, 3mm diameter, disk usually made of copper, that is etched into a grid pattern and covered with carbon film. The grid bars provide a useful reference when imaging and the suspended carbon between them provides the support for the sample. This carbon film is normally between 20 - 50 nm thick. There are three types of carbon film that can be used, either full coverage over the grid, 'holey' or 'lacey'. Holey carbon has uneven coverage with holes to allow specimens to spread across the holes and be imaged without any interference from the background. Lacey carbon is similar but with larger holes and less carbon.

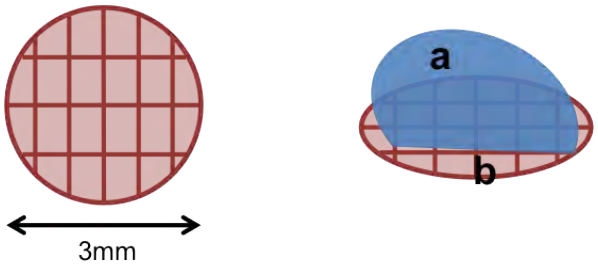

Figure 3.1: A basic schematic of a copper EM grid coated with amorphous carbon. The diagram on the right shows a representation of drop casting a liquid sample (a) onto a grid (b). The sample is then allowed to adsorb before being inserted into the electron microscope column and imaged.

EM grids can be made with a variety of materials and supports and can be customised depending on the sample. The 'mesh size' or number of grid squares per disk can also be varied, with 300 being the average. However, for the work presented in this thesis, amorphous carbon coated copper 300 mesh grids were used throughout. Both holey and full coverage carbon supports were used.

All the specimens examined in this thesis were in the liquid state prior to imaging. In order to deposit them onto the grid, a method known as 'drop-casting' was used. This is where a small amount (normally 5 μl) of sample is dropped onto the grid and left to adsorb for around 10 minutes in air before being transferred to the microscope sample holder. Figure 3.1 shows a schematic of a grid and the drop casting procedure.

3.2 Scanning Transmission Electron Microscopy

3.2.1 Jeol 2100F

A Jeol 2100F transmission electron microscope was used exclusively in scanning mode for all the STEM work presented in this thesis (chapters 4 and 5). A schematic showing the different

lenses and detectors in place in the Jeol 2100F STEM is shown in Figure 3.2.

The 'imaging' components of the microscope are a high angle annular dark field (HAADF), bright field (BF), energy dispersive x-ray (EDX) and electron energy loss (EELS) detectors. The next sections will describe these in more detail. The lenses, electron source and aberration corrector are the fundamental components that generate and focus the electron beam.

The electron source is a 200kV field emission gun, with a tungsten tip coated in zirconium oxide. The tip is a cathode with respect to two anodes. The first anode draws out the electrons from the tip, and the second accelerates them to 200kV, this is shown as a schematic in figure 3.3.

The electron beam produced from the FEG (0.9$\mathring{A}$ diameter) then passes through several different lenses in the Jeol 2100F column (see figure 3.2). As the microscope was always operated in STEM mode, all the lenses were placed before the sample chamber in the column. There are some post-specimen lenses but these are relatively weak, and are used to direct the electrons to the detector rather than imaging lenses. As discussed in chapter 2, electron lenses consist of two components, a polepiece and a coil and when a current is passed through the coil, this generates a magnetic field in the centre of the polepiece. Figure 3.4 shows a schematic of the lens. When focusing electron lenses, one is actually adjusting the current through the lenses in order to maximise image quality.

CEOS double hexapole aberration correctors are used to correct for the spherical aberrations introduced into the beam from the normal lenses. The aberration corrector is located just above the condenser mini lens coil, detailed in figure 3.2. This microscope is only corrected in STEM mode as the correctors are only installed on the pre-specimen lenses.

There are two levels of corrector alignment, the rough alignment performed several times in a

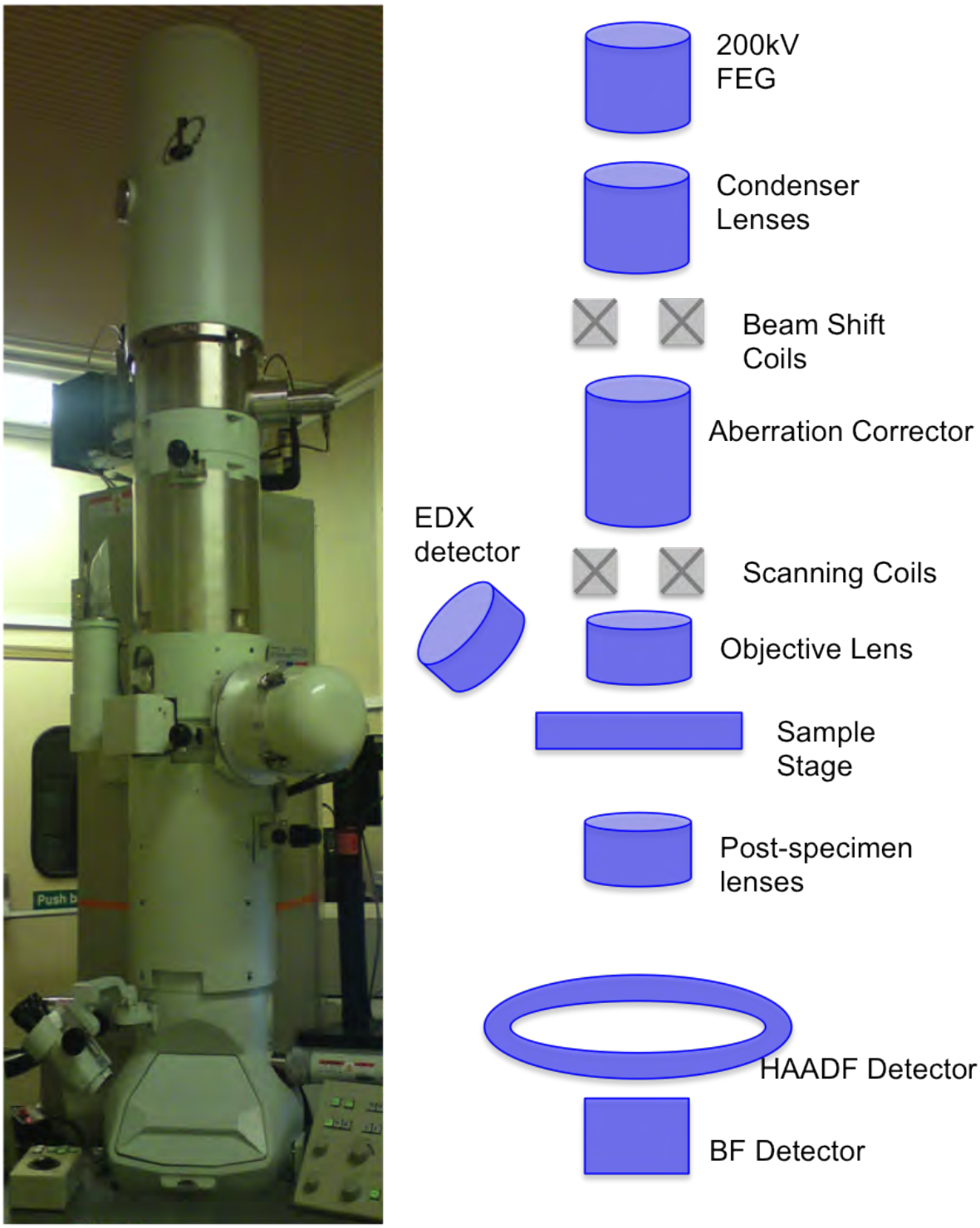

Figure 3.2: Jeol 2100F STEM and schematic of the principal components, including lenses and imaging detectors.

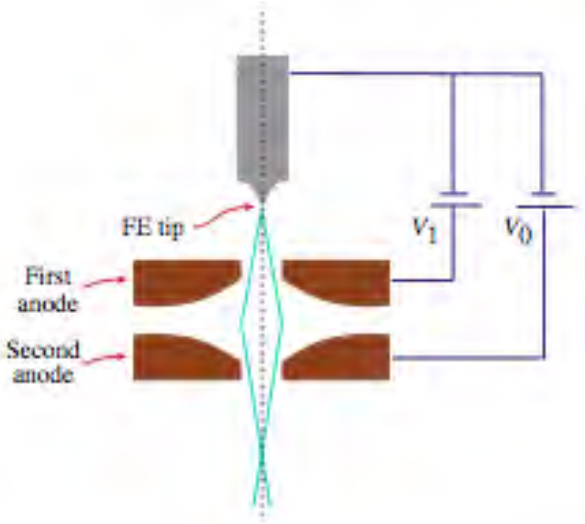

Figure 3.3: Schematic of a field emission gun (FEG) reproduced from [1]. The tungsten tip acts as a cathode in relation to two anodes. The first anode draws electrons from the tip and the second accelerates them to 200kV.

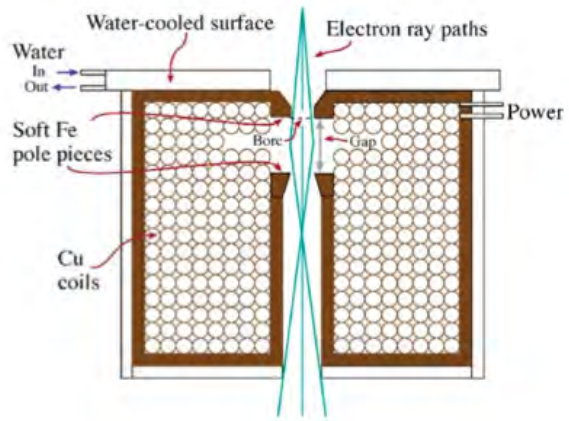

Figure 3.4: Schematic of a magnetic lens reproduced from [1]. When a current is passed through the coil, a magnetic field is generated within the bore of the polepiece meaning the electrons passing through the lens can be controlled.

session and the detailed calibration performed less often. The rough alignment is performed by analysing the 'ronchigram' [2], see figure 3.5. This is the projection of the probe formed on the diffraction plane and when in perfect alignment, it should have 12 points for each pole in the aberration corrector (i.e. 2x6 pole pieces of the two hexapole parts of the corrector) and a smooth centre. If this is not the case, the astigmatism and bright field tilt can be adjusted until the best ronchigram is obtained. If the ronchigram is poor after rough alignment, then it is necessary to perform a detailed iterative alignment up to 4 orders of symmetry. More information about ronchigram alignment can be found in articles by Browning *et. al.* [3] and Rodenburg *et. al.* [4].

A Jeol HAADF detector with inner and outer collection angles fixed at 62 and 164 mrad respectively was used to acquire all the HAADF-STEM images presented. The angles were determined by fixing the camera length at 10cm, this setting was used throughout data acquisition.

A Gatan bright field detector was used which can be inserted at the same time as the HAADF detector in order to acquire simultaneous imaging. This does not interfere with the HAADF detector and allows different contrast mechanisms to be recorded for the same sample, as described in chapter 2 above. In figure 3.6, a set of HAADF and BF images of size selected Au_{6000} clusters is presented. It can be seen that the contrast is reversed, whereby gold atoms appear bright in the HAADF image and dark in the BF signal. In figures 3.6(e) and 3.6(f) single atomic columns within the gold cluster are clear. In the HAADF image single atoms can be seen surrounding the cluster which cannot be localised in the BF image, whereas the carbon substrate is more structured in the BF image. This highlights the advantages of the different imaging modes.

A Bruker EDX detector was used, with the detector inserted above the sample in the column. In order to maximise the signal arriving at the detector the spot size of the beam was increased from standard imaging conditions to allow more electrons to interact with the sample, this was often at the expense of image quality. Point and line spectra can be taken along with maps to

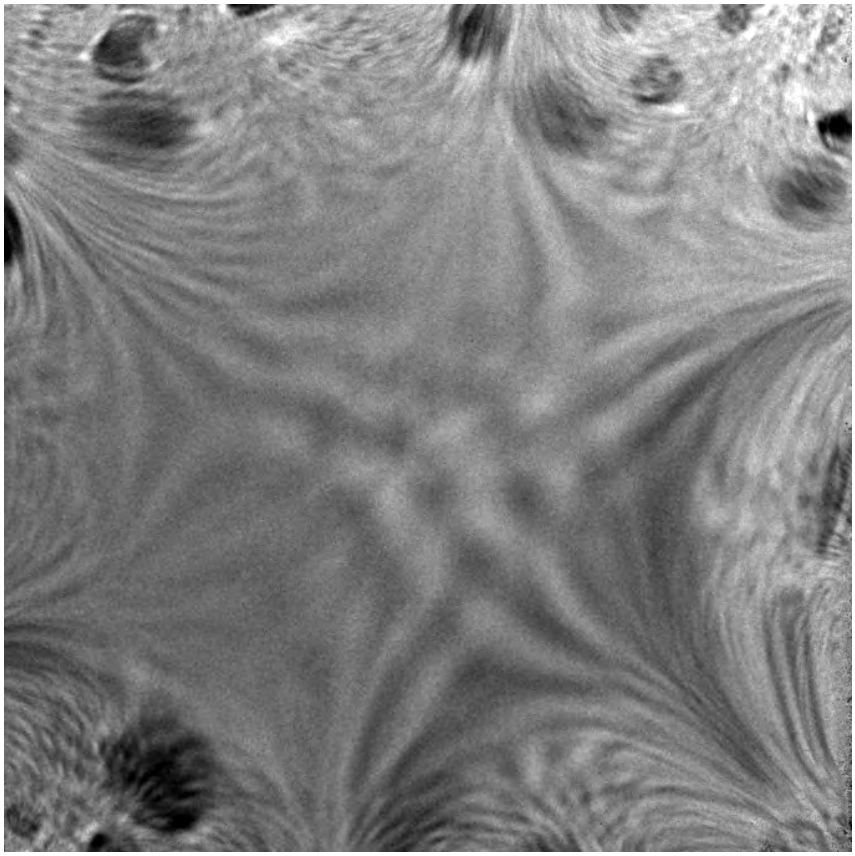

Figure 3.5: Alignment using the ronchigram. If the specimen is viewed in the diffraction plane and the corrector is well aligned, there should be 12 points (for each pole in the abberation corrector) and a smooth centre. This is used as an alignment guide, and can be modified during a microscope session to maximise image resolution. It can be seen that this only has 6 points and so would need some further alignment work to achieve the best resolution.

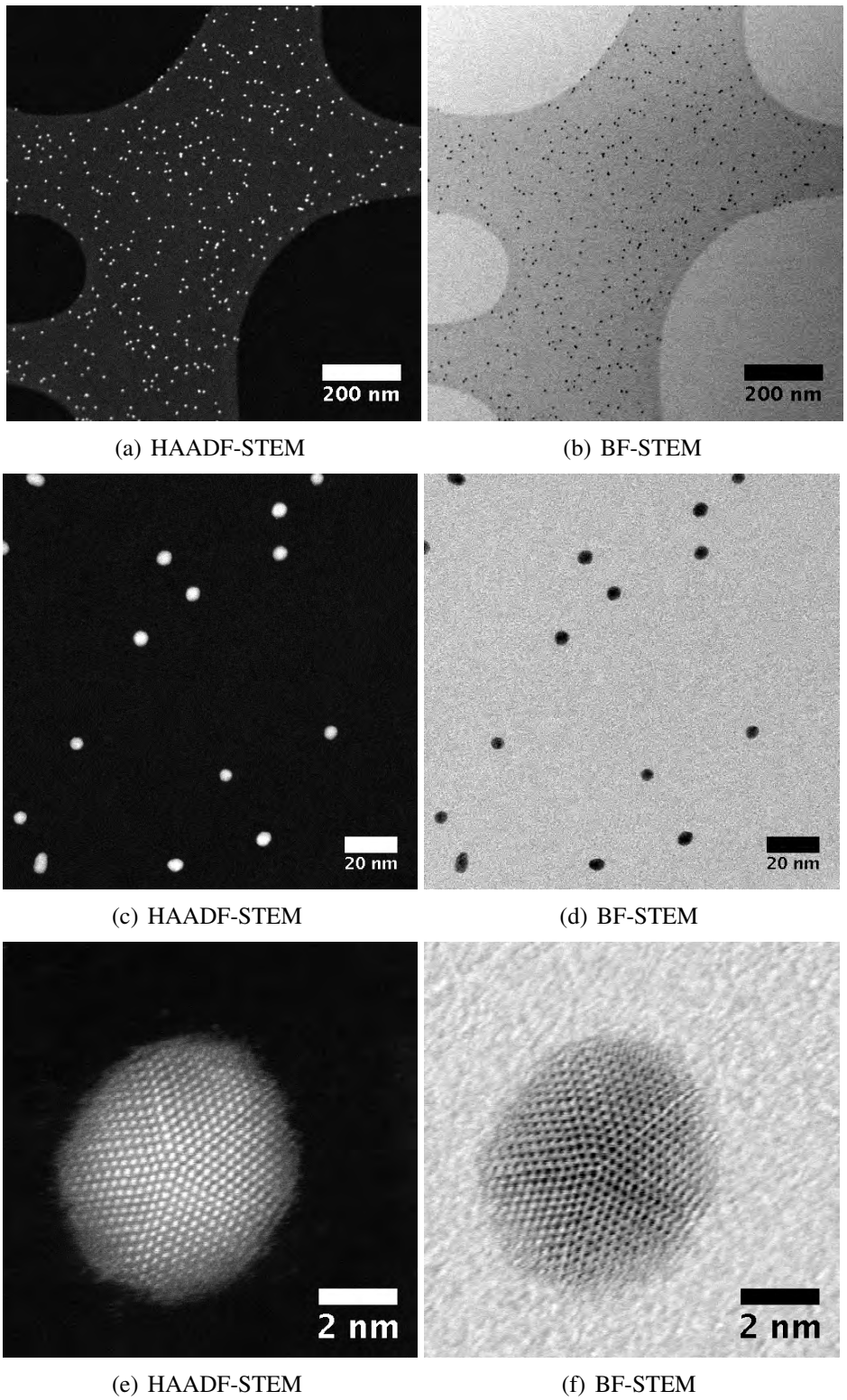

(a) HAADF-STEM (b) BF-STEM

(c) HAADF-STEM (d) BF-STEM

(e) HAADF-STEM (f) BF-STEM

Figure 3.6: HAADF and BF STEM performed simultaneously on size-selected Au_{6000} clusters deposited onto a holey carbon substrate. It can be seen that the contrast is reversed, single atoms are clearer in the HAADF images and the carbon substrate is more structured in the BF image.

show the spatial distribution of the elements of interest.

3.2.2 Imaging Protocol

A single tilt holder was used to perform all imaging. This holds a standard 3mm TEM grid in place using a screw-in lever mechanism [5]. The holder is capable of tilting up to 20 degrees on the horizontal plane.

Gatan DigitalMicrograph software was used to acquire images at usually between a range from 250k to 10M magnification with 1024x1024 pixels and a 19 ms dwell time per pixel.

Low magnification searching was performed initially, to survey the grid and locate areas where specimen had adsorbed well onto the carbon. After localizing these areas, the grid was allowed to settle within the column. This minimises both physical vibration and thermal movement and therefore allows higher resolution imaging due to reduced sample drift. At least 20 minutes of settling time was required, but for optimum results longer was needed (up to an hour).

Since the sample enters the vacuum of the column from the atmosphere, there will always be hydrocarbons present on the grid. Since these are predominantly positively charged, they are attracted to the negative electron beam and cause an overload of carbon that 'masks' the sample. To avoid this hydrocarbon contamination during imaging, the region of interest in the sample was pre-irradiated with a defocused, high intensity beam for 20 minutes. Although this will have exposed the sample to a certain dose of electrons, this will be constant over the whole sampled area. This is known as a 'beam shower' and there is more detail in [6].

Figure 3.7 demonstrates the single atom capability of the imaging system combined with the aberration corrector. A gold cluster is shown 'disintegrating' under the electron beam. Single atoms can be seen surrounding the cluster, they are spherical in shape which indicated that the

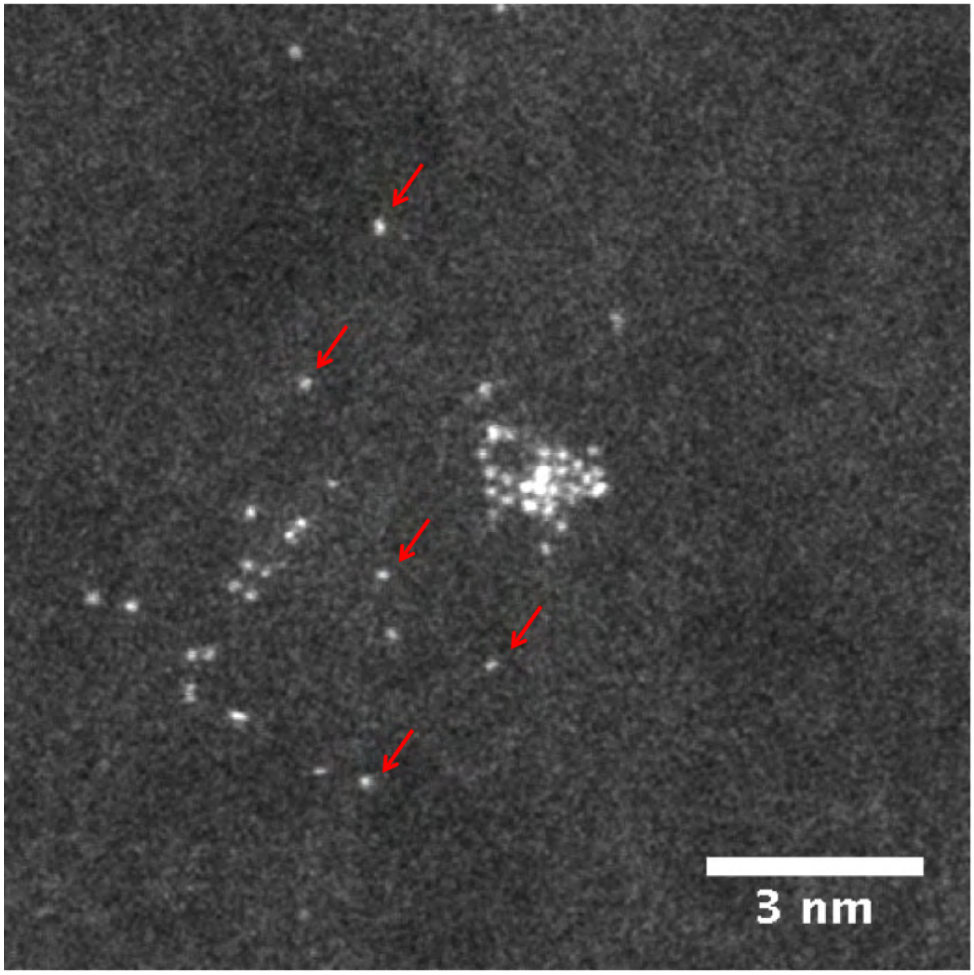

Figure 3.7: Imaging single gold atoms with HAADF-STEM. A Au_{55} cluster (centre of image) has disintegrated under the beam and this image shows single gold atoms (some examples arrowed) surrounding the clusters. The atoms are spherical in shape indicating a good corrector alignment.

aberration corrector is well aligned.

3.3 Analysis Methods

3.3.1 Size-Selected Clusters as Mass Balances

Production of Size-Selected Clusters

Size-selected clusters can be manufactured using a cluster source developed at Birmingham [7], a schematic of which is presented in figure 3.8. Briefly, in the first 'formation' stage, a metal (in this case, gold) target is plasma sputtered, producing single atoms and small clusters of the target material. These are allowed to condense and in the 'focusing' stage travel through ion optics which focus the beam down into a single cluster beam which then enters a lateral time of flight mass filter in the 'mass-selection' stage. Perpendicular voltage pulses separate the beam, and the timing of the different pulses determines which part of the beam exits the end of the filter and so allows deposition of specific sized clusters onto an electron microscopy grid, which has a voltage applied to it which determined the landing energy of the clusters. The mass filter selects on a m/z basis and so, sometimes doubly charged clusters that have twice the mass pass through the filter and are deposited onto the substrate. Since these are twice the size as the target clusters, they are obvious in analysis and relatively straight forward to exclude. An example of this can be found in chapter 4. This gas-phase technique not only results in bare clusters, but is also highly specific over a wide range of cluster sizes, from one to thousands of atoms per cluster [8]. However, there are certain sizes of cluster that are more thermodynamically stable, and so are more abundantly produced and easier to isolate. These are known as 'magic numbers' [8], two of which are 55 and 147, which is the reason these cluster sizes are used in this work.

Size-selected clusters, each consisting of 147 or 55 gold atoms were used as the mass standards for the work presented in chapter 4. They were produced in the gas-phase and selected using a lateral time-of-flight mass filter [7], with a mass accuracy of approximately 5%. In order to minimise differences in imaging conditions it is necessary to deposit both the target (ferritin) and reference (gold clusters) samples on the same carbon coated copper TEM grid. This was done by soft landing (10eV per atom) clusters onto one half of a grid, by masking the other

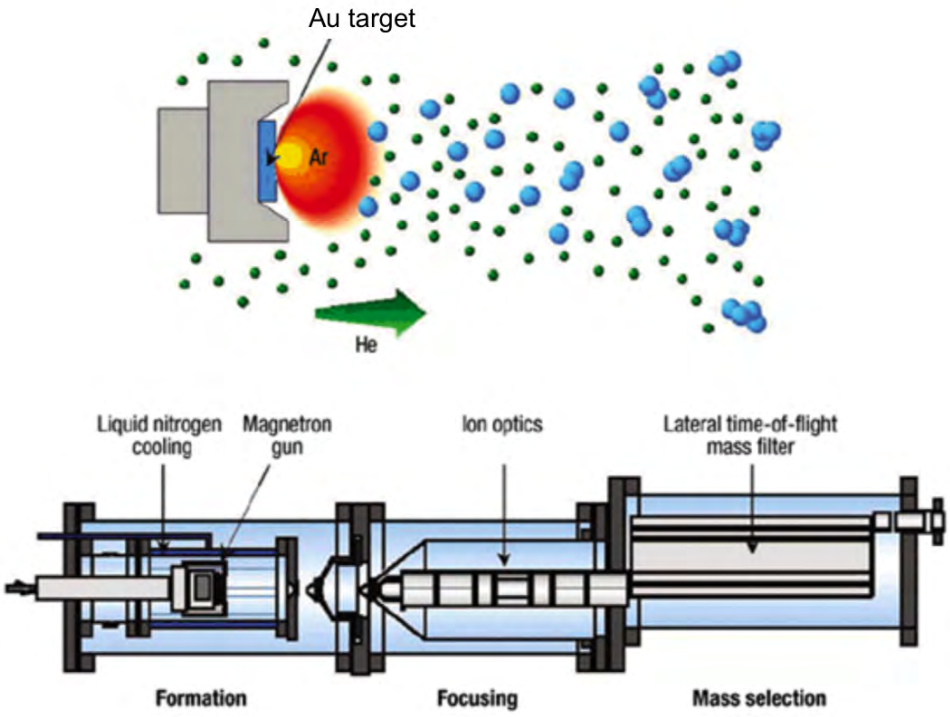

Figure 3.8: Schematic of the size-selected cluster source developed at Birmingham. There are three stages of production: formation, where gold atoms are sputtered from a target; focusing, where the atoms and allowed to condense into clusters and focused into a beam and mass selection, where the clusters are filtered by mass before being deposited onto a substrate. Figure adapted from [8]

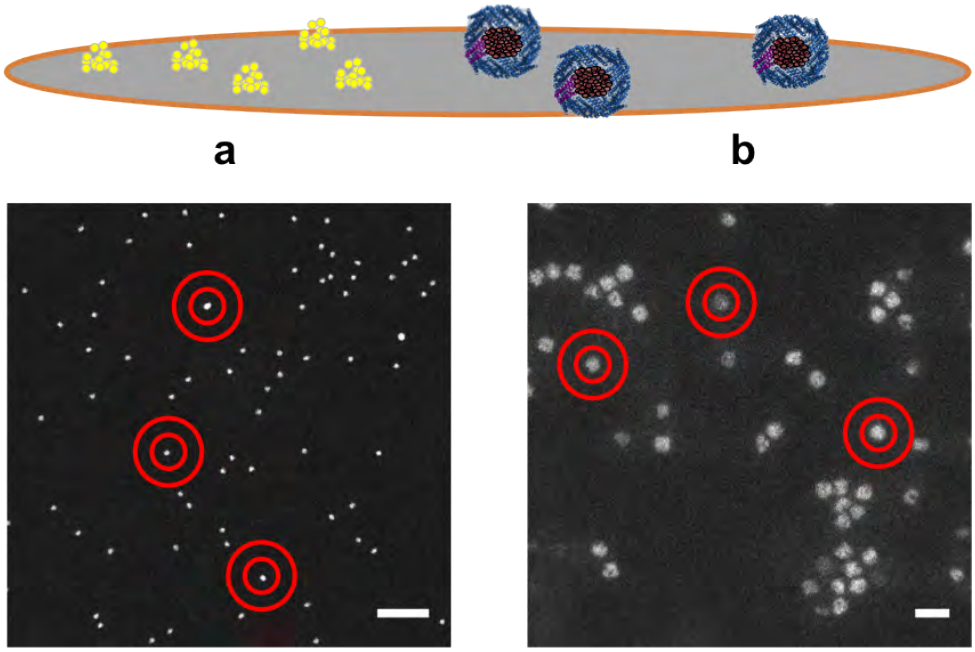

Figure 3.9: Size-selected gold clusters (a) are soft-landed onto one half of a carbon coated TEM grid and ferritin molecules are deposited from solution onto the other half (b). This preparation allows direct comparison between the two samples; the mono-dispersity in HAADF integrated intensity of the gold clusters enables them to be used as standards for quantitative studies of the ferritin. A background subtraction is performed on an individual basis through an annular template drawn around each feature (shown by the red rings). Scale bar = 15nm.

half with aluminium foil to prevent the clusters depositing on the entire substrate, as described in [9] and shown in the schematic in figure 3.9.

This resulted in carbon coated TEM grids with half the surface coated with gold clusters containing either 55 $\pm$ 3 or 147 $\pm$ 7 atoms per cluster. These grids could then be used to perform mass measurement by depositing ferritin on the other half, as discussed below.

Calculation of HAADF-STEM Integrated Intensity

All integrated intensity measurements were calculated with a background subtraction, which was performed on each individual feature by defining a ring around each core for localised background and subtracting the mean from the intensity of each pixel in the core (Figure 3.9).

The integrated intensity units can therefore be considered as arbitrary. Gold clusters and ferritin cores that were touching each other or that had agglomerated were excluded from this analysis. More discussion of the diameter of rings used to circle each feature is included in chapter 4, as this forms part of the results.

Equivalence Calculation

The relationship between the integrated intensities and size of the reference and target can be expressed as equation 3.1, where integrated intensities are I_1,I_2 the number of atoms in each cluster N_1, N_2, the atomic number of the two materials Z_1, Z_2 and a scattering coefficient which is characteristic of the microscope hardware.

$$\frac{I_1}{I_2} = (\frac{N_1}{N_2}) * (\frac{Z_1}{Z_2})^n \tag{3.1}$$

The scattering co-efficient, n, was determined for these conditions as 1.46 by Wang *et al.* [10, 11]. This was performed by depositing size-selected Au_{923} and Pd_{923} clusters on the same grid and imaging using the same microscope and conditions as in the work presented in this thesis. Once the integrated intensity has been measured, the only unknown variable in equation 3.1 was the co-efficient n, allowing it to be calculated.

In this caseI_1, N_1, and Z_1 can be taken as the gold signal, and I_2, N_2, and Z_2 as the ferritin signal. As an initial estimation the core can be assumed to be pure iron. However, if the oxide nature of the core is taken in to account, for any oxide formula there will be a certain number of iron (N_{Fe}), oxygen (N_O) and hydrogen (N_H) atoms. In order to calculate the number of iron atoms with this oxide correction (N_3) an equivalence factor (E) is used to modify the initial pure iron estimation (N_2).

$$\frac{1}{E} = N_{Fe}(\frac{Z_{Fe}}{Z_{Fe}})^n + N_H(\frac{Z_H}{Z_{Fe}})^n + N_O(\frac{Z_O}{Z_{Fe}})^n \tag{3.2}$$

$$N3 = N2 * E \tag{3.3}$$

For example, the calculation for the possible core formula of FeOOH would be, $\frac{1}{E} = 1 + (\frac{1}{26}^{1.46} + 2 * (\frac{8}{26}^{1.46})$ and therefore, N3= 0.731 * N2. The error in the measurement of n and I_1 is taken into account using the standard error of the distribution in the general error propagation equation.

3.3.2 Image Processing

All image processing was performed using either Gatan Digital Micrograph software or ImageJ/Fiji. This includes distance measurement and feature identification. Some images were contrast adjusted for display however quantitative analysis was only performed on raw, non-adjusted images.

In order to count particles, a pixel value threshold was set to include the relevant regions of interest and then the 'Analyze particles' command was used to count them. This was also used for sizing of particles, whereby the area of the region selected was also measured. For all diameter sizing, the diameter was calculated from assuming circular features. Average separation of particles was measured by drawing a circle round the relevant particles, measuring the centre of mass using ImageJ, calculating the distance between these and then subtracting the relevant radii. All fourier transform analysis was performed using the FFT command in Fiji. The indexing was then performed by measuring the predominant spots in the fourier transform.

Histograms were plotted using Plot for Mac (http://plot.micw.eu/) and the curve fitting function available within this software was used to fit gaussian distributions to the data.

3.4 Transmission Electron Microscopy

3.4.1 FEI Tecnai 12 and 20

In figure 3.10 a schematic is shown of a TEM in operation. An FEI Tecnai 12 BioTwin transmission electron microscope was used exclusively for all the negative stain imaging presented in chapter 6. This has a 120 kV tungsten filament for straight forward, relatively low magnification imaging. It is fitted with an FEI Eagle 4k x 4k CCD camera for image acquistion. A single tilt holder was used to secure a standard 3mm TEM grid in the microscope column.

A Tecnai 20 twin lens transmission electron microscope was used exclusively for cryo imaging, presented in chapter 6 of this thesis. This is fitted with a 200 kV LaB6 filament and an FEI Eagle 4k x 4k CCD camera

3.4.2 TEM Sample Preparation

Negative Staining

All grids were glow discharged prior to sample preparation this allows for easier sample wetting to the carbon substrate which ensures a more even coverage of the sample across the grid. This also has the advantage that molecules settle onto the substrate in a uniform manner. The effects of glow discharging on imaging results are discussed in detail in chapter 6.

The negative stain protocol used was standard for Uranyl acetate. 20μl of sample was drop cast onto a grid, left to adsorb for one minute, and then 50μl of 1% Uranyl Acetate stain was added and the overflow caught with blotting paper. This was then left to dry for 5mins and transferred into the microscope column.

In figure 3.11 a comparison of different imaging techniques (negative stain TEM, HAADF-

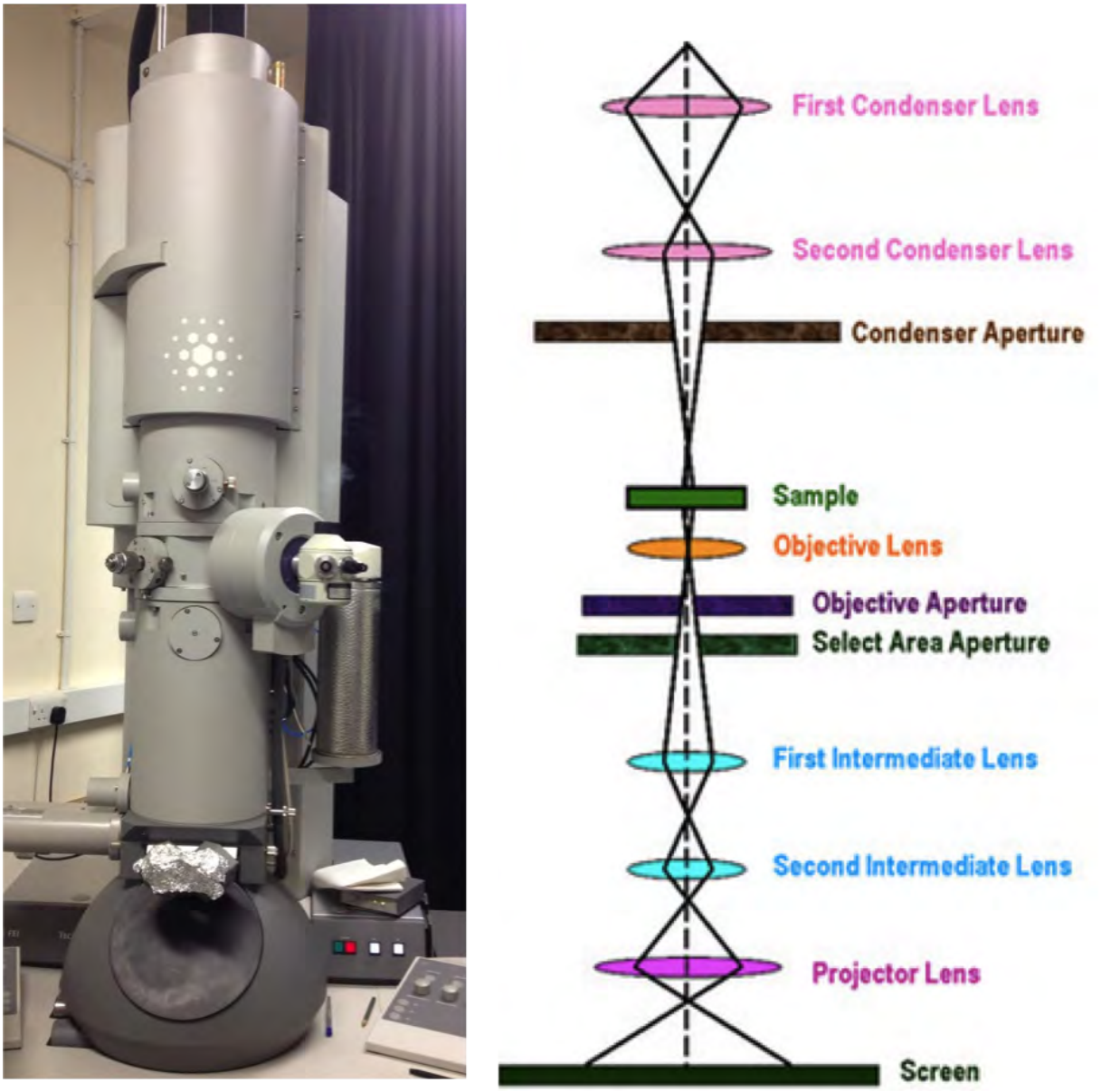

Figure 3.10: Schematic of TEM in operation alongside an image of the FEI Tecnai 20 TEM. Schematic modified from [12].

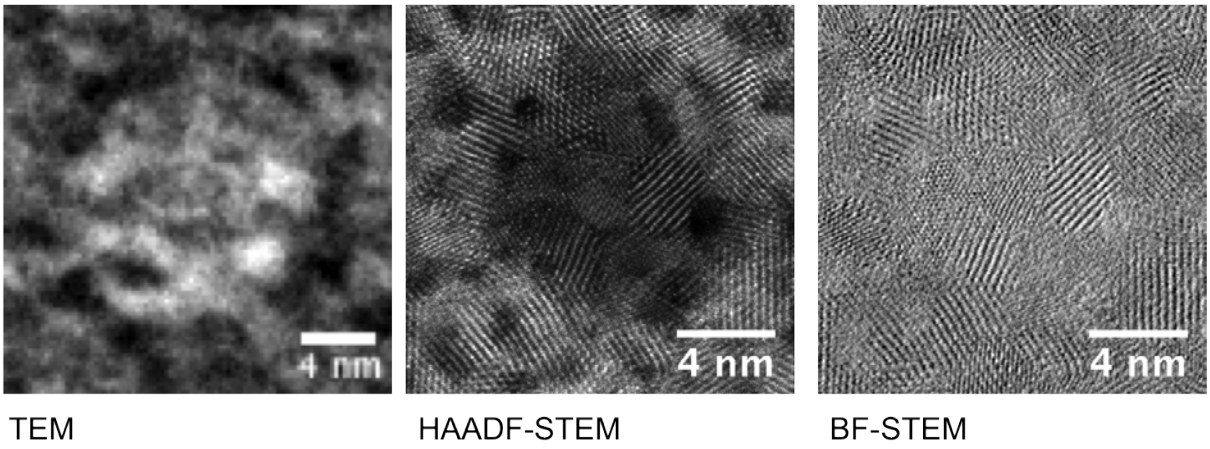

Figure 3.11: Comparison of a negative stained nanodisc imaged in TEM, HAADF-STEM and BF-STEM mode.

STEM, BF-STEM) of the same negatively stained nanodisc sample. The BF and HAADF images were obtained of the same disc simultaneously, the disc in the TEM image was on the same grid but not the same disc as localisation of exactly the same disc was not possible. It can be seen that atomic resolution of the stain can be seen in the STEM images, which are not visible in the TEM image. This highlights the change in contrast induced by the stain and shows a complete coverage over the molecule.

Nanogold Labelling

Ni-NTA Nanogold 5nm beads were purchased from Nanoprobes, Inc, USA. The 5nm gold particles are coated in a Ni-NTA ligand which is able to attach to his tags in any protein. This aids in localisation of the target protein, since the dense gold particle is relatively straight forward to image with TEM. A schematic showing the binding scheme is shown in figure 3.12.

The nanogold was added to the protein-SMALP sample using two different protocols, these are shown in figure 3.13. In the first protocol, the same concentration of Ni-NTA nanogold [$1X10^{-5}$ mg/ml] was added to the PagP protein [$1X10^{-5}$ mg/ml] in solution, left to mix and then deposited onto a substrate. In the second protocol, the protein sample was first deposited

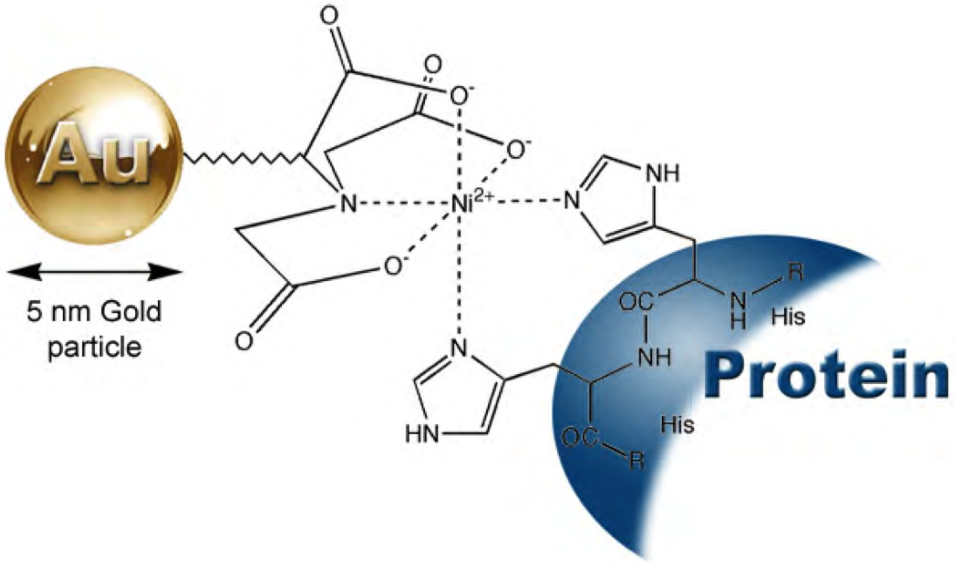

Figure 3.12: Schematic showing a Ni-NTA Nanogold 5nm attaching to a his-tag on a protein. This electron dense tag allows easier identification of the protein using electron microscopy. Figure adapted from [13].

onto the grid and then the Ni-NTA nanogold was also added and the two solutions were left for around 10 minutes to mix prior to rinsing and staining, following the protocol presented in [14].

3.4.3 TEM Imaging Protocol

A standard TEM imaging protocol was used, whereby the eucentric height was found using the wobbler. The beam was centred in intensity. The beam intensity was increased to be maximal and evenly distributed over the CCD, before images were acquired. For the work presented in Chapter 6, typical magnifications were from 30,000X - 100,000X. The main differences in operation between this microscope and the Jeol are a result of the lower resolution of this microscope and so there are less requirements for high precision sample settlement. This allows faster imaging and more specimens can be imaged in a shorter amount of time. There is also no need to perform beam showers, as carbon contamination is not a significant problem due to the less intense nature of the parallel electron beam compared to STEM imaging described in

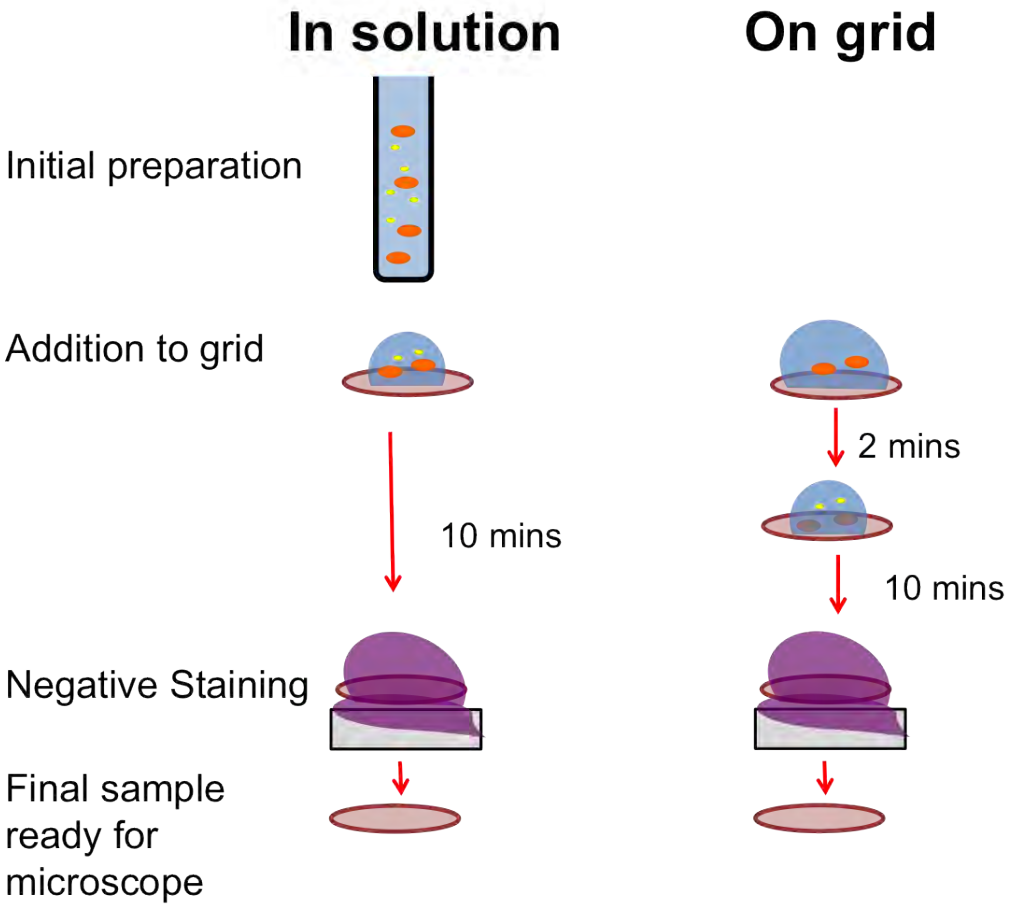

Figure 3.13: Schematic showing the two Nanogold adherence protocols. One is performed in solution prior to going on the EM grid, the other is performed on the grid.

section 3.2.2.

3.4.4 Cryo Sample Preparation

For this work a FEI Vitrobot was used to vitrify the samples which were then transferred into a Gatan 626 cryo transfer holder, see figure 3.14. The glow discharged grid is held by a pair of tweezers within an environmentally controlled chamber. The liquid nitrogen cooled ethane is held in a small pot within a workstation which is raised near to the tweezers. After applying around 5 μL of sample to the grid using a precision pipette, excess liquid is blotted away and the grid is robotically plunged into the ethane. The grid must then be rapidly transferred to the transfer station where it can be loaded into the liquid nitrogen cooled microscope grid holder. Once the grid is loaded into the holder a metal guard (labelled in figure 3.14C) is placed over the grid to protect it whilst it is rapidly entered into the microscope column. The temperature is then maintained by a liquid nitrogen cooled dewar at the end of the holder.

3.4.5 Cryo Imaging

Once transferred into the microscope and initial alignment was performed a low dose regime was used. This utilises the built in low dose software from FEI to minimise the number of electrons per square angstrom. The protocol for low dose imaging is shown in figure 3.15. There are three phases of imaging: search, focus and acquire. Initially a low magnification search is performed to identify a region of interest. Due to the low magnification at this stage the aim is to identify ice that appears thin and even. The magnification is then increased and the beam shifted to an area close to, but not on the region of interest. This allows the user to focus and align the beam.

All cryo-TEM images were analysed within the ImageJ/Fiji platforms after being imported from the low dose software. This included size and shape analysis as discussed above and also contrast enhancement.

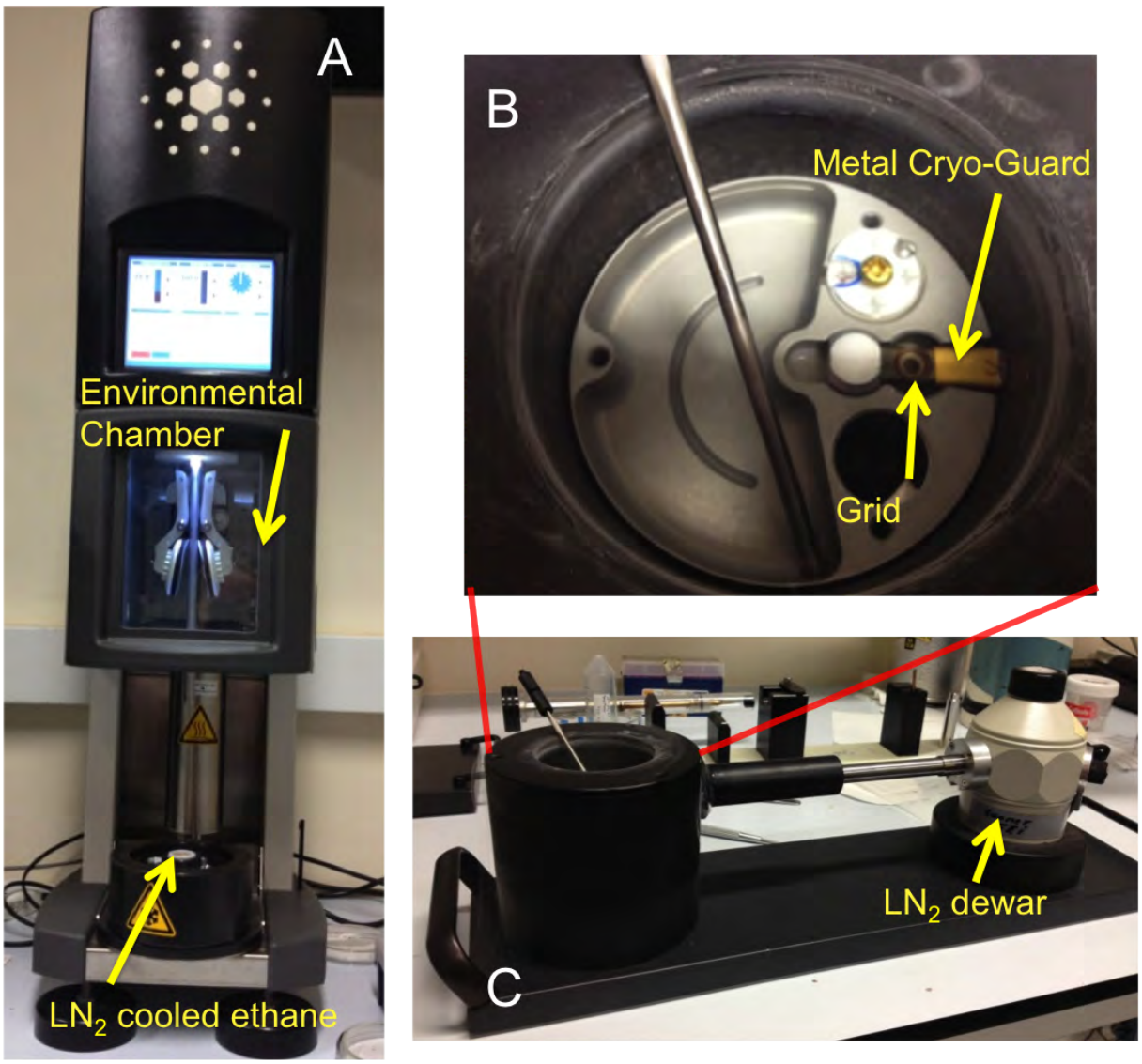

Figure 3.14: FEI Vitrobot Plunge Freezer (A) and Gatan 626 Cryo Transfer Holder (B,C). The glow discharged grid is held by a pair of tweezers within an environmentally controlled chamber (A). The sample is introduced to the grid via pipette onto one side of the grid. It is then blotted and plunged into liquid ethane cooled to -174. The tweezers can then be removed from their grip and the grid transferred into a grid holder by the user. A grid box containing the plunge frozen samples can be transferred into the station (B). The grid is then placed into the holder (C) and secured with a clipring. A metal guard is then placed over the grid to prevent ice formation on transfer into the microscope column.

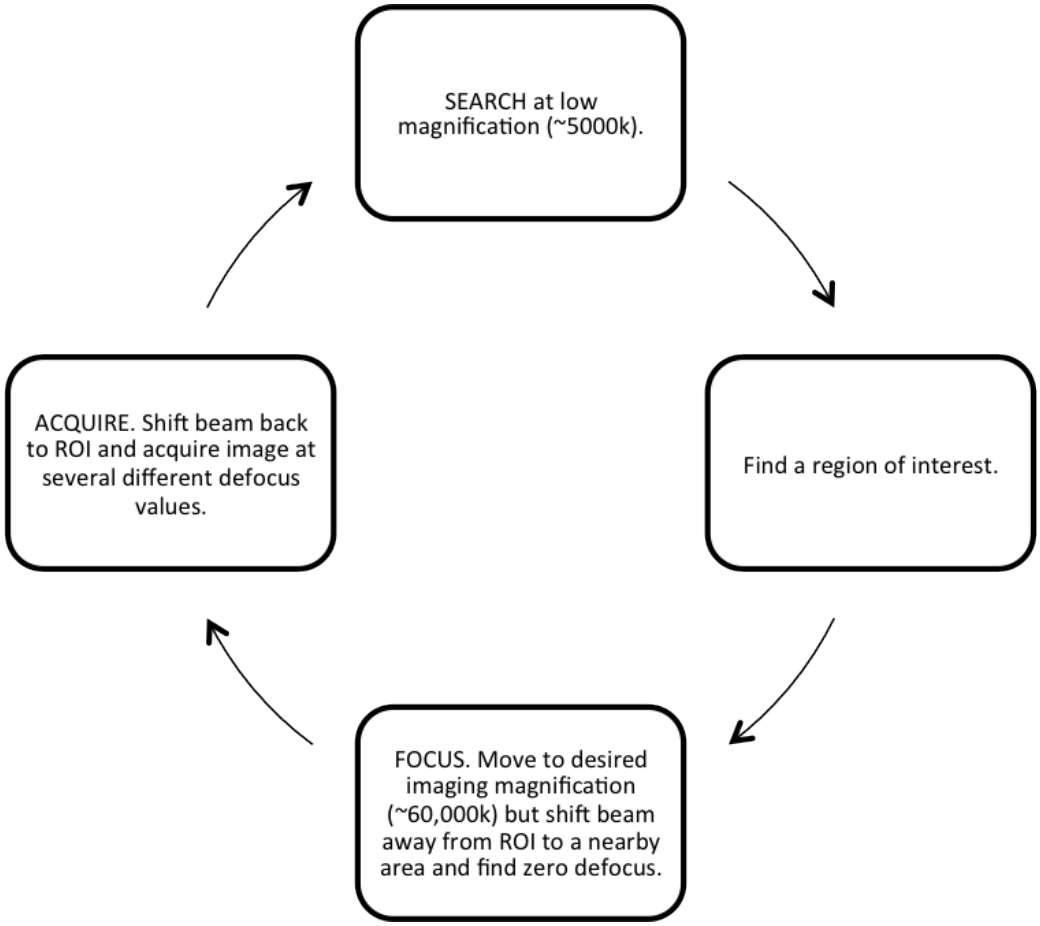

Figure 3.15: Low dose imaging protocol. There are three stages to imaging at low dose, an initial SEARCH phase followed by FOCUS and ACQUIRE. This helps to minimize the electron dose to the sample.

3.5 Biological Sample Preparation

For all samples, carbon coated TEM grids were used as a support. These were generally sourced from Agar Scientific (http://www.agarscientific.com/) or Electron Microscopy Sciences (EMS, http://www.emsdiasum.com/Microscopy/). Normally 300 mesh, i.e. 300 squares of carbon per 3mm grid. Both holey and continuous carbon were used for STEM and negative stain TEM and holey carbon was used exclusively for cryo-TEM.

3.5.1 Ferritin

Ferritin purified from equine spleen in saline solution (Sigma Aldrich UK), diluted to 0.5 mg/ml in de-ionised (DI) water, was used for all the results presented in chapter 4. For ferritin only samples, 2μl of ferritin solution was pipetted onto a grid, left to adsorb for 2 minutes then the excess solution removed by blotting and left to completely dry in air before being transferred into the electron microscope column. For the size-selected gold experiments, the grid was prepared by holding the grid perpendicular to a surface with a pair of opposable tweezers, and pipetting around 2μl of ferritin solution onto the non gold coated half nearest the surface, ensuring there were areas of the grid containing ferritin and gold only. This was again left to adsorb for 2 minutes before blotting and drying in air before being transferred into the electron microscope column. A new grid was prepared for each imaging session, to ensure the sample was not contaminated.

3.5.2 Alginates

All alginate sample preparation was performed by Richard Horniblow (School of Chemistry, University of Birmingham). The details are provided here for completeness.

Alginate samples were prepared by dialysing a 10ml solution of sodium alginate LFR 5/60 (0.1% (w/v)) dissolved in DI water against a solution of $FeCl_3 7H_20$ ([10mM], 750ml) for two hours. The sample was rinsed with distilled water by removing the dialysis bag and immersing it into a 750ml beaker of DI water for 2 hours. This removes any unbound iron prior to being prepared for the microscope. The same procedure was followed for samples including calcium rather than iron, however calcium was included in the incubation at a physiological concentration.

The grid preparation protocol for this sample was non-trivial due to the interaction of the sample with the carbon substrate, and is therefore described as preliminary work in the results section of chapter 5.

3.5.3 Membrane Proteins

All the sample preparation needed for the investigation of membrane proteins encapsulated by nano-discs was performed by Timothy Knowles (School of Cancer Sciences, University of Birmingham). The details are provided here for completeness.

In order to prepare a SMALP sample, two initial solutions had to be prepared - the copolymer and the required phospholipid. A 10% solution of styrene maleic acid (SMA) copolymer was prepared by dissolving 25g of copolymer in 250ml of NaOH [1 M]. The resulting solution was then refluxed for 2 hours and allowed to cool to room temperature. The material was then aliquoted into 50ml samples and placed in a freezer, and thawed and dialysed against the buffer solution before use. For the phospholipid, a 0.5 vol% solution was prepared by suspending 0.025 g lipid powder in 3.92 ml of phosphate buffer solution, then sonicating for 5 minutes to disperse the lipid in the solution. A solution consisting of 6.93 vol% copolymer in buffer was prepared and 1.08 ml added to the 3.92 ml lipid solution to reach a final copolymer con-

centration of 1.5 vol% and a final total volume of 5 ml. This mixed solution was shaken for approximately 1 min until clear.

The PagP proteins were first isolated and amplified in E.Coli before being isolated within the SMALP nanodisc, by adding the protein in membrane solution during the mixing process. This resulted in a PagP-SMALP concentration of 5mg/ml in buffer solution. Since the PagP contains a his tag, the resulting complex was passed through a nickel column in order to purify the sample and remove any 'empty' discs that did not contain protein.

As the SMALP nanodiscs contain no heavy atoms, the techniques of negative staining and nanogold labelling (described in chapter 2 above) were used as part of the imaging protocol for these samples.

3.6 Summary

The three microscopes, both STEM and TEM, that have been used to obtain all the images presented in this thesis have been described and technical detail of their operation discussed. The methods that have been used to prepare and image the biological samples of interest for this work have been explained in detail. Image analysis and interpretation protocols used to process the resulting images have also been presented. These methods therefore constitute all the procedures needed to attain the data presented in the following three results chapters.

References

[1] D. B. Williams and C. B. Carter. *Transmission electron microscopy: a textbook for materials science*. Springer, 2009.

[2] N. D. Browning, E. M. James, K. Kishida, I. Arslan, J. P. Buban, J. A. Zaborac, S. J. Pennycook, Y. Xin, and G. Duscher. Scanning transmission electron microscopy: an experimental tool for atomic scale interface science. *Reviews on Advanced Materials Science(Russia)*, 1(1):1–26, 2000.

[3] E. M. James and N. D. Browning. Practical aspects of atomic resolution imaging and analysis in STEM. *Ultramicroscopy*, 78(1):125–139, 1999.

[4] J. M. Rodenburg and E. B. Macak. Optimising the resolution of $tem/stem$ with the electron ronchigram. *Microscopy and Analysis*, pages 5–8, 2002.

[5] Jeol. *JEM-2100F Manual*. Jeol, 1 edition, 2009.

[6] R. F. Egerton, P. Li, and M. Malac. Radiation damage in the TEM and SEM. *Micron*, 35(6):399–409, 2004.

[7] S. Pratontep, S. J. Carroll, C. Xirouchaki, M. Streun, and R. E. Palmer. Size-selected cluster beam source based on radio frequency magnetron plasma sputtering and gas condensation. *Review of Scientific Instruments*, 76:045–103, 2005.

[8] R. E. Palmer, S. Pratontep, and H-G Boyen. Nanostructured surfaces from size-selected clusters. *Nature materials*, 2(7):443–448, 2003.

[9] Z. W. Wang, O. Toikkanen, F. Yin, Z. Y. Li, B. M. Quinn, and R. E. Palmer. Counting the atoms in supported, monolayer-protected gold clusters. *Journal of the American Chemical Society*, 132(9):2854–2855, 2010.

[10] Z. W. Wang and R. E. Palmer. Intensity calibration and atomic imaging of size-selected au and pd clusters in aberration-corrected HAADF-STEM. In *Journal of Physics: Conference Series*, volume 371, page 012010. IOP Publishing, 2012.

[11] Z. W. Wang, Z. Y. Li, S. J. Park, A. Abdela, D. Tang, and R. E. Palmer. Quantitative Z-contrast imaging in the scanning transmission electron microscope with size-selected clusters. *Physical Review B*, 84(7):073408, 2011.

[12] Yong Ding. *http://www.nanoscience.gatech.edu/research/Fundamental WWW, 2014.*

[13] NanoProbes Inc. http://www.nanoprobes.com/products/NTAgold.html. *WWW, 2014.*

[14] V. E. Pye, F. Beuron, C. A. Keetch, C. McKeown, C. V. Robinson, H. H. Meyer, X. Zhang, and P. S. Freemont. Structural insights into the p97-Ufd1-Npl4 complex. Proceedings of the National Academy of Sciences*, 104(2):467–472, 2007.*

Chapter 4

Aberration Corrected Scanning Transmission Electron Microscopy Study of Ferritin

4.1 Introduction

This chapter presents an atomic scale study of the iron storage protein, using scanning transmission electron microscopy (STEM). Size-selected gold clusters are used as mass standards to quantitatively assess the iron loading of individual ferritin proteins. This is demonstrated as the first application of a cluster-based mass standard approach to a biological system, providing a method to determine not only the metal loading of individual molecules but also cross-reference this with their morphology.

The high resolution imaging capabilities available, namely aberration corrected scanning transmission electron microscopy (STEM) have also allowed analysis of molecule packing and assembly on a substrate and studies of iron reduction from the inner core of ferritin proteins.

The results are presented in this chapter, along with a literature review of the biological sig-

nificance of ferritin and previous structural studies, including previous transmission electron microscopy imaging studies.

4.2 Literature Review

4.2.1 Iron Storage in the Body

Iron is one of the most abundant metals in the human body; this is due to its ability to engage in redox reactions, and so ability to hold on to oxygen [1, 2]. A number of proteins contain a 'heme' group which has an iron ion coordinated at the centre. Hemoglobin is the primary example of this, enabling oxygen transport around the body. Due to this essential role, maintaining the balance of iron in the body is important, and is mediated through a process known as 'iron homeostasis'. Figure 4.1 shows a schematic of the various mechanisms involved in this. It can be seen that iron is transported via a protein called transferrin, on entering the cell this attaches to a transferrin receptor that spans the membrane and then directs the protein through the cell and releases the protein and the iron. This iron forms a labile iron pool, which must be either used (eg. in haemoglobin) or sequestered within the iron storage protein, ferritin. Otherwise, DNA damaging free radicals can form.

Iron has two oxidation states in the body, ferrous (2+) and ferric (3+). Ferrous iron is soluble and has been shown to aid in the creation of dangerous free radicals in the body. An overloading of ferrous iron in the body has been linked to many diseases, such as Alzheimer's [4, 5, 3]. Whereas in the ferric state, iron is insoluble and inaccessible. In order to maintain iron stocks in this non-toxic, ferric oxidation state, the iron-storage protein ferritin has evolved.

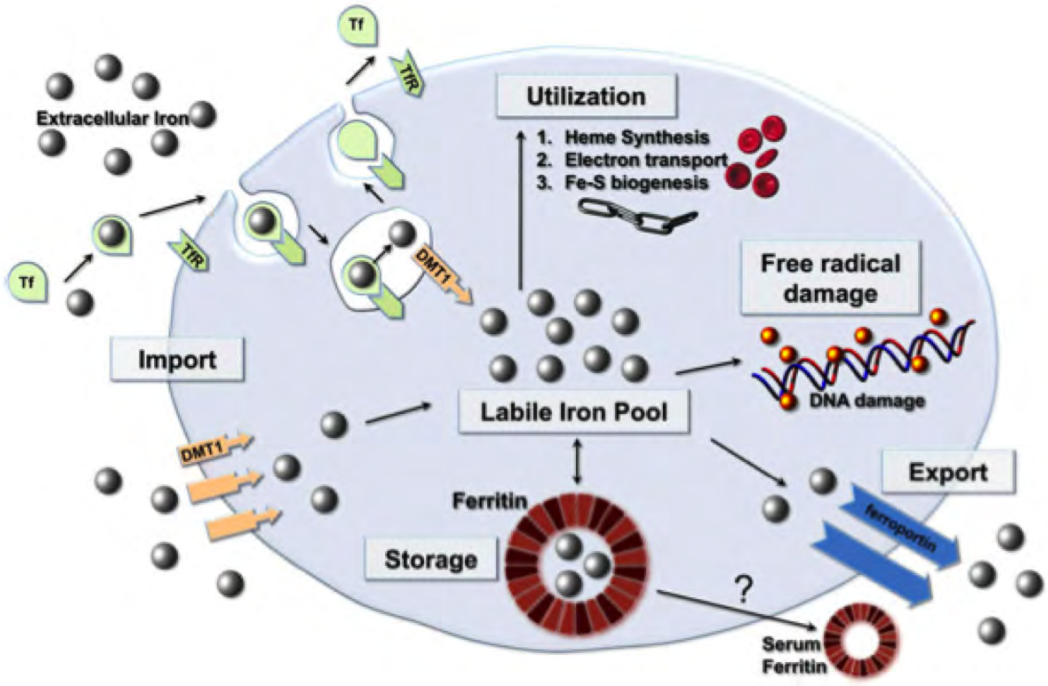

Figure 4.1: Schematic of ferritin behaviour in the body. Iron atoms are shown as grey spheres, with free radicals in yellow. DMT1 = divalent metal ion transporter 1, Tf = Transferrin, TfR = Transferrin receptor are all proteins involved in iron transport in the body. It can be seen that no free radicals are produced once iron is sequestered in the ferric form within ferritin. (Figure modified from [3])

4.2.2 Ferritin

Ferritin is a shell-like iron storage protein, (see figure 4.2) within which it is thought to be able to sequester up to 4500 iron atoms as an iron oxide core [6]. It is ubiquitous in the natural world, occurring not only in mammals but also in plants, bacteria and other species [7].

In the clinic, a ferritin serum assay is the most common method to determine iron levels within the body [8]. It can be used in order to diagnose iron deficiency disorders such as anaemia. The concentration of ferritin in the blood is broadly proportional to the amount of iron in the body overall. Ferritin expression assays are also used in the laboratory as an indication of iron content in the cells. For example, if ferritin expression has increased this normally means more iron has entered the cell [9].

The physical characterisation of ferritin generally falls into two areas - characterisation of the protein shell and characterisation of the iron oxide core. The protein shell is most often characterised by diffraction studies of the crystallised protein whereas electron microscopy is more appropriate for the core due to it's comparitively high atomic number and the direct imaging capability of the technique.

X-Ray Crystallography Characterisation

Due to the relative ease of crystallising ferritin, there have been numerous studies of the structure of ferritin, in both its filled and unfilled state. The unfilled state, which is the empty ferritin shell with no iron core residing within, is known as apoferritin. In one of the most cited papers, Harrison and Ford [10] describe the structure of the protein shell and relate this to its function as an iron storage facility. Although ferritins are present in many different mammalian and plant forms, they all exhibit very similar structural properties. For example, in the early 1980s the structure of human spleen apoferritin was refined to 2.8 $\mathring{A}$ and compared to that of horse spleen ferritin [11], there was only a 14% difference in the amino acid composition [12].

There are 24 symmetrical subunits of two types, either *h* or *l*, which each have different roles within the protein. These form a symmetrical structure with 8 inter subunit gaps providing entry and exit channels for the iron. The current model assumes that iron enters the protein in the 2+ form and that oxidation takes place whilst travelling through a *h* subunit after which core growth is catalysed by the *l* subunits. The amount of *h* and *l* subunits (the *h*/*l* ratio) differs in different areas of the body, depending on whether there is more need for iron storage (the spleen) or iron mobility (the heart). This also affects the shape of the iron core, which is discussed more in the next section.

The iron oxide core is much more variable in size and shape, depending on the type of ferritin but also time of purification. Electron microscopy is therefore a more useful technique as it is

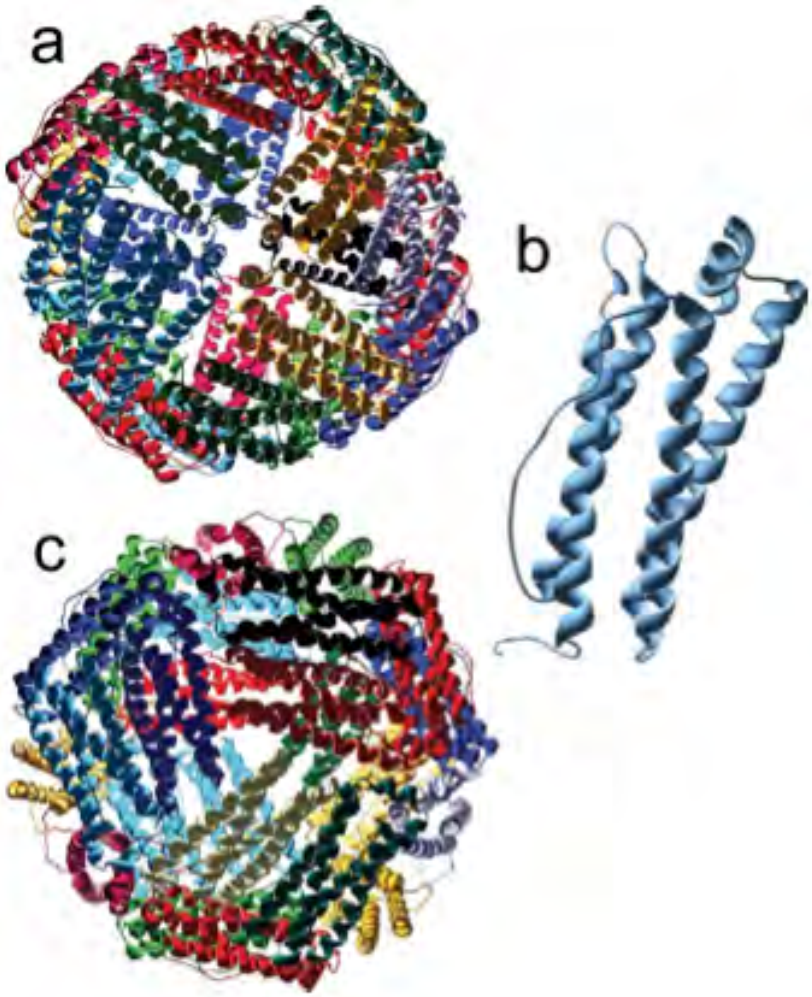

Figure 4.2: Three dimensional crystal structure of ferritin. Ferritin is a spherical, hollow protein which contains an iron oxide core capable of holding up to 4500 iron atoms (iron core not shown). This shows the human H-chain ferritin viewed from the four-fold symmetry axis (a) and three fold (c). b shows a single h subunit. Figure reproduced from [7]

possible to image individual cores rather than diffraction patterns of many hundreds, as in X-ray crystallography.

Electron Microscopy

A comprehensive review on ferritin by Massover [13] details the results achieved in the second half of the 20th century. However, there has been more recent work using the scanning transmission electron microscope (STEM) that has advanced understanding of the core structure and growth process [14, 15]. The dense iron core of ferritin lends itself to the z-contrast imaging mechanism of HAADF-STEM and this technique could provide insight into the core growth and morphology.

The exact oxide stoichiometry of the core is not known, although the closest approximation is believed to be ferrihydrite ($Fe_5HO_8 \bullet 4H_2O$) [14]. This is a naturally occurring mineral with some studies having been performed on the nano-crystalline structure [16]. This is challenging as most characterisation techniques depend on long-range order, resulting in accurate diffraction patterns. However, nanocrystalline materials inherently do not have long-range order and so Michel *et al.* achieved a structure by modelling the pair distribution function.

Pan *et al.* have performed aberration corrected HAADF-STEM on isolated ferritin cores fixed in human tissue [14]. This was the first example of Cs corrected electron imaging on ferritin cores. A polycrystalline core morphology was found, rather than a single sphere. A schematic of this proposed morphology is shown in Figure 4.3. STEM-EELS was also performed, which provides chemical specification. This was used along with standards to assess the iron loading and stoichiometry of the protein core. Quantitative measurements were performed and the EELS signal was calibrated to the amount of iron per ferritin molecule, the mean was found to be around 1200 with a gaussian distribution.

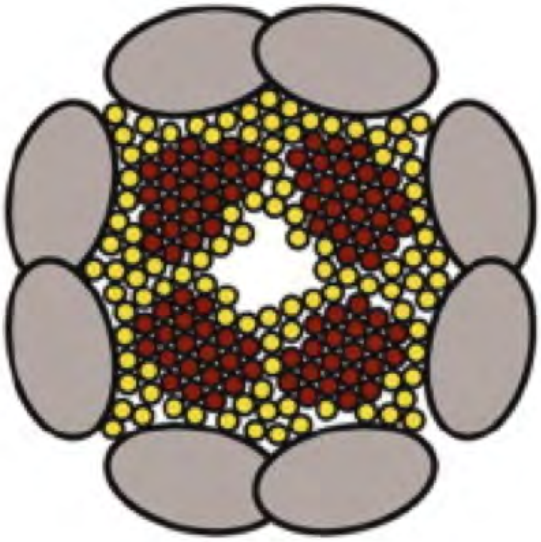

Figure 4.3: Sub-unit morphology of ferritin iron core proposed by Pan *et al*. Iron atoms enter through inter sub unit spaces in the protein and fill in separate areas which correspond to their entry. This results in an iron core with eight 'sub-units' rather than a single sphere. Figure modified from [14]

Recently, work has been published demonstrating high resolution aberration corrected STEM of ferritin isolated in a liquid environment [17]. The silicon nitride liquid cells discussed in Chapter 2 are too thick (50-500nm) to allow atomic scale imaging, and so this work was performed by using two graphene sheets to encapsulate a layer of ferritin in solution within the microscope vacuum. This allowed atomic scale imaging of ferritin whilst in the liquid state, along with EELS spectroscopy to identify iron, oxygen and nitrogen localisation. This demonstration is a promising step towards atomic resolution imaging of biological samples without the need for dehydration.

Similar *uncorrected* HAADF-STEM studies have recently been published of magnetic nanoparticles synthesised using recombinant ferritin as a template [18]. By calibrating the HAADF-STEM intensity to the EELS signal, it was found that up to 8,500 iron atoms in the form of magnetite could be found within a single ferritin 'cage'. This higher maximum number of iron atoms per core was attributed to the nature of the sample, being nanoparticles synthesised within ferritin rather than 'natural' ferritin.

Lopez *et al.* have recently performed *uncorrected* HAADF-STEM on ferritins from different

areas of the body, in order to assess changes in core morphology due to different subunit ratios within the protein shell [15]. It was found that ferritin with a high amount of *l* subunits were able to store more iron in discrete cores, whereas proteins engineered to consist of *h* units only were unable to store iron. The shape of the core was also found to vary depending on the *h/l* ratio within the ferritin protein (which depends on whereabouts the ferritin originates from in the body). Non-symmetrical (c-like shapes) cores were found more often in proteins with majority *l* subunits, and so an unsymmetrical number of binding sites when partially filled.

As well as structural studies of the core itself ferritin has a number of uses in the wider field. It has been suggested as a potential electron dense marker for cryo-TEM [19] in the same way as green fluorescent protein (GFP) is used in fluorescence microscopy. This is because the ferritin protein can be genetically engineered onto most molecular targets that would otherwise be difficult to identify in an EM image. The iron dense core would provide much better contrast and allow for advanced imaging techniques to be performed, such as cryo-tomography. One can imagine a case where differently loaded ferritin cores are added at various stages of a biological process in order to identify a particular component at different time points. Detailed knowledge of the core and how it is formed would aid development of this type of methodology.

4.3 Aims

The initial aim of this project was to perform aberration corrected electron microscopy of ferritin assemblies, and gain high resolution atomic images in order to gain a better understanding of the structure and formation of the iron core within the ferritin protein.

Further aims were to use size-selected clusters manufactured in the Nanoscale Physics Research Laboratory as mass balances for quantifying the amount of iron in the ferritin cores using the methods described in Chapter 2. This is, to the authors knowledge, the first application of this

mass measurement technique to a biological molecule.

A subsequent aim was to reduce the amount of iron within the ferritin molecules, in order to assess the impact on size and shape of the iron oxide core.

4.4 Results and Discussion

4.4.1 HAADF-STEM Imaging of Individual Ferritin Molecules

Imaging of individual ferritin molecules adsorbed onto a carbon substrate was performed as described in Chapter 3. Iron has a relatively low atomic number (26) compared to materials commonly studies with STEM, such as gold (79). Taking into account the dependance of intensity on atomic number (equation 4.1)

$$I \sim z^{1.46} \tag{4.1}$$

this means that it is not trivial to achieve atomic resolution images of iron samples. This is compounded by the organic material surrounding the core and in the buffer solution increasing contamination and worsening imaging conditions. This means that corrector alignment and sample stability are paramount for successful imaging, see Chapter 3 for further detail.

Low Magnification Imaging

In order to assess a large population of ferritin molecules, low magnification images (from 50k - 800k xM) were taken, each showing tens of molecules per image (see figure 4.4). From the image it can be seen that the molecules often group together on the substrate, most probably attracted to each other during the drying process. On a macro scale, the proteins in solution spread evenly across the grid with little crystallisation of the buffer solution.

Figure 4.4 also demonstrates the range of intensities of proteins. Since intensity is proportional to atomic number and the number of atoms (equation 4.1) and it is known that the elemental composition is broadly the same across the population [10], this variation is due to differing iron loadings from molecule to molecule. Comparing the cores labelled 1 and 2 in figure 4.4, it should be clear that core 1 contains less iron than core 2 since core 2 has a higher HAADF intensity and therefore a higher iron content.

The mean diameter of the protein was 7 nm with a standard deviation of 0.5 nm. This was calculated by measuring the area and assuming each core was circular. Figure 4.5 shows a histogram of the diameter of 151 ferritin cores. A minimum diameter of 5.3 nm and a maximum of 8.6 nm was found which is due to the natural variation in iron loading and therefore core shape/size. However, it can also be seen that the distribution has four peaks with a dominant one at 7nm. This suggests that the cores have preferential iron loading states and this is explored in subsequent sections of this chapter.

The diversity of shape within a ferritin core population is apparent in these low magnification images, a range of structures can be found such as the 'C-like' (core 3) and sphere (cores 1 and 2) structures discussed by [15] and highlighted in the image. A significant difference in the intensity of each core can also be seen, which corresponds to a varying loading of iron atoms in each core.

High Magnification Imaging

Figure 4.6 shows a single ferritin core with each bright spot in the image representing a single atomic column of iron within the ferritin core. The intensity of the spot being proportional to how many atoms are in the column, from one to tens of atoms. Single iron atoms can also be seen surrounding the iron core, highlighted by a red arrow in figure 4.6. The fourier transform

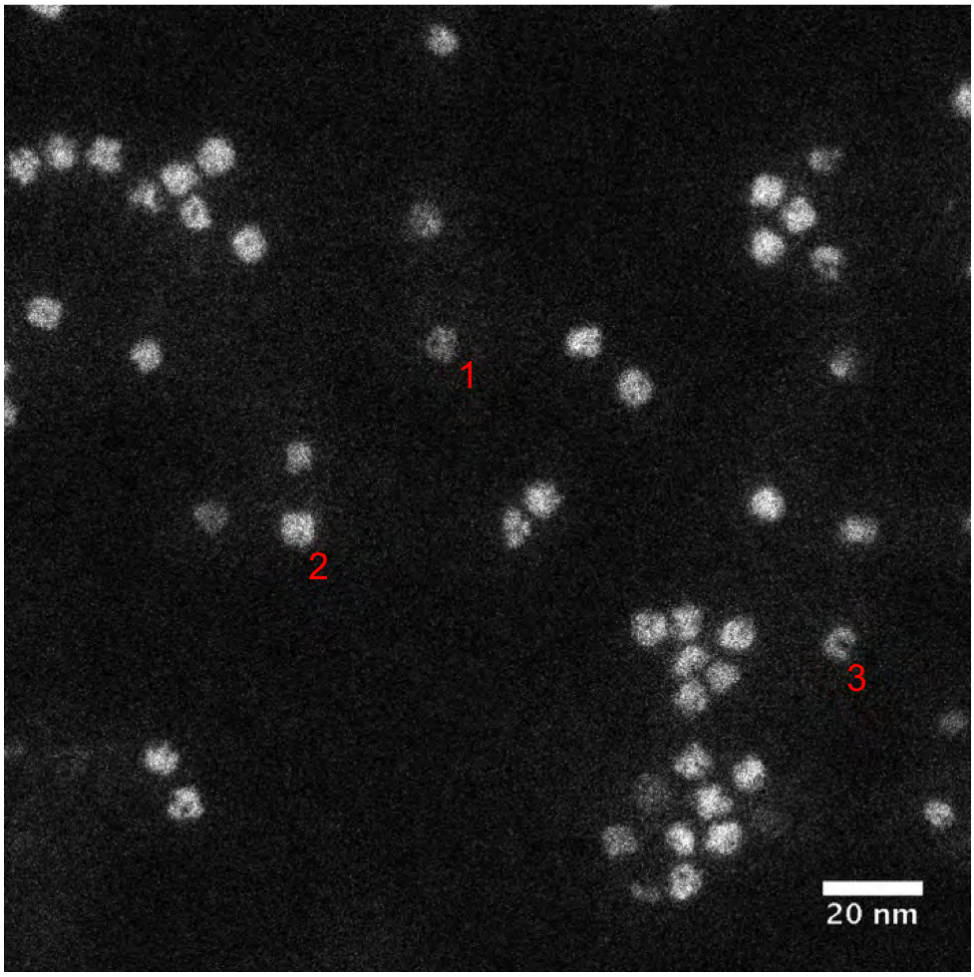

Figure 4.4: Low magnifiifcation HAADF-STEM images demonstrate the diversity of shape and intensity of ferritin cores. Both spherical (1,2) and 'c-like' (3) cores can be seen. A significant difference in intensity can be seen if core 1 and 2 are compared, representing a variation in iron loading.

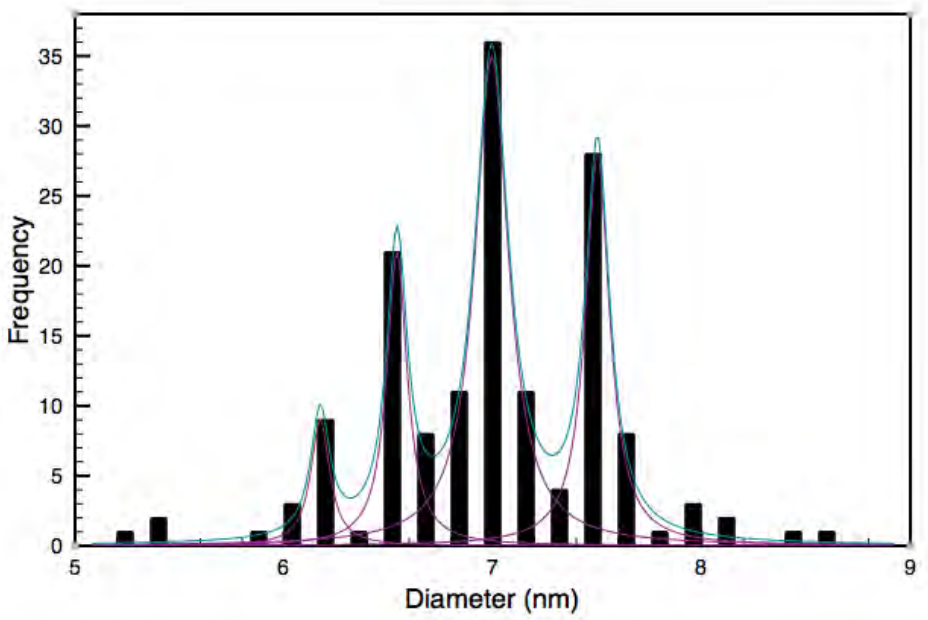

Figure 4.5: Histogram showing the measured diameter of 151 ferritin cores adsorbed onto a carbon substrate. The mean value ($\pm$ standard deviation) was 7 $\pm$ 0.5 nm. Four clear peaks can be seen, which indicate that there are preferential iron loading states for ferritin. The purple lines are gaussian components, with a combined gaussian in blue.

of a high resolution image of a ferritin core shows interplanar spacings of 0.25 and 0.26 nm which matches those found by Pan *et. al.* [14], an example is shown in figure 4.7.

In Figure 4.8 an example of the core subunit morphology described by Pan *et al.* [14] can be seen. In this model, the iron enters through channels between each subunit in the protein, which means there are eight entry points into the central cavity. Pan *et al.* propose that the iron pool close to the exit of each channel, meaning the iron core forms in subunits that grow to form a single sphere at higher capacity. This morphology is not observed in every ferritin core, some are more like a single crystalline sphere or just one of the subunits. This provides the motivation for quantification of the images, as cross-referencing with HAADF-STEM images allows size and shape comparison and an investigation into whether iron loading affects the shape. However, before quantification could be performed it was necessary to establish whether the protein shell was complete or not (i.e. damaged) at the time of imaging.

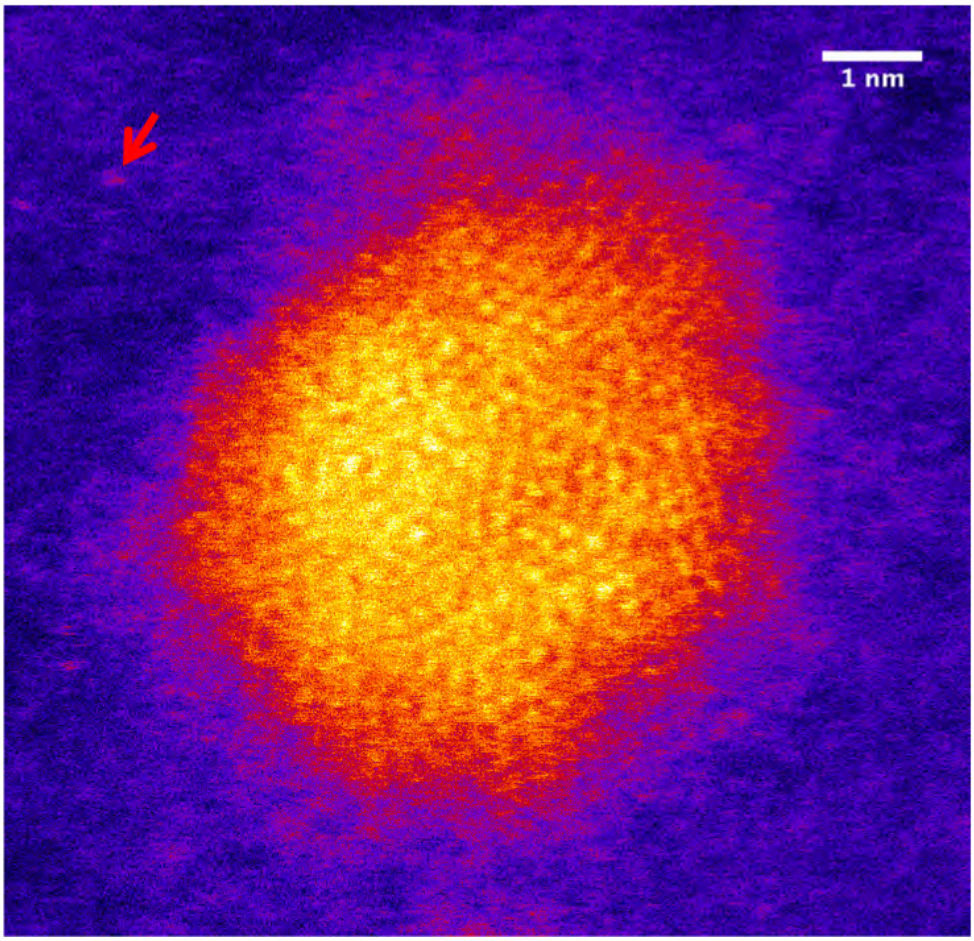

Figure 4.6: High resolution image of a single ferritin core showing atomic lattice structure. Atomic columns can be seen within the ferritin core as single bright dots. The intensity of the dot is proportional to the number of atoms within the column. Single iron atoms can also be seen surrounding the core, an example of this is highlighted by the red arrow.

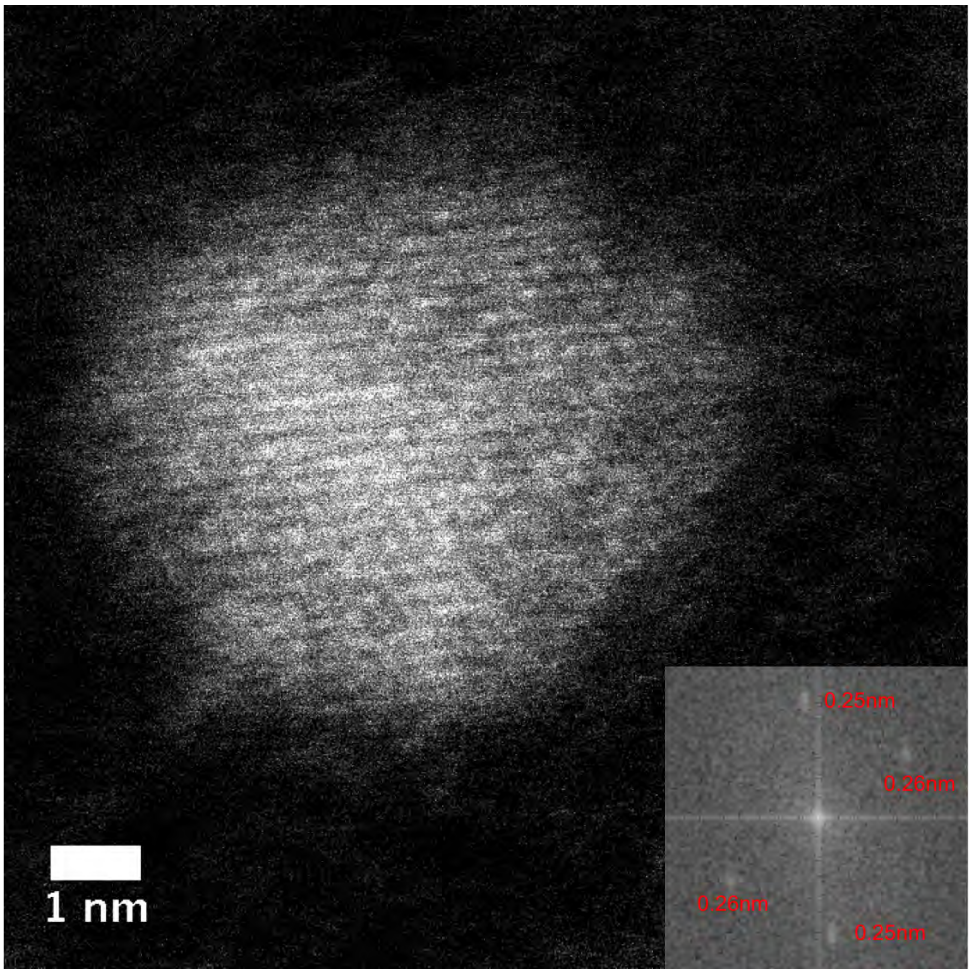

Figure 4.7: Fourier transform of a high resolution HAADF-STEM image of a ferritin core. Interplanar spacings are measured as 0.25 and 0.26 nm which correspond with those found by Pan *et. al.*.

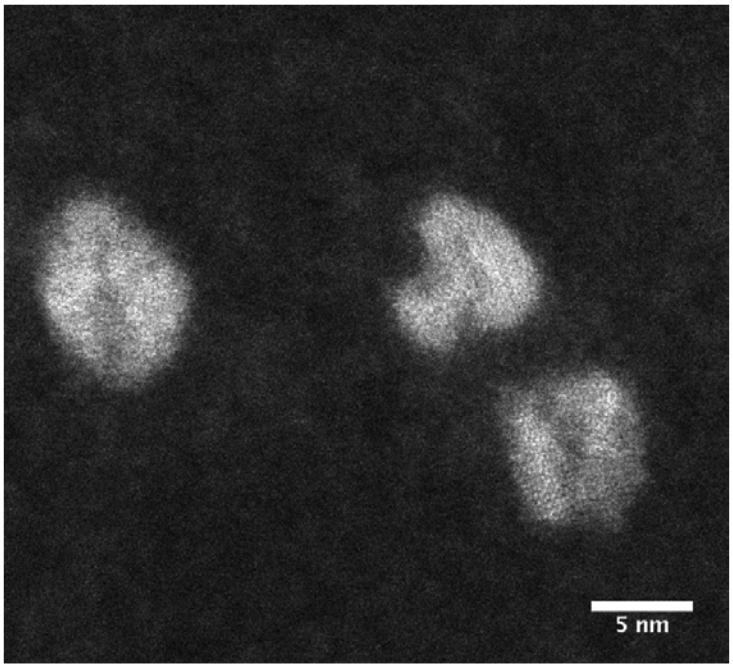

Figure 4.8: High resolution HAADF-STEM image showing ferritin cores with variable morphologies. The cores have some internal structure with a lower intensity centre and in the case of the upper right core a non-symmetrical shape.

Resolving the Protein Shell

Previous studies of ferritin have focused on either the ferritin protein shell or the iron oxide core, but have not usually considered both with the same technique and data. As the elements that make up the protein have a low atomic number, the contrast in the image is low and any signal is obscured by the background intensity. However, with intensity profile analysis the protein can convincingly be found. In figure 4.9 an intensity profile across the gap between two neighbouring ferritin cores is shown. It can be seen that there is a clear increase in signal through the area where protein would be expected to be present, immediately surrounding the cores.

This can also be seen in profiles of individual cores. Figure 4.10 shows an intensity profile taken radially from the centre of a single ferritin core. Although the effect is less pronounced there is a 'step' in the profile that is visible and again corresponds to where one would expect to find the protein shell. This demonstrates that the protein is still intact, at least in part, after imaging with

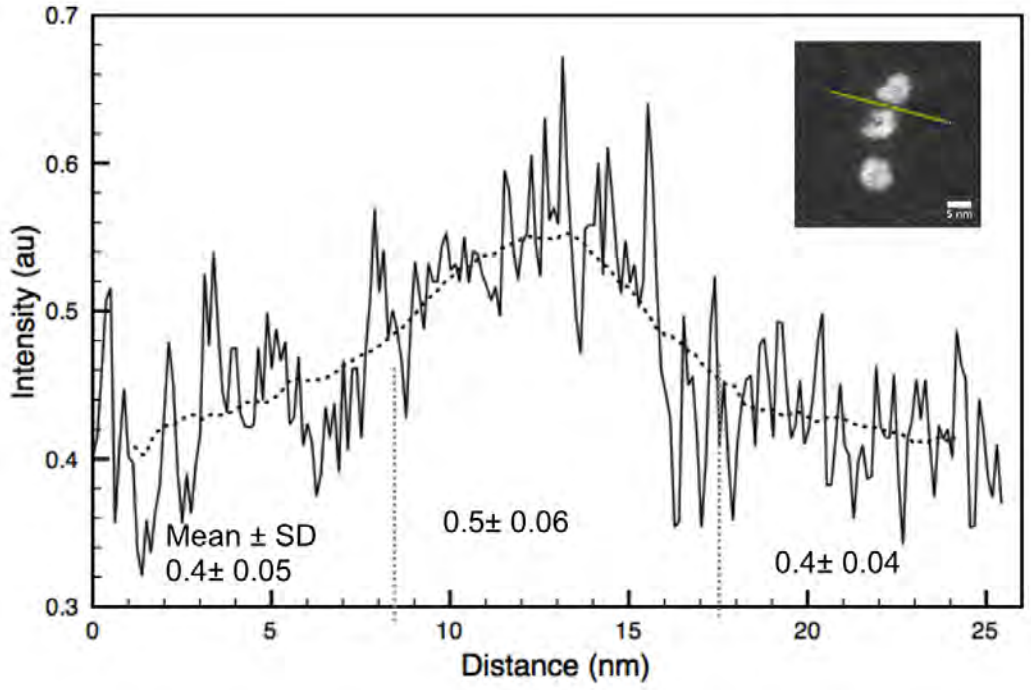

Figure 4.9: HAADF-STEM intensity profile of the protein shell surrounding the iron oxide core. The inset shows a HAADF-STEM image of three ferritin cores, with a line profile (1nm in width) taken between two in close proximity. Even though the elemental composition of the protein is low in atomic number, the intensity profile clearly shows a peak where one would expect the protein shell to be between the two iron cores.

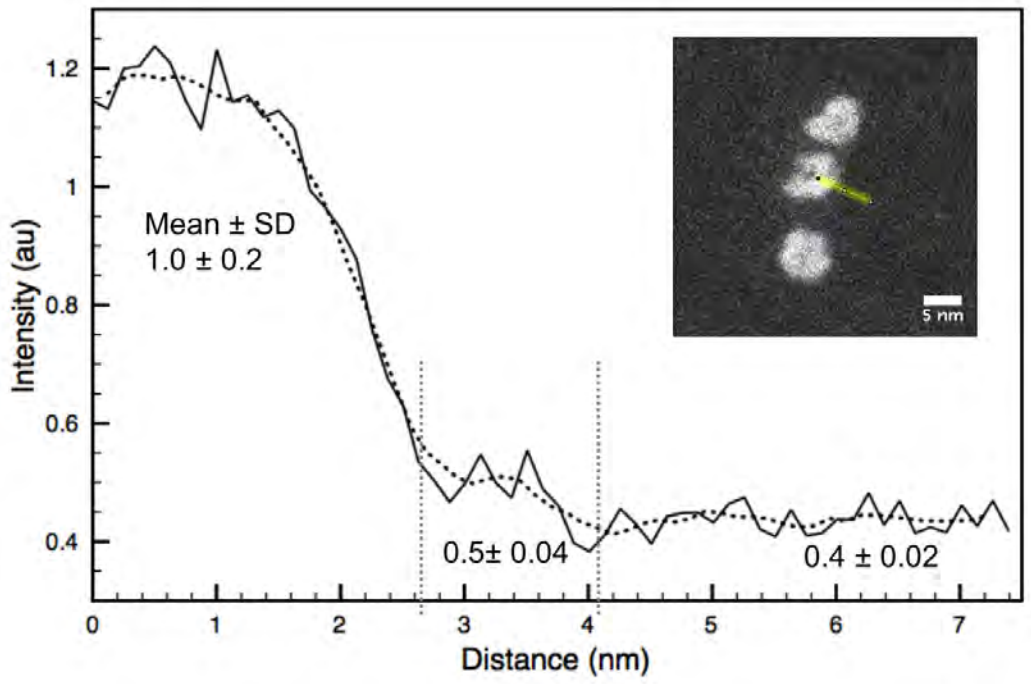

Figure 4.10: Radial HAADF-STEM intensity profile from the core centre. Even taking into account the low z number of the material surrounding the core, the intensity profile clearly shows a protein shell where the mean intensity is slightly higher.

the high-energy electron beam. It is therefore necessary to take into account in any quantitative analysis of the cores. More detail on how this is achieved is described in later sections.

Width of the Protein Shell

The separation of ferritin cores within close packed networks was measured by taking the centre of mass, measuring the distance between the two, then subtracting the core width of both. A histogram of the separation distance was then plotted and the result is shown in figure 4.11. It can be seen that the mean separation is around 1nm (ie a protein width of 0.5nm), compared to a protein width of around 1nm on isolated cores described in the previous section. In Figure 4.11(b) there is a broadly gaussian distribution centered around 1.3nm. Around 6% of the

measured separations were negative numbers, indicating that these are overlapping cores and meaning the vast majority (94%) of cores are separated. This will be due to the protein shell surrounding the core. It could be assumed that half of that value would be the protein width (0.65nm) on either side of the core. However the previous analysis of isolated ferritin cores suggests this is too small.

This suggests that when two proteins come in proximity to each other, they become compressed together and therefore the diameter of the protein surrounding the core decreases. There does not seem to be an effect on the iron core, just the protein shell. This means when performing quantification of the iron content of the cores, the contribution of the protein must be taken into account, bearing in mind the protein is above and below the core as seen in the image, in addition to surrounding it. In this work, a larger region of interest was measured in order to include the whole protein and then the contribution was subtracted from the signal.

This is supported by integrated intensity analysis of the cores with increasing sample area, which is presented by figure 4.12. In the figure, the integrated intensity increases to a point and then fluctuates once the sampling region has become too large. This gives an optimum inner region diameter of 12nm to use for further analysis, including the quantitative mass standard study presented below.

4.4.2 Quantifying Iron Loading Using Gold Clusters

As described in the literature review in chapter two, gold clusters have previously been used as mass standards for chemical samples such as ligand protected gold clusters [20] and palladium catalyst nanoparticles [21]. Here, the first application of this technique to a biological molecule is presented.

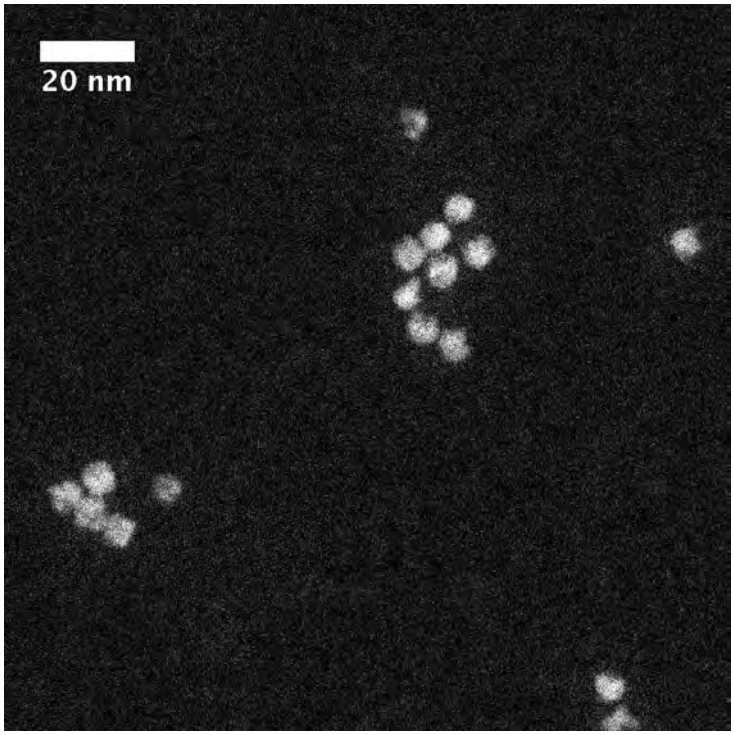

(a) HAADF-STEM image of closely packed ferritin on a grid

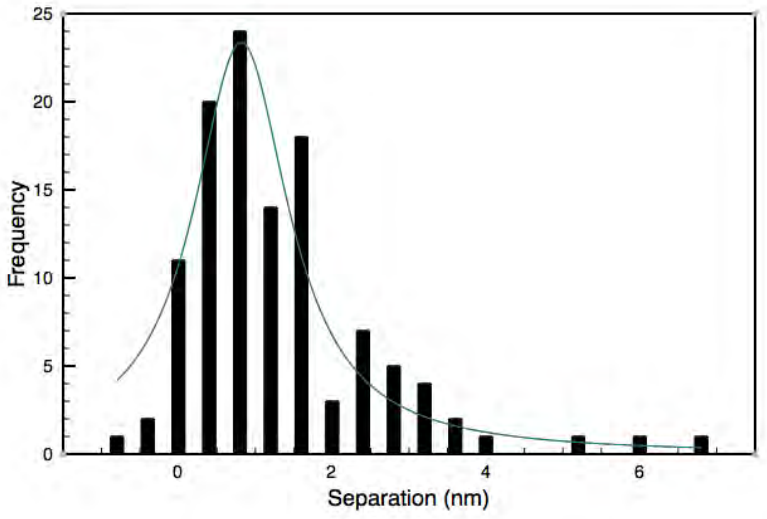

(b) Histogram of separation distance between two cores

Figure 4.11: The mean separation distance of ferritin cores when the cores are packed close together is 1.3nm. Around 6% of the measured separations were negative, which implied the cores were touching and so the vast majority of close packed cores are separated by some distance.

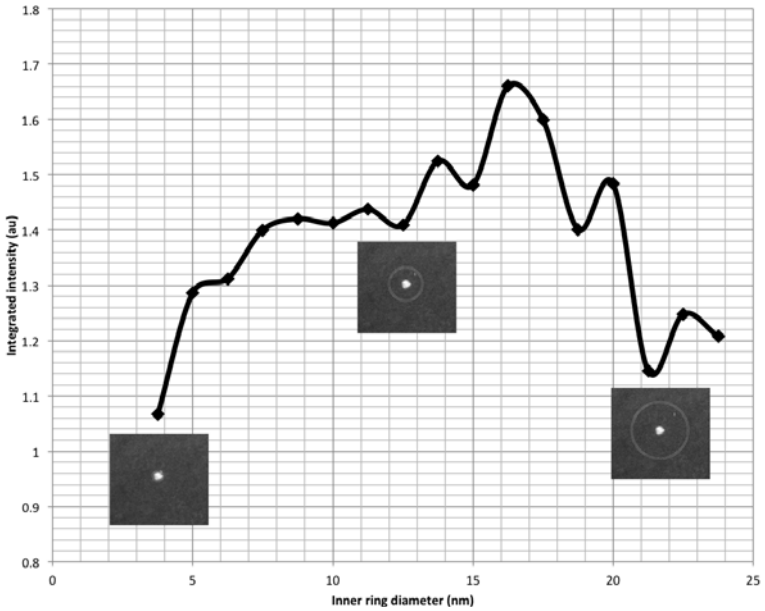

Figure 4.12: The sampling area for the integrated intensity was varied from 3.5 to 24 nm in diameter. It can be seen that the intensity increases until reaching stability around 12nm, after this the signal fluctuates due to the sample size being too large.

The Interaction of Gold with Ferritin on the Grid

In order to perform mass calibration with size-selected gold clusters, it was first necessary to confirm the nature of interaction between gold clusters and ferritin on a carbon coated electron microscopy grid. Ferritin was deposited from solution onto a grid pre-deposited with Au_{55} size-selected clusters. HAADF-STEM imaging (Figure 4.13) revealed that the ferritin (or most probably the buffer solution it is suspended in) mobilises the gold clusters, resulting in the clusters interacting with the ferritin and surrounding the molecule. There were two different interactions of the ferritin with the gold on the same grid. That shown in figure 4.13 where the gold in some cases covers the ferritin, and that shown in figure 4.14 where a dense layer of Au_{55} surrounding ferritin protein cores is presented. It can be seen that the gold surrounds the cores leaving a 'halo' (labelled 1 in the diagram), presumed to be due to the protein shell surrounding the core. This is supported by the 'empty' areas (labelled 2 in the diagram), which are assumed to be apo-ferritin. Here, the gold clusters are effectively acting as a negative stain for the ferritin cores. This highlights the fact that when imaging ferritin on a grid, there is a high probability

that these 'empty' proteins are also present but will not be taken into account in quantitative studies because they cannot be measured.

The various interactions shown in Figures 4.13 and 4.14 make any quantitative analysis of the images extremely challenging as for this ferritin molecules must be well separated. It was therefore necessary to use a half covered grid, one side with gold and the other with ferritin, to separate the samples whilst maintaining the same imaging conditions for both. This technique has been used before and is discussed further in chapter 3.

Two sizes of size-selected gold clusters were chosen as the mass standards, Au_{55} and Au_{147}, two of the 'magic numbers' of gold cluster sizes, discussed in detail in Chapter 3. This was so that a comparison could be made between the two values obtained.

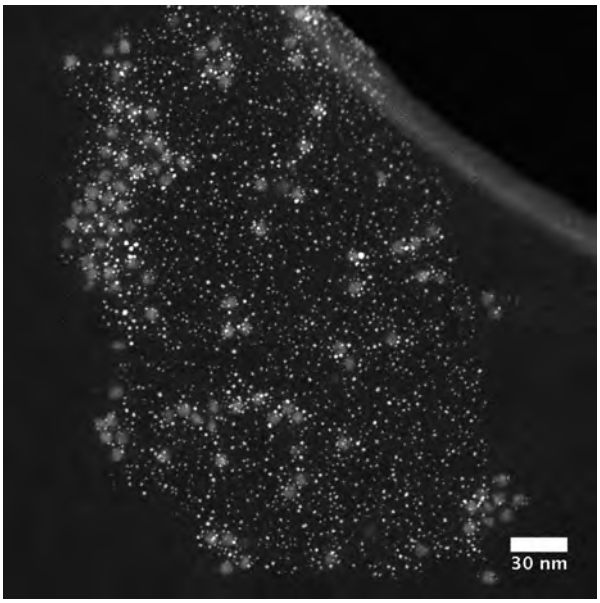

(a) Low magnification HAADF-STEM image of ferritin and gold clusters on the same substrate

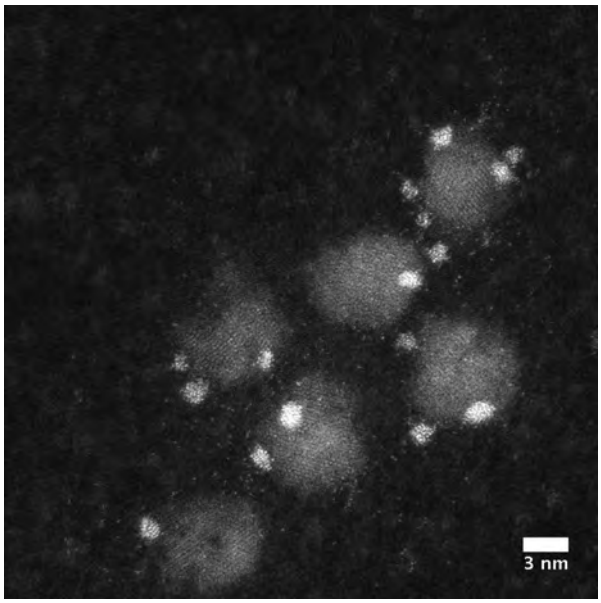

(b) 6 ferritin cores surrounded by gold clusters

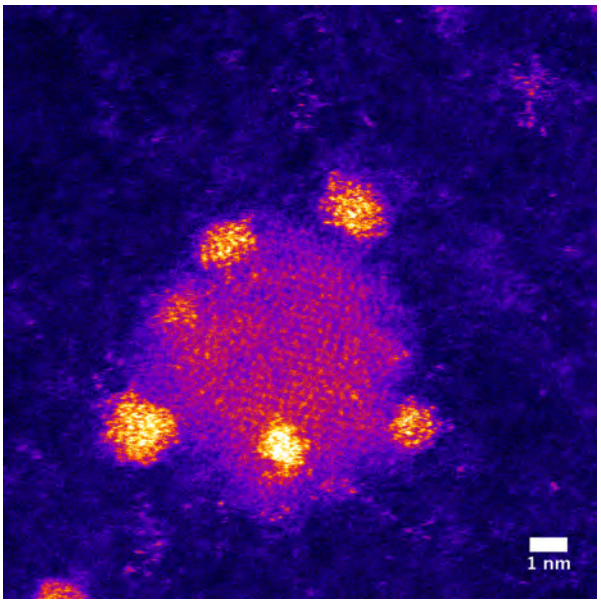

(c) Single ferritin core surrounded by gold clusters (false coloured)

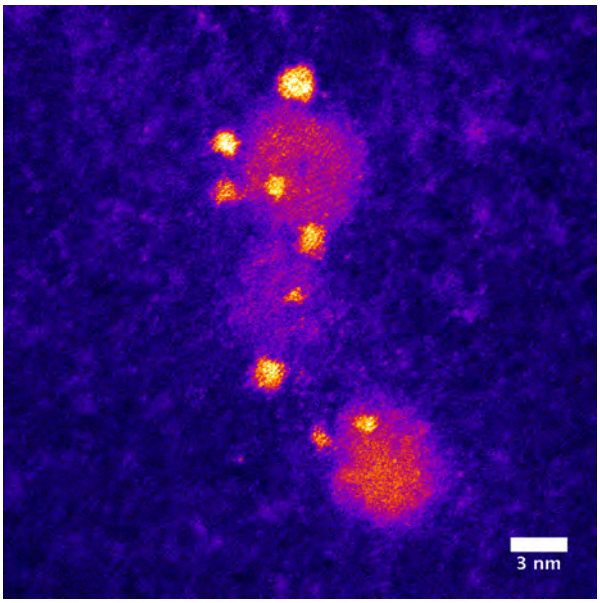

(d) 3 ferritin cores surrounded by gold clusters

Figure 4.13: Size-selected Au_{55} clusters deposited onto an amorphous carbon substrate along with ferritin in a buffer solution. It can be seen that the two samples interact with each other on the grid. Gold clusters, which are brighter are found to surround the less dense ferritin cores. Single atoms of gold are also visible lying on the carbon substrate, these would make quantitative measurements challenging as it would be difficult to find a 'clear' area of background carbon to use as a normalisation.

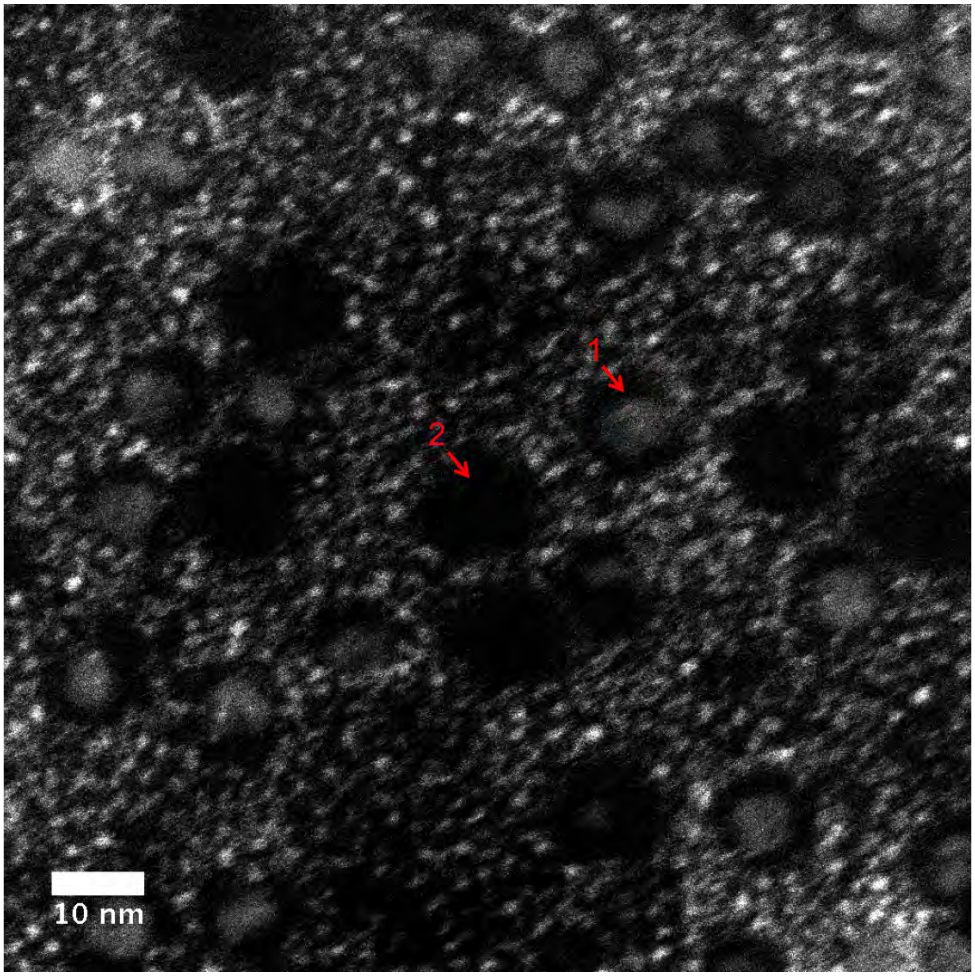

Figure 4.14: Gold particles surround ferritin molecules acting as a negative stain. It can be seen that there are some cores visible (labelled 1) and some 'empty' holes visible (labelled 2). These are most likely to be 'empty' ferritin proteins with no iron loading.

Size-Selected Au_{147} as the Mass Balance

A HAADF-STEM image of the Au_{147} clusters deposited onto a carbon substrate can be seen in Figure 4.15(a). The integrated intensity of 573 clusters was measured as described in chapter three and the resulting distribution is presented in Figure 4.15(b). It can be seen that the main peak in intensity is centred around 1.5 intensity units, but there is a second, much smaller peak at around 3.5 intensity units which represents doubly charged clusters traversing through the time of flight filter, see the discussion in chapter 3 for more detail. These clusters have twice the number of atoms and can be seen in Figure 4.15(a) as the two 'brighter' clusters in the top right corner.

The integrated intensity of 82 ferritin proteins deposited onto the same grid as the gold in Figure 4.15(a) was measured and was plotted in a histogram. Figure 4.16 shows this histogram and a representative HAADF-STEM image of the ferritin. It can be seen that there is a large variation in intensity as expected, but that also the histogram shows a multi peak formation. This histogram shape can be replicated with all ferritin sample sets.

As described in chapter 3, the scattering calibration (equation 4.2) can be used to convert from intensity to mass, effectively counting the atoms in each ferritin core. Table 4.1 shows the values obtained by applying the calibration to this data.

$$\frac{I_{Au}}{I_{Fe}} = \frac{N_{Au}}{N_{Fe}}\left(\frac{Z_{Au}}{Z_{Fe}}\right)^{n} \tag{4.2}$$

	Mean	Minimum	Maximum
Fe	6684 ± 1802	2199 ± 44	10478 ± 210

Table 4.1: Counting the iron atoms in ferritin molecules using Au_{147} size selected clusters as mass standards

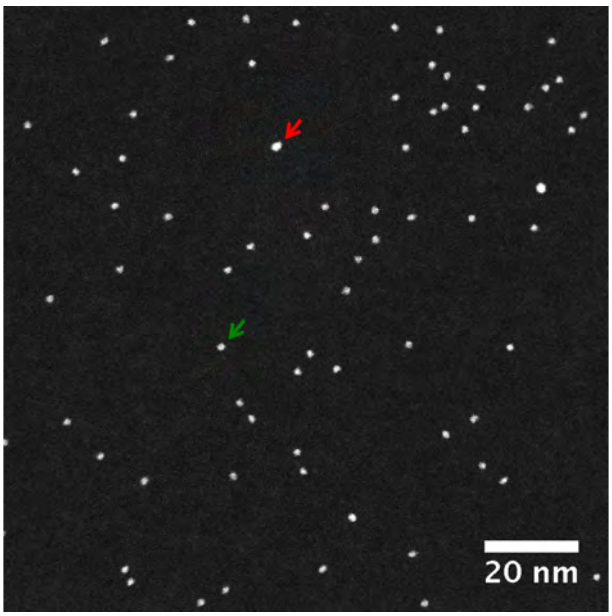

(a) HAADF-STEM image of size-selected clusters.

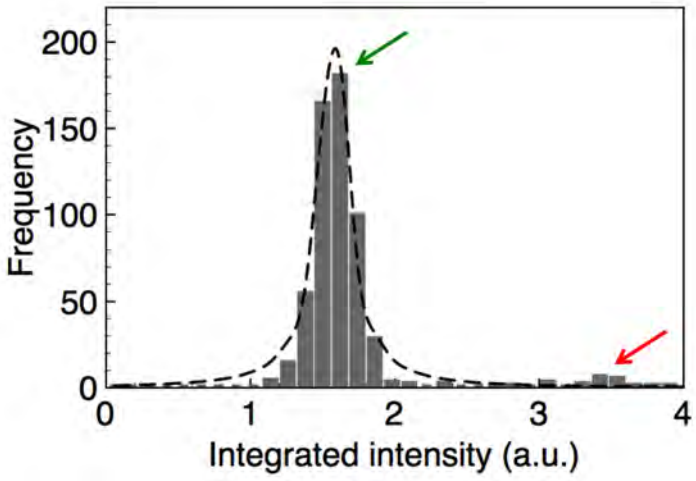

(b) Integrated intensity distribution of the clusters.

Figure 4.15: HAADF-STEM imaging of size-selected Au_{147} clusters deposited onto an amorphous carbon substrate. In 4.15(a) it can be seen that there are two sizes of clusters. The smaller size, highlighted with a green arrow, are much more abundant and are uniform in intensity, these are the Au_{147} clusters. There are two instances of the larger size cluster (red arrow) in this image, these are doubly charged clusters that have traversed through the mass filter. This is reflected in the histogram of integrated intensities shown in 4.15(b), where there is large peak representing the Au_{147} clusters and a much smaller peak at twice the intensity.

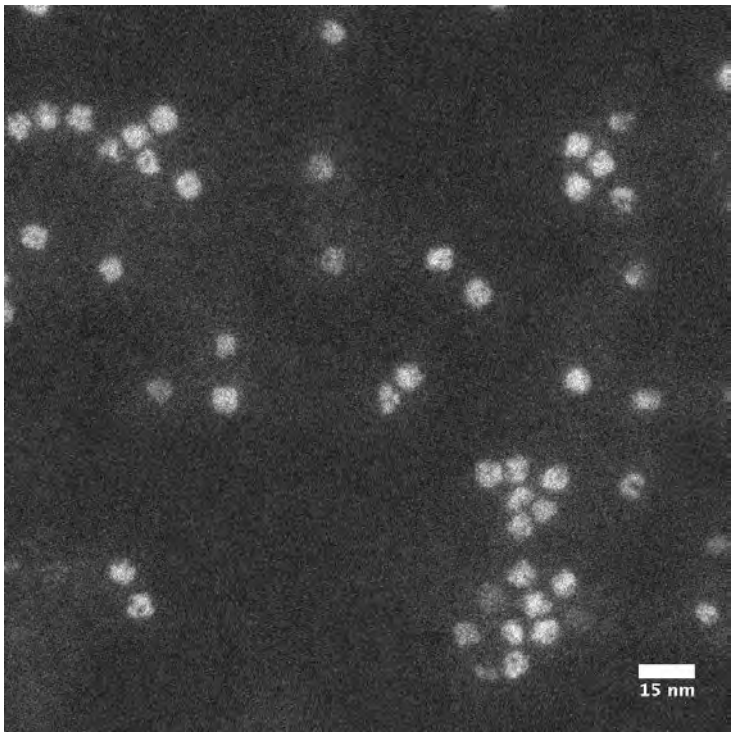

(a) HAADF-STEM image of ferritin

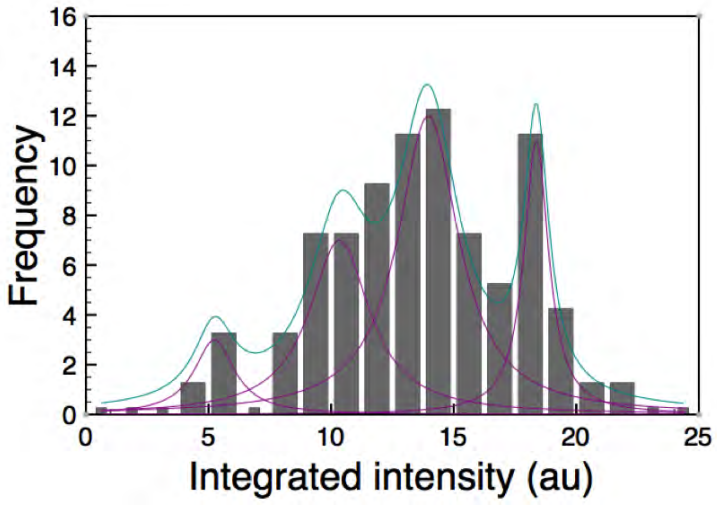

(b) Integrated intensity distribution of ferritin

Figure 4.16: Ferritin molecules adsorbed onto a carbon substrate were imaged using HAADF-STEM (4.16(a)). The integrated intensities of each protein core was then measured and plotted in a histogram (4.16(b)). A multiple peak distribution can be seen, with a gaussian fitted to each peak. This suggests that the ferritin protein has preferential loading states.

	Mean	Minimum	Maximum
Fe	2607 ± 651	1531 ± 31	4026 ± 81

Table 4.2: Counting the iron atoms in ferritin molecules using Au_{55} as mass standards. This can be compared to that found using Au_{147} clusters as mass standards, in table 4.1

Size-Selected Au_{55} as the Mass Balance

The experiment was repeated but using smaller size-selected clusters with 55 atoms. Figure 4.17 shows a HAADF image of the Au_{55} clusters and their associated integrated intensity distribution (inset) and the integrated intensity of the ferritin clusters. Both the distributions show the same broad shape as those for the larger Au_{147} clusters. However, when the calibration is made for the iron content (Table 4.2) the values are around 60% smaller, suggesting that these clusters are too small in comparison with the ferritin core to be suitable mass standards.

Multi Peak Analysis

As discussed earlier, Figure 4.16(b) shows a distribution with multiple peaks rather than a simple gaussian shape. This suggests that there are preferential binding states within the molecule leading to peaks at certain loading amounts, which is supported by the sub-unit morphology visible in the HAADF-STEM images. The multiple peak formation is always seen when analysing integrated intensities and so is reproducible, indicating it is a true property of assemblies of ferritin and implying that there are preferential loading states in the molecules.

In order to understand this distribution an approximate gaussian distribution was fitted to each peak in the distribution and the separation was forced to be equal (shown in Figure 4.18). It can be seen that this is a reasonably good fit to the data. This multi-peak structure was not seen by [14] and rather a simple gaussian distribution was observed.

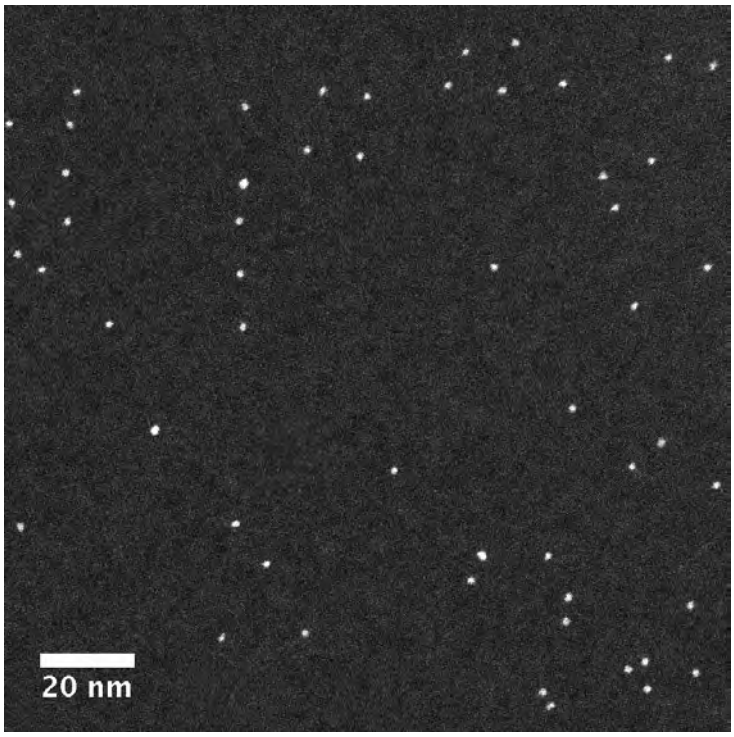

(a) HAADF-STEM image of size selected Au_{55} clusters

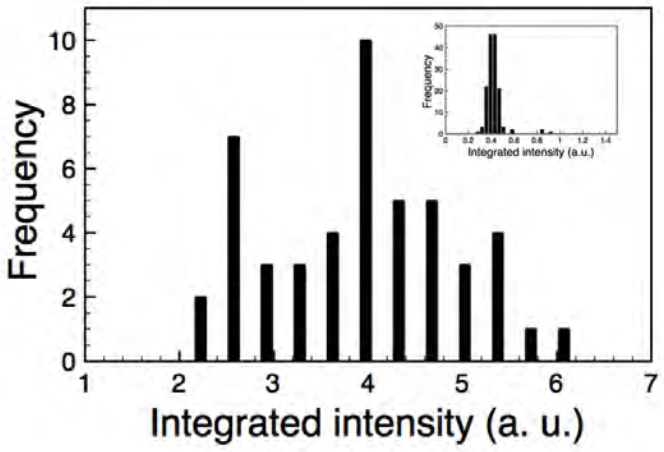

(b) Integrated intensity distribution of size selected Au_{55} clusters

Figure 4.17: Size-selected Au_{55} clusters deposited onto an amorphous carbon substrate were imaged using HAADF-STEM. A uniform intensity distribution of Au_{55} can be seen in the inset. As with the Au_{147} clusters, there are doubly charged clusters visible in the image and second peak in the histogram. Histogram of the integrated intensity of ferritin deposited onto the same grid as Au_{55} clusters. A similar multiple peak structure is found to that found previously.

	Mean	Minimum	Maximum
Fe	6684 ± 1802	2199 ± 44	10478 ± 210
Ferrihydrite	4626 ± 1247	1522 ± 30	7252 ± 145

Table 4.3: Iron and Ferrihydrite correction using Au_{147} as the mass standard

Correcting for Ferrihydrite

As discussed in section 4.2, the iron core within the protein is not pure iron but in fact an iron oxide core and this must be considered when performing quantification. This can be corrected by taking into account the other elements by calculating the 'equivalence' factor [20] using Equation 4.3.

$$\frac{1}{E} = N_{Fe}(\frac{Z_{Fe}}{Z_{Fe}})^n + N_O(\frac{Z_O}{Z_{Fe}})^n + N_H(\frac{Z_H}{Z_{Fe}})^n \tag{4.3}$$

The Au_{147} data taking into account the oxide nature of the core is shown in table 4.3. It can be seen that once the intensity contribution due to the other elements such as oxygen and hydrogen has been taken into account, the total number of iron atoms significantly decreases. The maximum loading often quoted for ferritin is 4500 iron atoms so with this in mind, the values in table 4.3 seem too high. This is due to the extra contribution from the protein shell, which is discussed below.

Estimation of the Protein Contribution

Discussion up to now has only taken into account the ferritin core however it is also necessary to take into account the protein shell surrounding the core. Previous electron microscopy studies do not take this into account, or include it in their background subtraction. However, the protein shell must still be present in some way, even if it is damaged by entry into the vacuum, dehydration upon drying or interaction with the electron beam.

In section 4.4.1 it is noted that a protein layer can be seen in line profiles of ferritin cores, and is suggested by the fact that cores never seem to touch each other on the grid but are separated by a

small gap, which could be assumed to be protein. This protein layer can also be seen on higher magnification images and when gold is combined with ferritin on the same grid, presented in section 4.4.2. There are two methods to estimate the protein contribution numerically, through calculating the molecular weight of the protein and analysing the physical data.

The amino acid composition of the apoferritin shell is given in Harrison *et al.* [22], from this, the number of each essential element (C, H, O, N, S) can be deduced (Table 4.4). The equivalent intensity of these elements was estimated and subtracted from the actual intensity of the measured cores and around a third of the values were converted to negative numbers. This method is therefore an overestimation of the protein shell contribution, and indicates that the protein shell is, at least in part, damaged during preparation, entry into the microscope column vacuum or imaging.

An alternative method to work out the protein contribution is to exploit the multi-peak nature of the histogram to calculate each sub-unit intensity and then subtract the appropriate numbers of subunits from the 'brightest' ferritin core. In principle, this would result in the protein intensity only.

In figure 4.18 it can be seen that the peak interval was fixed to the mean interval of the peaks shown in figure 4.16. Assuming the maximum intensity value corresponds to the protein plus four intervals (one for each subunit), the protein contribution can be calculated and subtracted from each ferritin molecules intensity to obtain the core intensity. This resulted in the protein contribution estimation being 30% of the total intensity, implying the beam obliterates the majority of the light protein shell.

The contribution of the protein was therefore taken into account and the final values for the number of iron atoms per ferritin core using size-selected Au_{147} clusters as the mass balance was 3259 with a standard deviation of 1247. This is consistent with the maximum loading often

Amino Acid	Residues per molecule	Chemical Formula	Total Formula
Glutamic acid	577	$C_5H_9NO_4$	$C_{2885}H_{5193}N_{577}O_{2308}$
Aspartic acid	435	$C_4H_7NO_4$	$C_{1740}H_{3045}N_{435}O_{1740}$
Lysine	195	$C_6H_{14}N_2O_2$	$C_{1170}H_{2730}N_{390}O_{390}$
Arginine	213	$C_6H_{14}N_4O_2$	$C_{1278}H_{2982}N_{852}O_{426}$
Histidine	129	$C_6H_9N_3O_2$	$C_{708}H_{1062}N_{354}O_{236}$
Tyrosine	134	$C_9H_{11}NO_3$	$C_{1206}H_{1474}N_{134}O_{402}$
Phenylalanine	175	$C_9H_{11}NO_2$	$C_{1575}H_{1925}N_{175}O_{350}$
Tryptophan	21	$C_{11}H_{12}N_2O_2$	$C_{231}H_{252}N_{42}O_{42}$
Leucine	620	$C_6H_{13}NO_2$	$C_{3420}H_{7410}N_{570}O_{1140}$
Isoleucine	92	$C_6H_{13}NO_2$	$C_{468}H_{1014}N_{78}O_{156}$
Valine	173	$C_5H_{11}NO_2$	$C_{865}H_{1903}N_{173}O_{346}$
Alanine	348	$C_3H_7NO_2$	$C_{1044}H_{2436}N_{348}O_{696}$
Glycine	250	$C_2H_5NO_2$	$C_{500}H_{1250}N_{250}O_{500}$
Serine	180	$C_3H_7NO_3$	$C_{636}H_{1484}N_{212}O_{636}$
Threonine	140	$C_4H_9NO_3$	$C_{560}H_{1260}N_{140}O_{420}$
Proline	56	$C_5H_9NO_2$	$C_{360}H_{648}N_{72}O_{144}$
Cysteine	48	$C_3H_7NO_2S$	$C_{144}H_{336}N_{48}O_{96}S_{48}$
Methionine	74	$C_5H_{11}NO_2S$	$C_{335}H_{737}N_{67}O_{134}S_{67}$
Ammonia	453	NH_3	$N_{453}H_{1359}$
TOTAL			$C_{19125}H_{38500}N_{5370}O_{10162}S_{115}$

Table 4.4: Amino acid composition of apo-ferritin and associated chemical formulas, table modified from [22]

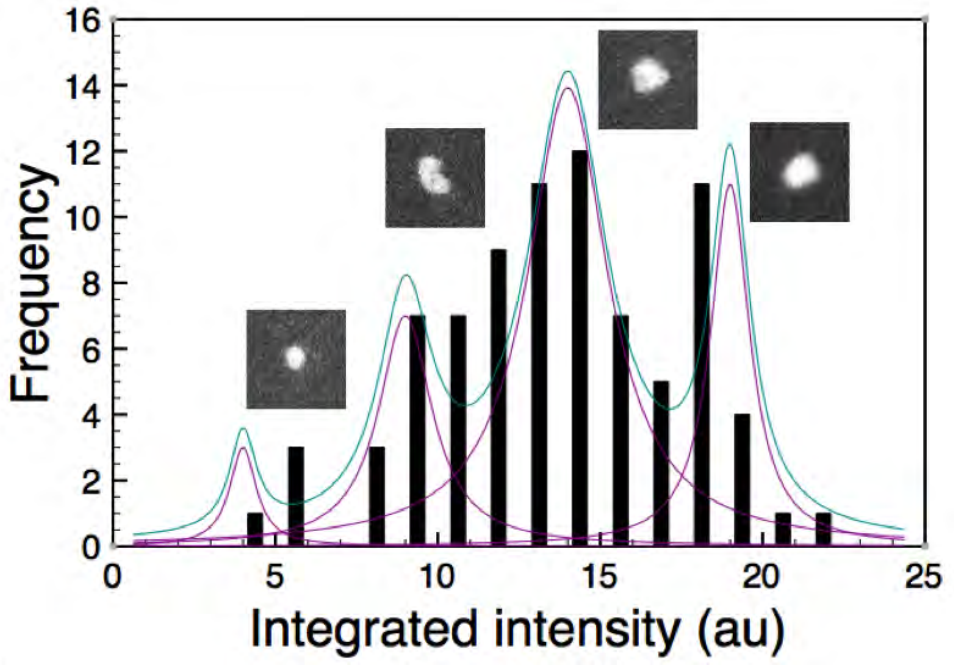

Figure 4.18: Calculating the protein contribution from separation of peaks. The peak interval was fixed, in order to estimate the protein contribution. Insets show HAADF-STEM images (20nm x 20nm) of representative ferritin cores for each peak in intensity

quoted as 4,500 iron atoms per protein. The minimum loading was found to be 154 ± 3 and the maximum was 5885 ± 118. It is important to bear in mind that the proteins with very low iron loadings would not be included in analysis, as discussed in section 4.4.2 and so this minimum could be artificially high. The maximum is over the 4,500 maximum loading often quoted in the literature. This is assumed to be because the oxide stoichiometry is assumed to be exactly the same across the whole population. It is noted that when Walls *et. al.* [18] synthesised magnetite nanoparticles within recombinant ferritin, a maximum of 8,500 iron atoms within a single ferritin protein was found. Although this was attributed to the synthesised nature of the particles, it indicates that ferritin is physically capable of holding more than 4,500 iron atoms.

The protein shell is almost certainly modified by the experimental procedure, either at the sample preparation stage, during introduction to the microscope column or interaction with the electron beam. The value calculated is an estimation based on the analysis of the range of core

intensities.

4.4.3 Reduction of the Iron Core

As discussed earlier, the iron at the centre of the protein core is stored as an iron oxide in the 3+ oxidation state. The oxidation takes place on entry into the protein, and if the iron is exposed to a reduction agent the iron should escape from the protein and the iron core reduce. Experimentally this has been achieved following the protocol in [23] and the resulting images can be seen in Figure 4.19.

In order to assess the changes in the cores accurately, the half grid method was used again. This time the standard used was 'native' ferritin from the original sample. This allowed a comparison to be made with minimal changes in imaging conditions. Figure 4.20 shows the integrated intensity distribution after 6 minutes reduction along with a control distribution on the same grid. Two major comparisons can be made: it can be seen that the average intensity has shifted lower and that there are fewer peaks visible in the reduced distribution.

As before, there is a wide range in the integrated intensity distribution with multiple peaks in both the control and reduced samples. In Figure 4.20(a) 4 peaks can be fitted to the distribution with a separation fixed at 1 unit. These can be attributed to preferential binding sites as with Section 4.4.2. Comparing this to Figure 4.20(b), one sees only 3 peaks that can be fitted in the distribution. The distribution also seems more uneven, with higher peaks towards the lower end of the range. This could be due to two reasons: the amount of preferential binding sites has reduced or iron prefers to exit from the fuller cores rather than the less filled ones.

A slightly different trend can be seen in the reduction after 18 minutes (Figure 4.21). In this case there is a more pronounced change in the average intensity as a result of the longer reduction time, however the distribution becomes wider. This could be due to the longer time

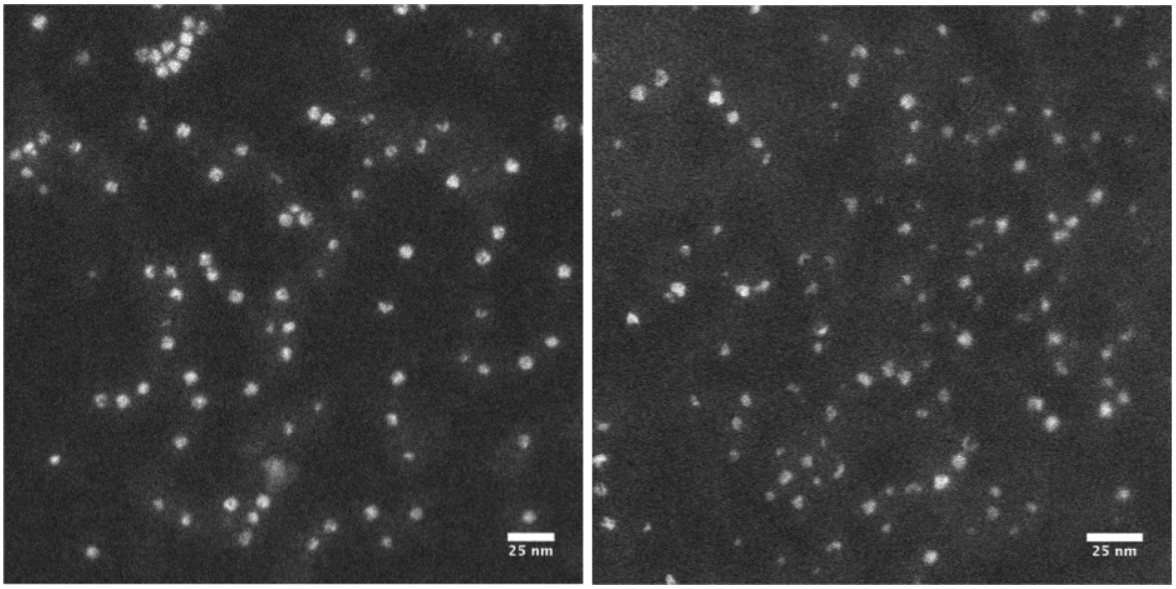

(a) Control (b) 5 mins

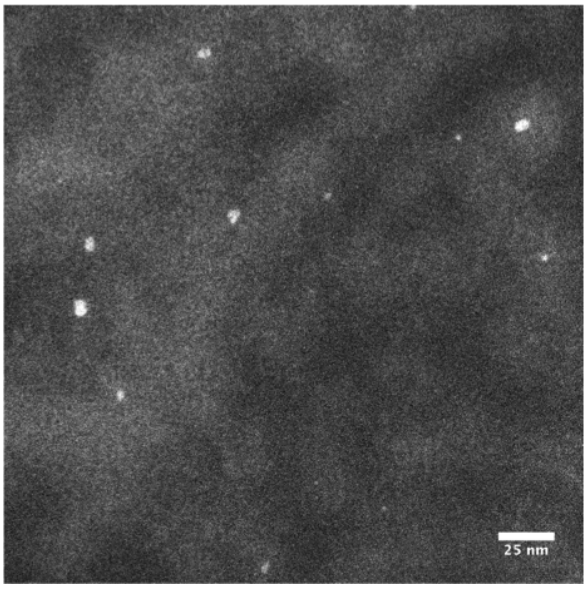

(c) 6 hours

Figure 4.19: Reduction of the iron within ferritin cores over time. In 4.19(a) a HAADF-STEM image of a control sample of ferritin is shown, and shows a similar range of iron loadings and core shapes as found previously. 5 minutes into the reduction, the cores are found to be less dense and after 6 hours, far fewer cores could be found.

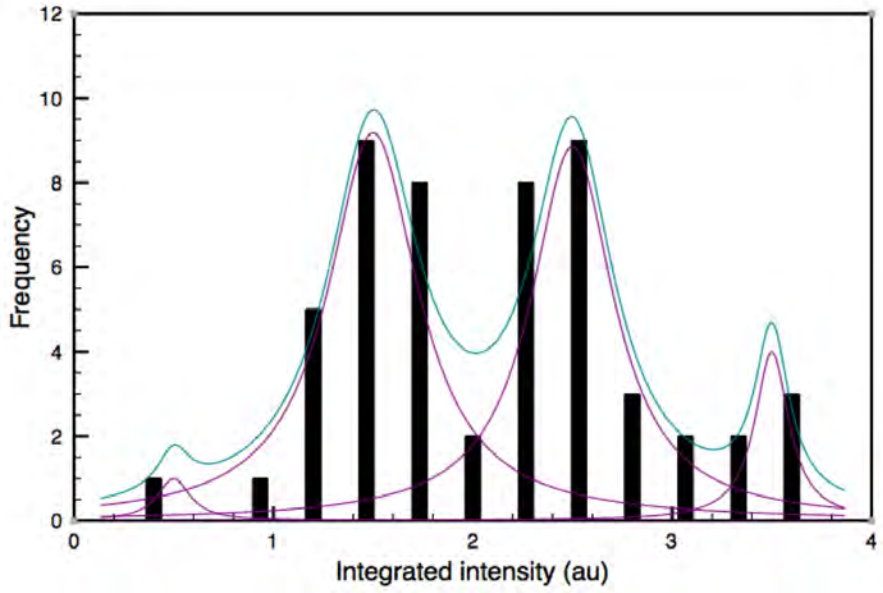

(a) Control

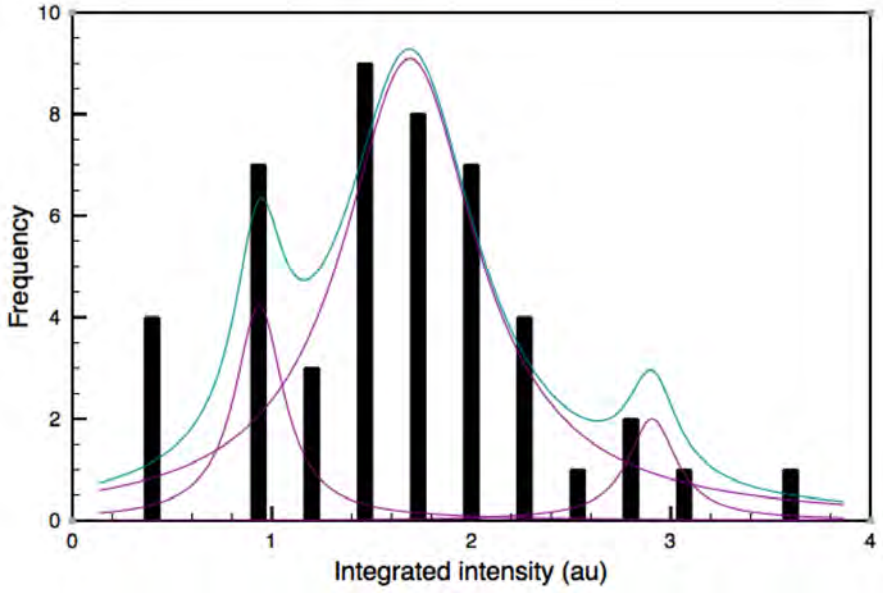

(b) Reduced after 6 minutes

Figure 4.20: Integrated intensity distribution of reduced ferritin cores. A shift in average intensity can be seen, along with a reduction of the number of peaks in the distribution.

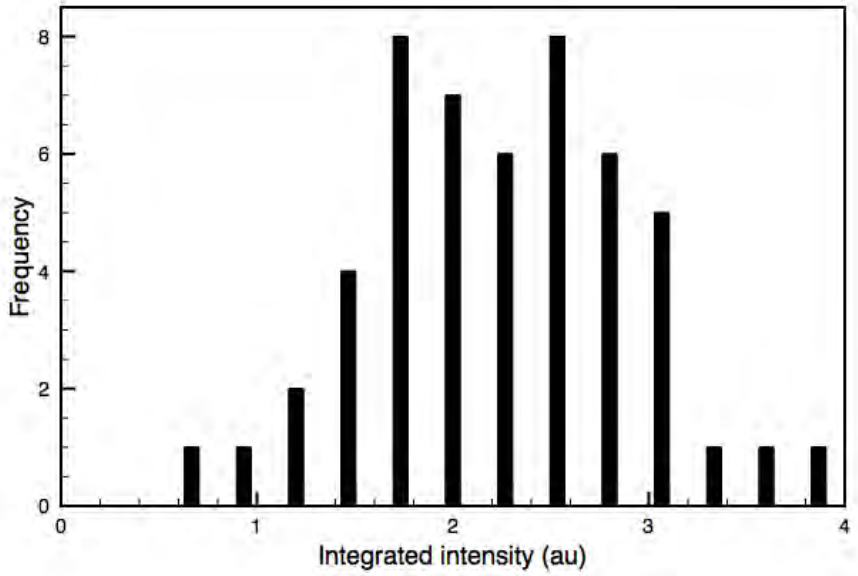

(a) Control

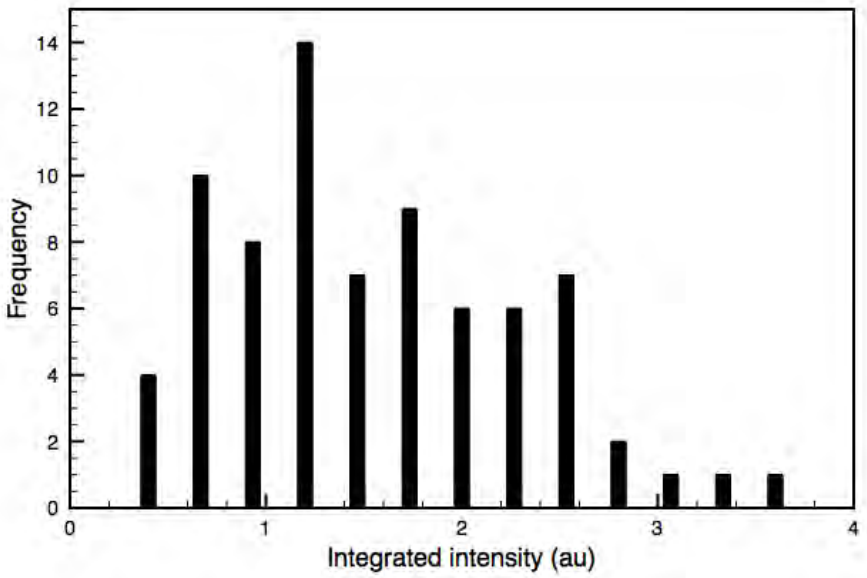

(b) Reduced after 18 minutes

Figure 4.21: Integrated intensity distribution of reduced ferritin cores. A pronounced shift in average intensity can be seen and a more even distribution of peaks appears after 18 minutes.

period allowing a more even removal of iron across all the binding sites resulting in a shift of distribution rather than higher peaks at the lower end.

4.5 Conclusions and Future Work

The high metal content of ferritin makes it an excellent candidate for imaging with HAADF-STEM and aberration correction has enabled atomic precision imaging to be performed. This has resulted in low magnification images showing a range of iron loadings and core shapes. High magnification images show lattice structure consistent with those in the literature. The presence of the protein shell surrounding the core has also been quantified and found to contribute towards the HAADF-STEM intensity measured. It has also been demonstrated that the protein shell contracts when in close proximity to other proteins.

Calibration with size-selected clusters has resulted in the iron content of individual proteins to be determined, and for this to be matched to the shape in the HAADF-STEM image. A mean number of around 3,300 iron atoms per ferritin core was found, once the iron oxide nature of the core and protein shell had been taken into account. Although, the ferritin core was also found to have preferential loading states, indicated by higher instances of certain loadings.

This method could be applied to ferritin from different areas in the body, such as the heart or lung, where there are different iron demands, and therefore the structure of the iron core could vary. The mass-standard quantification procedure could also be clinically relevant. For example, some patients exhibit symptoms of iron deficiency but have normal total body iron levels. Perhaps the patients have a mutation in the ferritin protein which means their iron storage on an individual molecule level is not efficient and iron is not available as it should be.

The mass measurement technique could also be extended to other metal containing proteins, such as transferrin. The advantage of this technique over other mass measurements, is that the mass can be matched to shape, as demonstrated in this study.

Future work should also include ‘filling up’ of the ferritin protein with iron and then quantification of this using size-selected gold clusters as a mass standard. This could provide further

insight into the iron loading, particularly how the subunits grow over time. Chemical characterisation such as EELS or EDX could also be performed to try to ascertain more accurately the stoichiometry of the ferritin cores.

References

[1] L. Stryer. *Biochemistry*. W. H. Freeman and Company, 3 edition, 1988.

[2] B. Halliwell and J. M. Gutteridge. Oxygen toxicity, oxygen radicals, transition metals and disease. *Biochemical Journal*, 219(1):1, 1984.

[3] M. A. Knovich, J. A. Storey, L. G. Coffman, S. V. Torti, and F. M. Torti. Ferritin for the clinician. *Blood reviews*, 23(3):95–104, 2009.

[4] J. F. Collingwood, A. Mikhaylova, M. Davidson, C. Batich, W. J. Streit, J. Terry, and J. Dobson. In situ characterization and mapping of iron compounds in alzheimer's disease tissue. *Journal of Alzheimer's Disease*, 7(4):267–272, 2005.

[5] J. Collingwood and J. Dobson. Mapping and characterization of iron compounds in alzheimer's tissue. *Journal of Alzheimer's Disease*, 10(2):215–222, 2006.

[6] F. A. Fischback, P. M. Harrison, and T. G. Hoy. The structural relationship between ferritin protein and its mineral core. *Journal of molecular biology*, 39:235–238, 1969.

[7] A. Lewin, G. R. Moore, and N. E. Le Brun. Formation of protein-coated iron minerals. *Dalton transactions*, (22):3597–3610, 2005.

[8] W. Wang, M. A. Knovich, L. G. Coffman, F. M. Torti, and S. V. Torti. Serum ferritin: Past, present and future. *Biochimica et Biophysica Acta (BBA)-General Subjects*, 1800(8):760–769, 2010.

[9] O. Kakhlon, Y. Gruenbaum, and Z. L. Cabantchik. Repression of ferritin expression increases the labile iron pool, oxidative stress, and short-term growth of human erythroleukemia cells. *Blood*, 97(9):2863–2871, 2001.

[10] G. C. Ford, P. M. Harrison, D. W. Rice, J. M. A. Smith, A. Treffry, J. L. White, and J. Yariv. Ferritin: design and formation of an iron-storage molecule. *Philosophical Transactions of the Royal Society of London. B, Biological Sciences*, 304(1121):551–565, 1984.

[11] C. Wustefeld and R. R. Crichton. The amino acid sequence of human spleen apoferritin. *FEBS Letters*, 150(1):43–48, 1982.

[12] R. R. Crichton and J-P Declercq. X-ray structures of ferritins and related proteins. *Biochimica et Biophysica Acta (BBA)-General Subjects*, 1800(8):706–718, 2010.

[13] W. H. Massover. Ultrastructure of ferritin and apoferritin: a review. *Micron*, 24(4):389–437, 1993.

[14] Y. H. Pan, K. Sader, J. J. Powell, A. Bleloch, M. Gass, J. Trinick, A. Warley, A. Li, R. Brydson, and A. Brown. 3D morphology of the human hepatic ferritin mineral core: New evidence for a subunit structure revealed by single particle analysis of HAADF-STEM images. *Journal of structural biology*, 166(1):22–31, 2009.

[15] J. D. López-Castro, J. J. Delgado, J. A. Perez-Omil, N. Gálvez, R. Cuesta, R. K. Watt, and J. M. Domínguez-Vera. A new approach to the ferritin iron core growth: influence of the H/L ratio on the core shape. *Dalton Transactions*, 41(4):1320–1324, 2012.

[16] F. M. Michel, L. Ehm, S. M. Antao, P. L. Lee, P. J. Chupas, G. Liu, D. R. Strongin, M. A. A Schoonen, B. L. Phillips, and J. B. Parise. The structure of ferrihydrite, a nanocrystalline material. *Science*, 316(5832):1726–1729, 2007.

[17] C. Wang, Q. Qiao, T. Shokuhfar, and R. F. Klie. High-resolution electron microscopy and spectroscopy of ferritin in biocompatible graphene liquid cells and graphene sandwiches. *Advanced Materials*, 2014.

[18] M. G. Walls, C. Cao, K. Yu-Zhang, J. Li, R. Che, and Y. Pan. Identification of ferrous-ferric Fe3O4 nanoparticles in recombinant human ferritin cages. *Microscopy and Microanalysis*, 19(04):835–841, 2013.

[19] Q. Wang, C. P. Mercogliano, and J. Löwe. A ferritin-based label for cellular electron cryotomography. *Structure*, 19(2):147–154, 2011.

[20] Z. W. Wang, O. Toikkanen, F. Yin, Z. Y. Li, B. M. Quinn, and R. E. Palmer. Counting the atoms in supported, monolayer-protected gold clusters. *Journal of the American Chemical Society*, 132(9):2854–2855, 2010.

[21] D. Pearmain, S. J. Park, Z. W. Wang, A. Abdela, R. E. Palmer, and Z. Y. Li. Size and shape of industrial Pd catalyst particles using size-selected clusters as mass standards. *Applied Physics Letters*, 102(16):163103–163103, 2013.

[22] P. M. Harrison, T. Hofmann, and W. I. P. Mainwaring. The structure of apoferritin: amino acid composition and end-groups. *Journal of molecular biology*, 4(4):251–256, 1962.

[23] M. J. Donlin, R. F. Frey, C. Putnam, J. Proctor, and J. K. Bashkin. Analysis of iron in ferritin, the iron-storage protein: a general chemistry experiment. *Journal of chemical education*, 75(4):437, 1998.

Chapter 5

Scanning Transmission Electron Microscopy Characterisation of Iron Chelating Alginates

5.1 Introduction

It has been proposed that alginate, a naturally occurring polymer, could be used as an iron chelator therapy in colorectal cancer, where excess luminal iron has been linked with cancerogenesis. In this chapter a physical characterisation study of the structures formed from alginate incubated with iron is presented, using aberration corrected scanning transmission electron microscopy (STEM) and energy dispersive x-ray (EDX) to characterise the structures formed.

This research was performed in conjunction with collaborators in the Schools of Cancer Sciences (Richard Horniblow and Chris Tselepsis) and Chemistry (Zoe Pikramenou), who conceived the therapy and prepared all samples. All of the electron microscopy and subsequent image analysis presented in this chapter were conducted by the author.

The work presented in this chapter has contributed towards the following publication:

The importance of alginate in templating formation of iron-oxide nanoparticles. Richard D. Horniblow, Miriam R. Dowle, Tariq H. Iqbal, Richard E. Palmer, Zoe Pikramenou and Chris Tselepsis. *Submitted to ChemComm.*

5.2 Literature Review

5.2.1 Colorectal Cancer and the Link to Iron

Worldwide, colorectal cancer (commonly known as bowel cancer) is the third most common form of cancer in males and second in females[1]. The mortality rate is 50.7% of cases and it is the second biggest cause of cancer mortality in the UK [1]. It is a government priority to identify the causes and trends in colorectal cases and diagnosis, with an NHS screening programme being set up in 2006 [2].

Around 80% of people who develop bowel cancer have a mutation in the adenomatous polyposis coli (APC) gene [3]. This is a tumour suppressor gene and so mutant protein products from it are thought to be an inducer of the disease [4], [5]. Mice have been genetically pre-disposed to develop bowel cancer by inducing a mutant APC gene [3]. Varying amounts of iron were introduced to the mice and it was found that the more iron, the faster the tumourigenesis rate and slower the apoptosis rate. This concept is shown graphically in figure 5.1.

There are two types of iron present in the bowel, systemic and luminal. Systemic iron is that contained in the blood and cellular iron. Luminal iron is free iron associated with the inner surface (lumen) of the bowel. Epidemiological studies have found a link between high iron content in the diet and higher instances of bowel cancer, by comparing for example the typical diet in Africa with that in western countries [6, 7]. It has also been shown that with an increase of luminal iron, the likelihood of bowel cancer increases [3]. Luminal iron is extracellular iron residing on the inner surface of the bowel, this iron is not required nutritionally, and

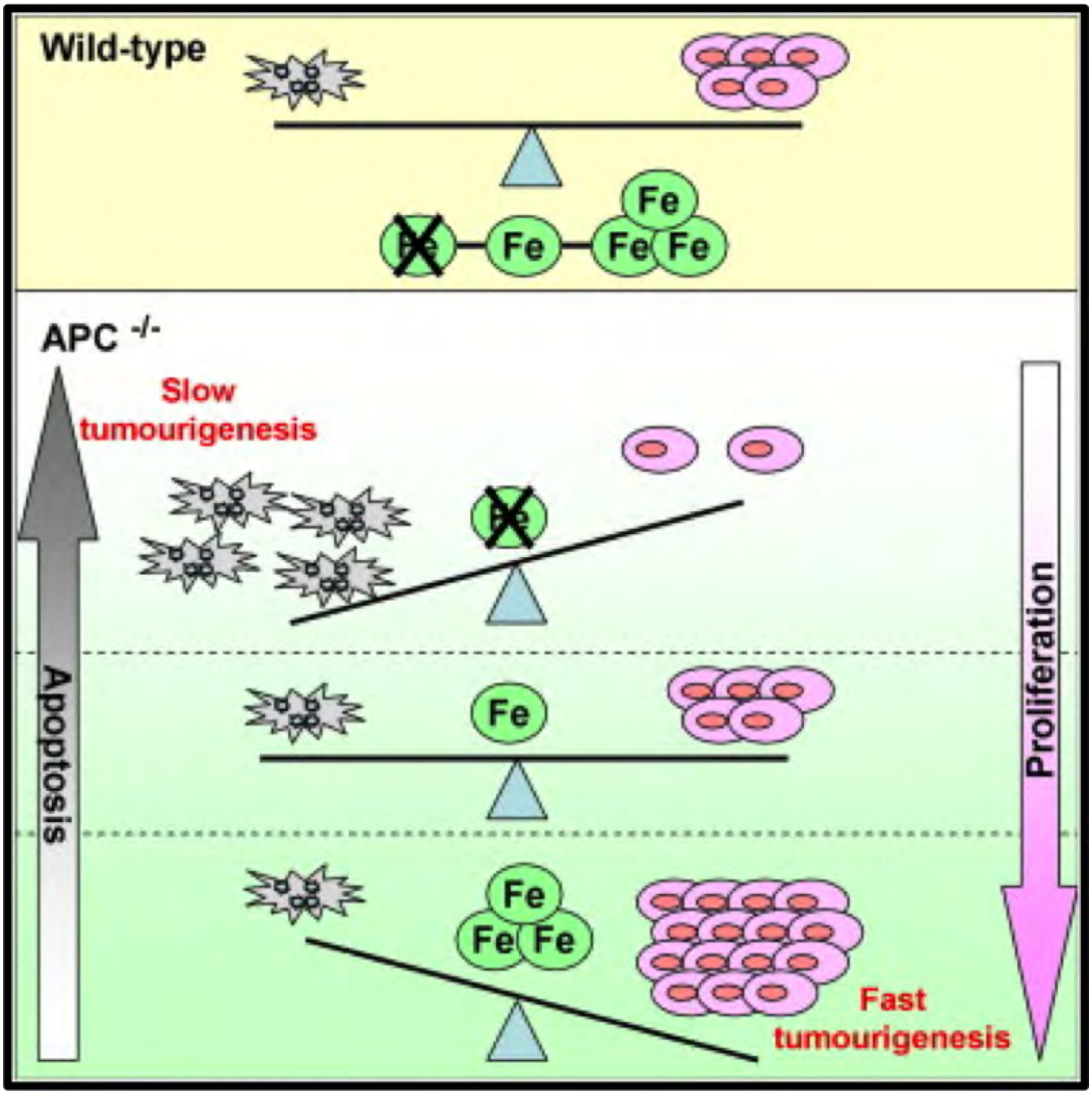

Figure 5.1: In mice pre-disposed to develop bowel cancer (by inroducing a mutant APC gene), an increase in iron concentration in the bowel results in a much higher risk of developing the cancer. As the iron concentration is increased, the tumourigenesis rate increases and apoptosis decreases. Figure reproduced from [3].

so is not absorbed in the small intestine (duodenum). As discussed in previous chapters, iron is essential for an array of biochemical processes within the body. And so, the specific reduction of luminal iron, rather than systemic iron (as described in Chapter 4), needs a targeted approach.

Therapeutic methods used against bowel cancer depend on the extent of the tumour. Smaller tumours are removed via surgery and larger are treated with conventional chemotherapy to attack tumour growth [8]. With a link between cancer and an excess of luminal iron now established, a new generation of therapies can be developed to reduce the luminal iron concentration. One promising proposal is the use of natural polymers called alginates as an iron chelation therapy.

5.2.2 Alginates and Iron Chelation

Alginates are naturally occurring polysaccharides found in seaweed. They electrostatically bind all divalent (+2) metal ions as they are negatively charged, the strongest bond being formed with strontium. Alginates in solution can be very viscous, hence their use as gelling agents in food. There are two sugar units that act as building blocks for alginate polysaccharides, mannuronic acid (M) and guluronic acid (G). Alginates are defined by their M/G ratio and their molecular weight, however the order of appearance of subunits within the chain is random [9]. All alginates exhibit broadly similar behaviours, such as gelling when solubilised. However, a difference in M/G ratio can influence the structures formed along with length of polymer [10] as the two subunits have differing binding affinities for different metals.

There is an enhanced binding capacity for group 2 metal ions as these are the right size to fit into the ‘egg-box’ shaped cavity. For example, when binding calcium the ‘egg box’ structure is formed with the calcium ions occupying gaps between different alginate strands [11]. A chemical representation of this egg-box structure is found in figure 5.3. This structure can be long range and reasonably robust. In a physiological environment such as the bowel, the two main metal ions present will be iron, as discussed, and calcium. The G subunits bind calcium

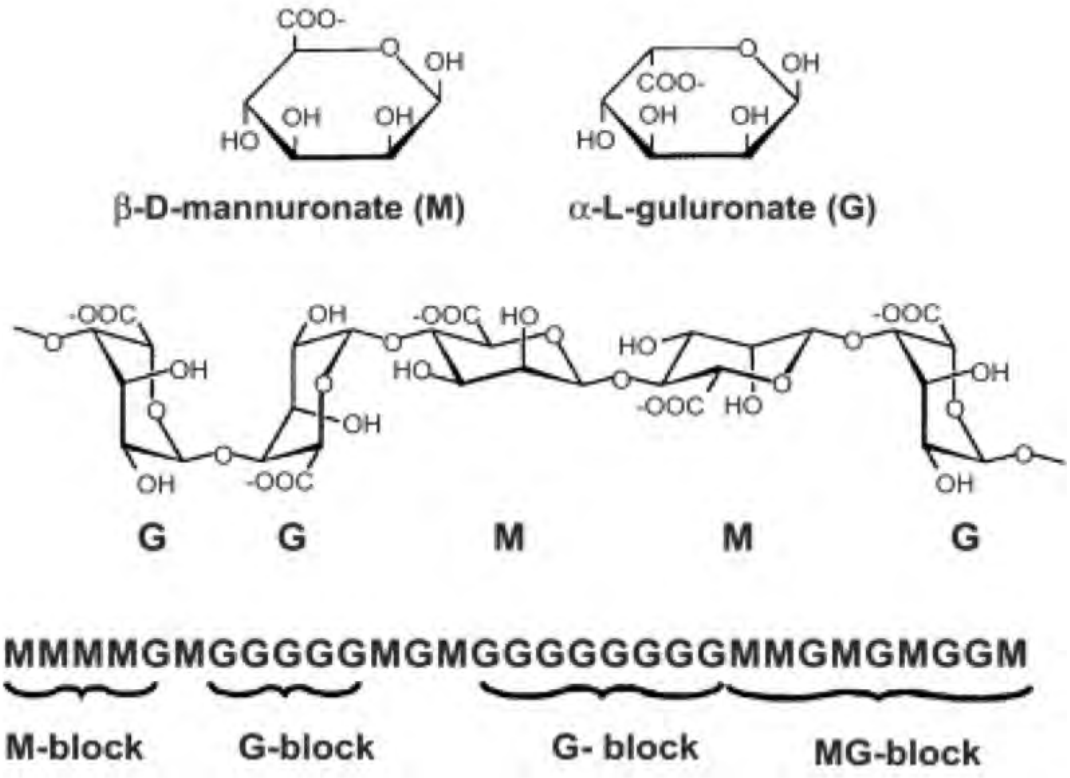

Figure 5.2: The chemical structure of alginates. There are two sugar units, M and G. These connect into long chains, where each combination of M and G makes a different alginate. The M/G ratio determines the properties of the alginate. Figure amended from [12].

stronger than the M subunits. This is not a chemical effect but rather a physical one, the size for the ion to fit into is better suited to calcium and so it more strongly bound. Iron is therefore bound more by alginates with a higher M number, as there are less calcium binding G subunits present in the polymer chain.

It has been found that when iron is added to alginates in a high pH environment (pH 13), nanoparticles are formed within the gel-like network [14]. These nanoparticles typically take on an Fe_2O_3 form and are 4 to 15nm in diameter. This work was performed using a combination of non-aberration corrected TEM and magnetic studies. Kroll *et al.* proposed to exploit the magnetic properties of the alginate/iron oxide gels to develop new diagnostic techniques such as drug delivery [14].

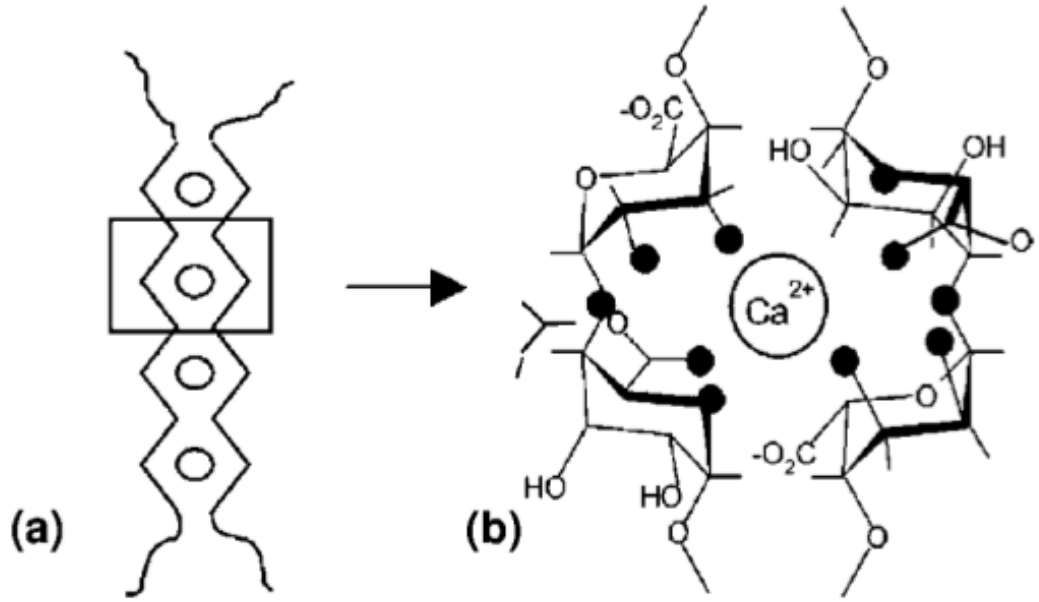

Figure 5.3: When the G subunits in an alginate chain bind calcium, they form what are known as 'egg box' structures, as can be seen in (a). Figure reproduced from [13].

Alginates as a Possible Cancer Therapy

Given the link between excess luminal iron and bowel cancer, it is proposed that the iron chelating behaviour of alginate molecules could be exploited as a bowel cancer therapy. The alginates can be ingested and since they are too long to be digested further up the digestive system they go straight to the bowel. Once in the bowel, any excess iron will be bound by the alginate and excreted. This drug therapy concept has been patented by our collaborators (Chris Tselepsis et al. Cancer Sciences, University of Birmingham) in the UK (patent number EP 2493481 A1). In theory, this would have several advantages in comparison to the conventional therapies:

- Alginates are non-absorbable and so will head straight to the bowel where they can collate any excess iron
- As alginates are cheap to produce, the therapy itself would be cheaper than more common therapies, both to manufacture and to administer

- Less invasive and therefore less traumatic for patients
- Alginates are already licensed for use in food products which will mean clinical trials can be 'fast-tracked'

In order to successfully develop a therapy the mechanism of iron chelation needs to be understood. It is also possible that a variety of different structures are formed when iron binds to alginates, this needs to be evaluated in a physiological context. As a first step a physiological environment was mimicked by using a simple dialysis set up with alginate and iron in solution in non-adjusted pH conditions. Although basic, this resembles conditions in the bowel with chemical reactions taking place and nanostructures being formed. Along with other physical characterisation techniques such as circular dichroism (CD) and fluorescent microscopy, scanning transmission electron microscopy (STEM) has been used to gain high resolution insight into these structures. The results from the STEM imaging and EDX are presented in this chapter.

5.2.3 Iron Oxide Nanoparticles

Biological Applications

Iron oxide nanoparticles have been widely studied in the context of biomedicine as imaging contrast and drug delivery agents. This is mainly due to their magnetic properties which can be exploited for magnetic imaging or manipulation [15]. Their use as delivery agents for drugs [16], contrast agents in MRI imaging [17] and targeted hypothermia treatment [18] have all been suggested, and in some cases are now available in the clinic.

As discussed in the previous chapter, iron has a suitably high atomic number for imaging with the electron microscope. This has been exploited in many studies, not only to analyse the nanoparticle structure itself but also to localise particles or groups of particles within cell sections.

Lu *et. al.* [19] have presented a method to coat iron oxide nanoparticles with a uniform silica coating with a view to modifying the surface properties whilst still being able to direct and detect the iron oxide core. This has similarities to the work presented in this chapter, however here the particles form spontaneously within a gel rather than being 'forced' to form with a gel coating. Li *et. al.* have presented what they have termed 'nanoroses' [20], which combine several properties within one particle. These include use as an MRI contrast agent, thermal activity, fluorescence and aptamers on the surface for targeted delivery of drugs and subsequent release.

5.2.4 TEM Imaging of Polymers and Nanoparticles

Alginates are basically natural (biological) polymers. Transmission electron microscopy (TEM) has been used extensively by polymer scientists to investigate their samples. However, they often use invasive techniques such as staining and sectioning to obtain sufficient contrast in the images. One example where stains are not used is in [14], where TEM is used to visualise the nano-structures formed within alginate networks at a reasonably high resolution. Particle sizing can be performed from the images, and oxide identification from the electron diffraction pattern.

Sipos *et. al.* have studied the interaction of polysaccharides with iron, resulting in iron oxide nanoparticle formation [21]. Relatively mono-disperse nanoparticles are found using TEM, with diameters between 5 and 10 nm. The TEM samples are made by dissolving a few flakes of the polysaccharide in water and then depositing this onto a formvar coated copper grid. The nanoparticles can then be seen suspended within a biological matrix and it is proposed that the particles are supported by this chitosan matrix rather than it incorporating within the particle. This is supported by other physical characterisation techniques such as DLS (dynamic light spectroscopy).

HAADF-STEM has been suggested as a useful technique for imaging polymers due to the nature of the signal and ease of interpretation of the images [22]. Although the average atomic

number of polymers is low, density does contribute towards contrast, particularly between different polymers [23]. Nevertheless, the imaging process is still more difficult than with higher atomic number samples.

Aberration corrected STEM, in both HAADF and BF modes, has the benefit of allowing one to conduct size and density calculations as with TEM but also achieve atomic resolution images to understand the stoichiometry of individual particles. Other techniques such as DLS, UV-vis spectrometry and viscometry or rheology can complement the direct imaging provided by EM. The advantage of these techniques is that they can be performed on the sample in the liquid phase and on large volumes to get an idea of general characteristics. These add another dimension to the analysis possible from electron microscopy images.

5.2.5 Supporting Experimental Results

The following experiments were carried out by collaborators Richard Horniblow, Chris Tselepsis and Zoe Pikramenou also from the University of Birmingham and based in the Cancer Sciences and Chemistry departments.

Circular dichroism is a technique that can determine the chirality of a molecule. This is done by exposing the molecule to differently polarized light and analysing the resulting signal. It has been used to examine the spectroscopic properties of iron and alginate mixtures in solution, where in this case iron binding will change the chirality inherent in alginate molecules. In the spectrum there is an FeOH peak at around 280nm which provides evidence for the possibility of iron oxide bond formation (see Figure 5.4). The peak at 210nm is dramatically decreased with the addition of iron, which is indicative of metal binding along the backbone of the alginate polymer.

These experiments indicated the presence of iron oxide bonds possibly in the form of nanoparti-

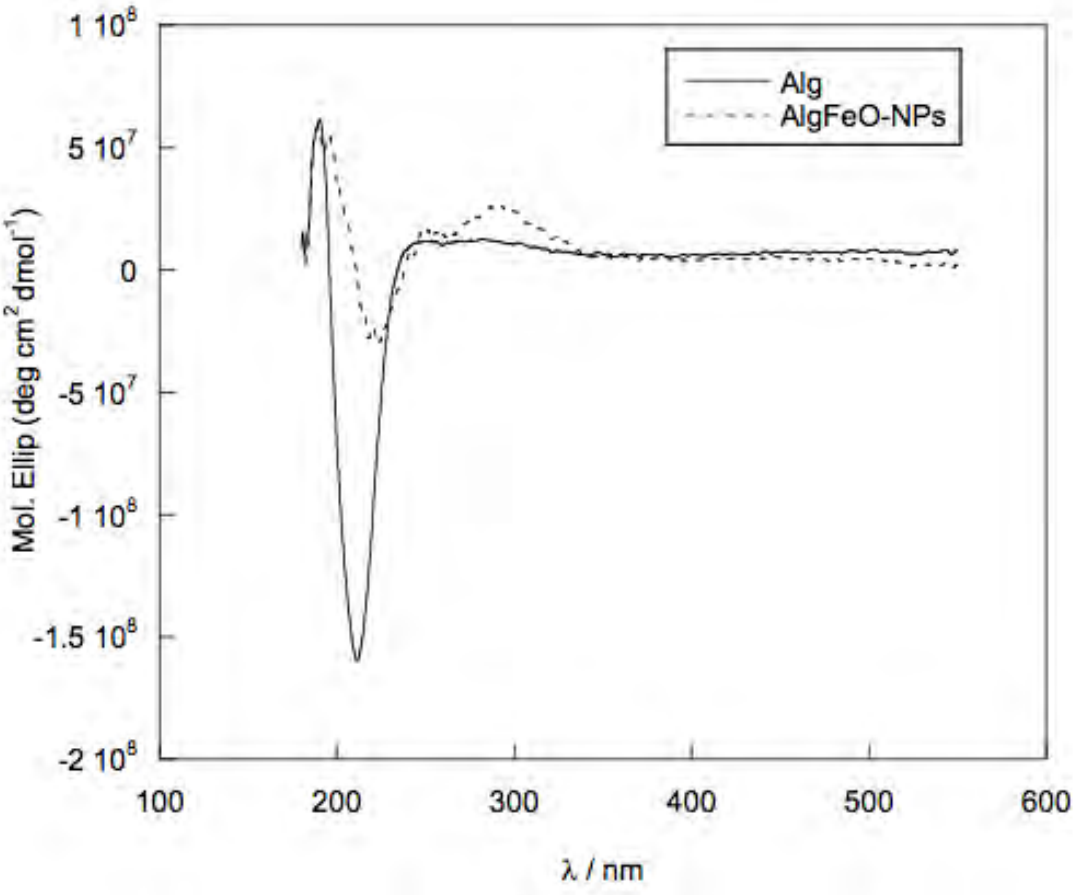

Figure 5.4: This circular dichroism spectra exhibits an peak at 280nm when iron is mixed with alginate, indicating iron hydroxide bonds are formed. The quenching of the peak at 210nm is due to iron binding along the backbone. Please note this work was carried out by RH.

cles, but did not directly detect any such particles. Electron microscopy, particularly aberration corrected STEM, is capable of imaging such particles and the resulting study forms the results presented in this chapter.

5.3 Aims

To develop a reliable protocol for preparing alginate/iron samples from solution onto a TEM grid in order to image them using the scanning transmission electron microscope.

To verify that iron nanoparticles are formed and ascertain the types of structures formed when alginate is incubated with iron *under physiological conditions*. This was aimed to be performed at the highest resolution possible by utilising electron microscopy, including aberration corrected HAADF, BF and EDX STEM. To characterise the oxide nature of the nanoparticles formed using electron diffraction patterns and crystallography.

5.4 Results and Discussion

5.4.1 Preliminary Protocol Development

Electron Microscopy Sample Preparation

As alginate/iron samples are a viscous liquid, it was initially unclear how to prepare the samples effectively for STEM analysis. Several different methods were tested and judged based on reliability of imaging at high resolution and level of carbon contamination:

1. Drop casting a small amount (5μl) of sample onto a TEM grid then leaving to dry in air
2. Drop casting a larger amount (20μl) of sample onto a TEM grid and wicking off after allowing to adsorb
3. Overloading TEM grid with sample (50μl) and collecting excess underneath, thus effectively pulling the sample through the grid

Figure 5.5 shows a schematic of each protocol. Protocol 1 was unsuccessful as the drying process over time resulted in large areas of crystallisation on the grid which were impossible to

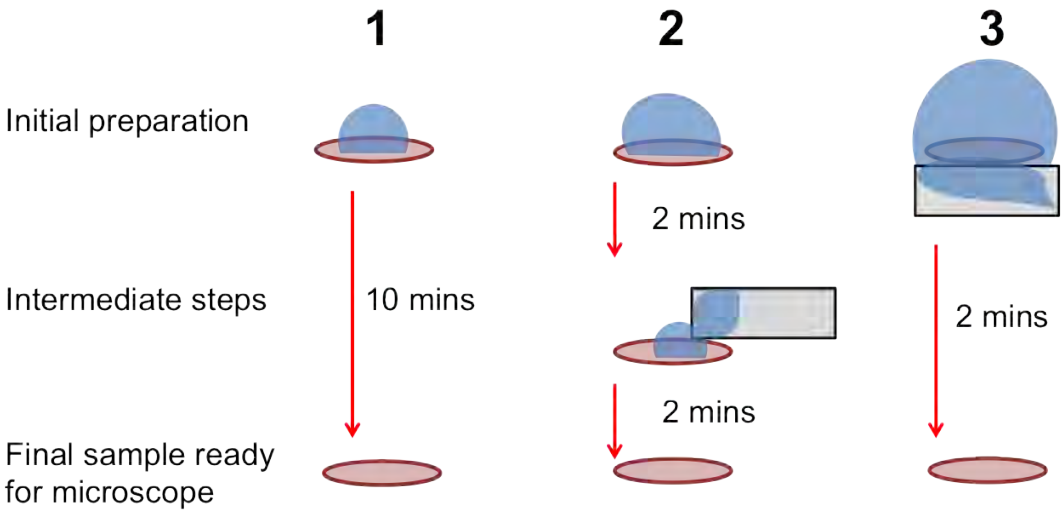

Figure 5.5: Schematic of the three sample preparation protocols tested. Protocol one resulted in extensive crystallisation of the sample on the TEM grid, and protocol two did not leave enough sample on the grid. Protocol three was therefore chosen as there was little sample crystallisation but an adequate layer of sample left on the grid for imaging.

image properly, even at low magnification. This could often be seen by the eye, meaning it was far too large for inspection with a transmission electron microscope. The second protocol avoided the drying process and so there were few areas of large scale crystallisation. However, because most of the sample had been blotted away, it was very difficult to find any areas where there was coverage and instead the grid was largely 'blank'.

Protocol 3 proved to be the most successful in that there was no drying process, and instead the sample had more contact with the grid by being effectively pulled through to the other side. This meant there were many areas with a thin sample coverage i.e. good imaging conditions for STEM. The carbon contamination was minimal and after a beam shower the sample could normally be imaged for at least an hour. This was therefore used to prepare all the samples used in the remainder of this results section.

Imaging Protocol

The imaging protocol was slightly different to that used for Chapter 4, in that bright field (BF) mode was used alongside the HAADF signal in order to focus and align properly. This is due to the different sensitivity of BF and HAADF STEM, with BF more sensitive to low atomic number materials than HAADF which is better for higher atomic numbers. Since the sample being investigated was organic (i.e. low atomic number) with iron embedded into it, a combination of HAADF and BF was necessary. See figure 5.6 for an example of the complementary signals provided by HAADF and BF at different magnifications taken from an alginate sample on an amorphous carbon support. It can be seen that in figure 5.6(d) the atomic structure of both the particles and carbon background is much clearer in the BF image, enabling easier focusing and image refinement using the BF signal.

To achieve stable scanning conditions it was also necessary to leave the sample to settle in the microscope for at least half an hour both on entry to the column and after a beam shower. This ensures negligible drift, both physically and thermally, and atomic resolution was achieved on these low atomic number samples.

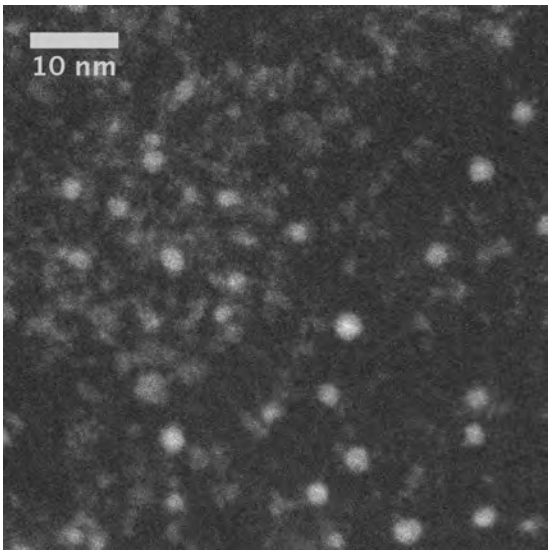

(a) HAADF image

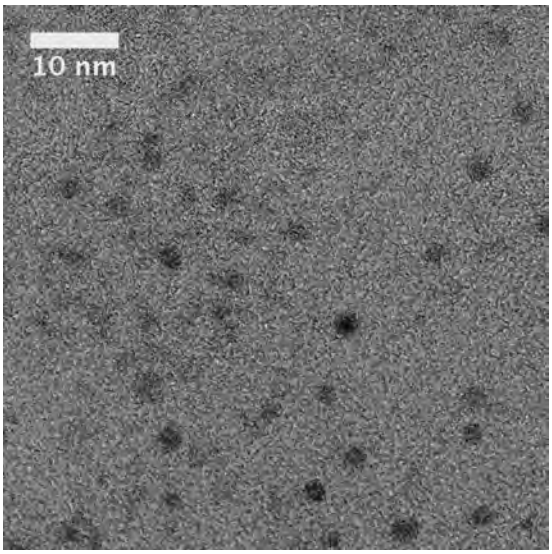

(b) BF image

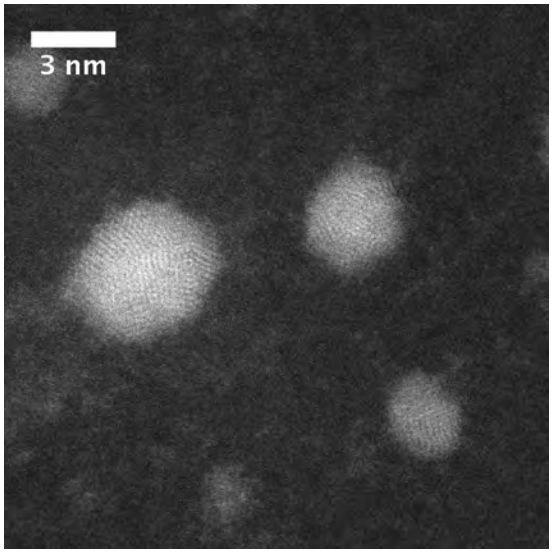

(c) HAADF image

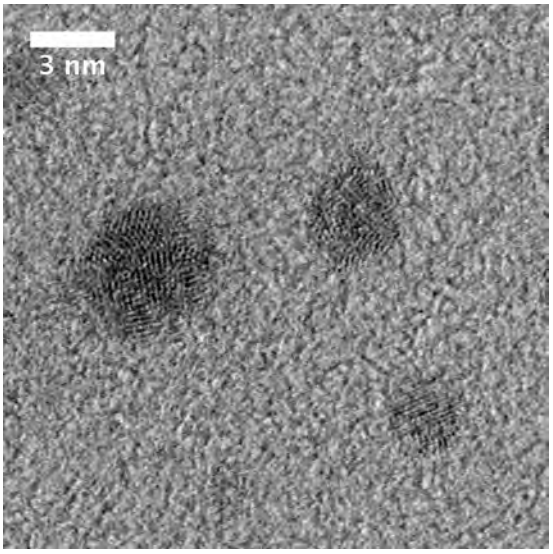

(d) BF image

Figure 5.6: HAADF (a,c) and BF (b, d) images of the same area taken simultaneously. In comparison to the HAADF images, it can be seen that the nanoparticle lattice fringes and the carbon background are much clearer in BF mode, allowing beam focusing and image optimisation.

5.4.2 STEM of Alginate/Iron Complexes

Alginates Form Long Range Networks

Alginate was incubated with iron and prepared as described in chapter 3. The sample was first imaged at relatively low magnification to assess the macro morphology. Large area STEM imaging revealed a gel-like network suspended over a holey carbon film, see figure 5.7 for examples. Areas with similar coverage could be found across the grid. These networks were often across the whole carbon substrate, but were easier to image when suspended over a hole in the carbon as this minimises the carbon contribution to the STEM intensity. It was found that under typical scanning conditions, the electron beam did not cause any noticeable damage to the sample, up to an hour after imaging.

The long range, relatively uniform structure typically observed over a large area (on the order on micrometres) indicates that alginates form long range structures instead of discrete particles. This is consistent with their polymeric nature and the 'gelling' nature of their binding that has been discussed above.

Nanoparticles Located within Long Range Networks

Within the network, bright features can be seen and due to their regular, spherical appearance these features are assumed not to be caused by thickness effects but rather the z-contrast nature of HAADF images allows us to attribute these to the formation of iron oxide nanoparticles within the network (see figure 5.8). These are spherical in shape and have a reasonably broad size distribution. Higher magnification images show atomic columns within the particles, as in figure 5.10.

The particles observed are found to be embedded within an alginate network rather than being isolated particles coated with a thin layer of alginate (analagous to the ferritin protein). There is

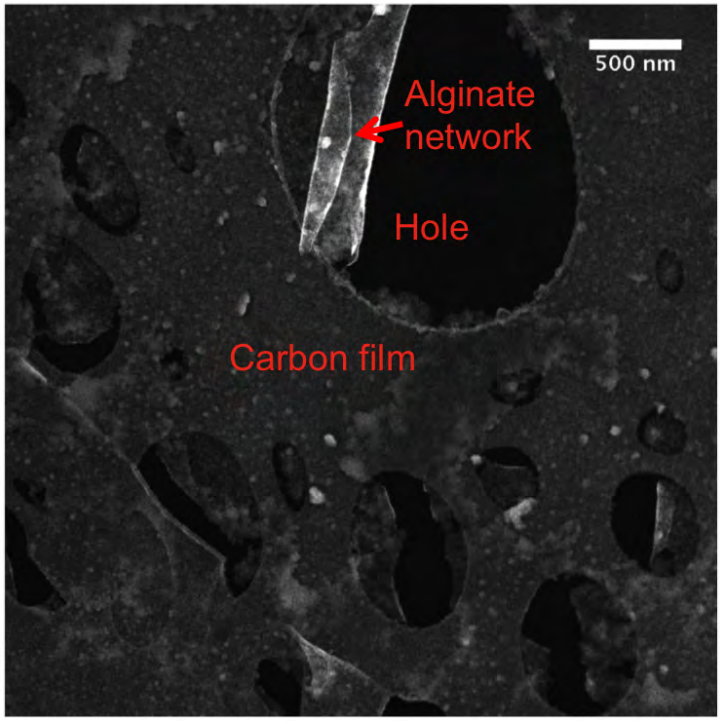

(a) Low magnification image showing a film suspended over a hole in holey carbon film

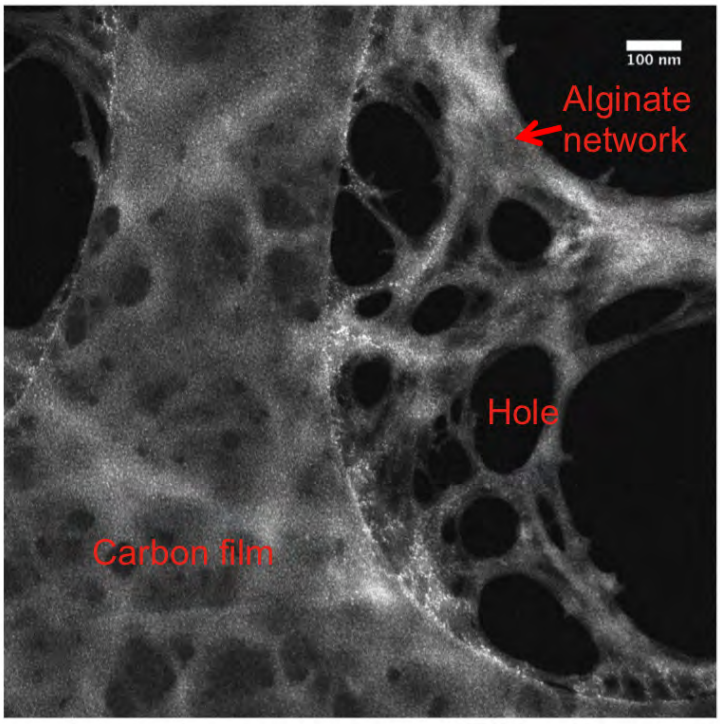

(b) Higher magnification image, where a network of strands can be seen

Figure 5.7: Large area images of alginate networks. These images show a long range coverage of a holey carbon film with a 'film' like network of alginate gel.

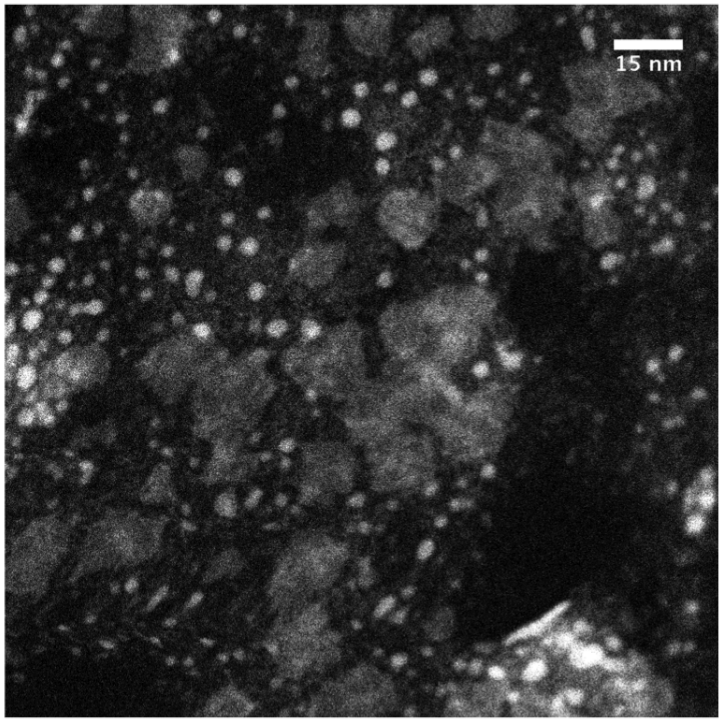

(a) Nanoparticles can be found within the network

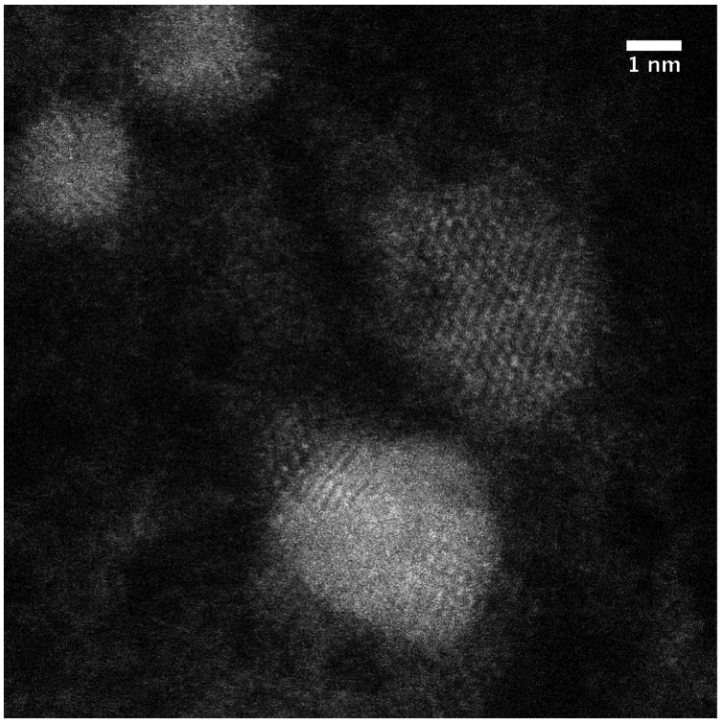

(b) Different morphologies of particles have been observed

Figure 5.8: Higher magnification HAADF-STEM images of alginate networks. These images demonstrate that nanoparticles can be found within the network.

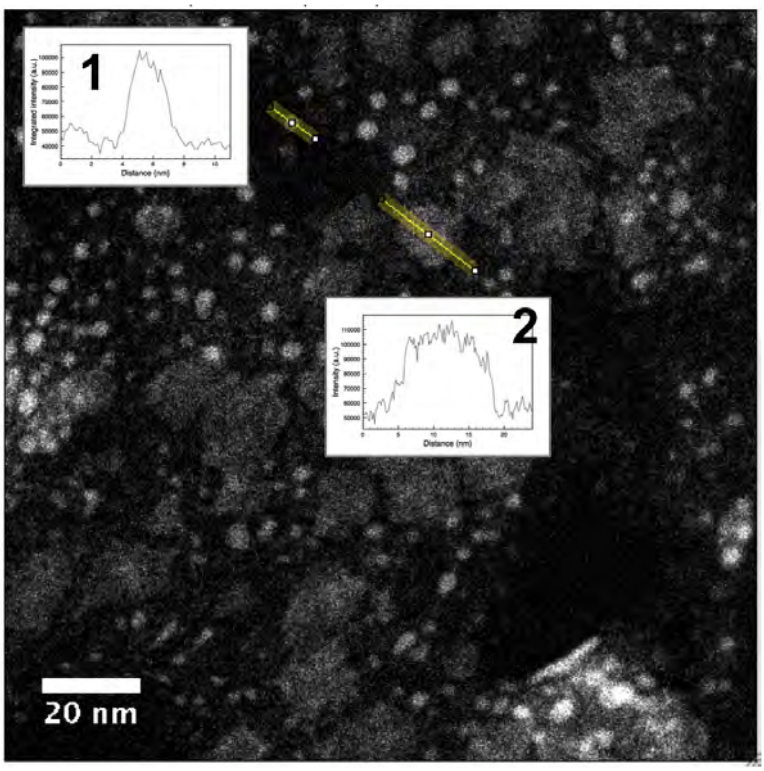

Figure 5.9: HAADF-STEM intensity profiles taken over two particles, demonstrating that both spherical (1) and flat (2) features are common.

a large degree of variation within the particles formed, different sizes and morphologies. This is most likely due to the physiological method of preparation, that mimics the human body but does not allow for any chemical modification to the reaction products. In figure 5.10, a HAADF-STEM image of an iron/alginate nanoparticle can be seen.

The large-area HAADF-STEM image in figure 5.8(a) demonstrates the variability in particle morphology with small spherical particles seen along with larger, flat structures that resemble flakes of material. To demonstrate this, line profiles were taken from two particles in figure 5.8(b) and these can be seen in figure 5.9. Particle 1 has a varying intensity profile, indicative of a spherical particle, whereas particle 2 has a 'flat' profile.

In addition to the nanoparticle formation, other morphologies have been observed. In figure 5.11 a long range alginate network with bound iron can be seen, with atomic resolution of single iron atoms surrounding the structure, and atoms within the structure. Both unattached, free iron can be seen (green arrow) and that associates with a long-range network (red arrows). This

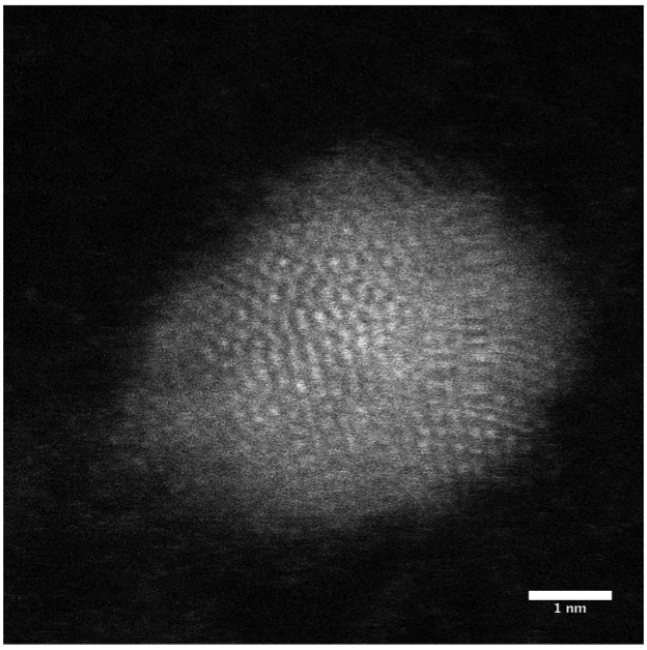

Figure 5.10: HAADF-STEM image of a nanoparticle found within the alginate network, demonstrating the ability to achieve atomic resolution of such clusters

demonstrates that nanoparticles are not the only structure found with this system and in addition there will be iron bound along unfolded alginate chains and also free, unbound iron.

These nanostructures have been formed in an environment that mimics physiological conditions. The method is very straight forward, a simple dialysis with no harsh chemical routines. This is in contrast to previously published work where iron nanoparticles are formed but in a pH 10 environment [14] .

5.4.3 Structural Characterisation

High resolution images obtained of the single particles were compared to those found in the literature [14, 24]. Fast fourier transforms were calculated of each particle and the inter atomic distances measured. Fe_2O_3 is also known as the mineral hematite, it has a corundum structure that can be indexed using either the hexagonal or rhombohedral lattices [25]. Ziolo *et al.*[14] state electron diffraction data for Fe_2O_3, where the atomic spacing range from 1.47 to 2.97 $\mathring{A}$. It can be seen in figures 5.12 that the values determined here are similar to this, indicating

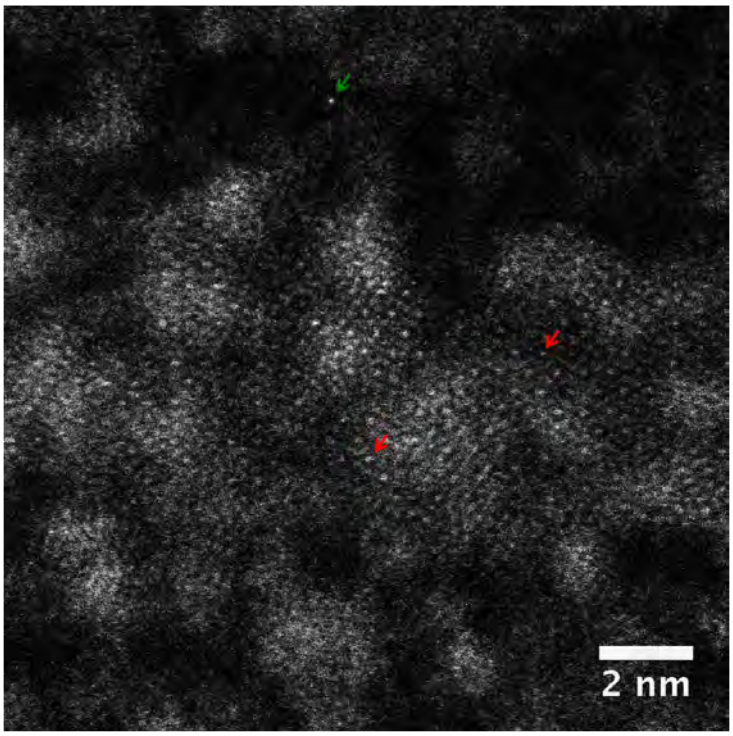

(a) Long range structure with single isolated iron atoms (green arrow) and as part of a network (red arrows) visible

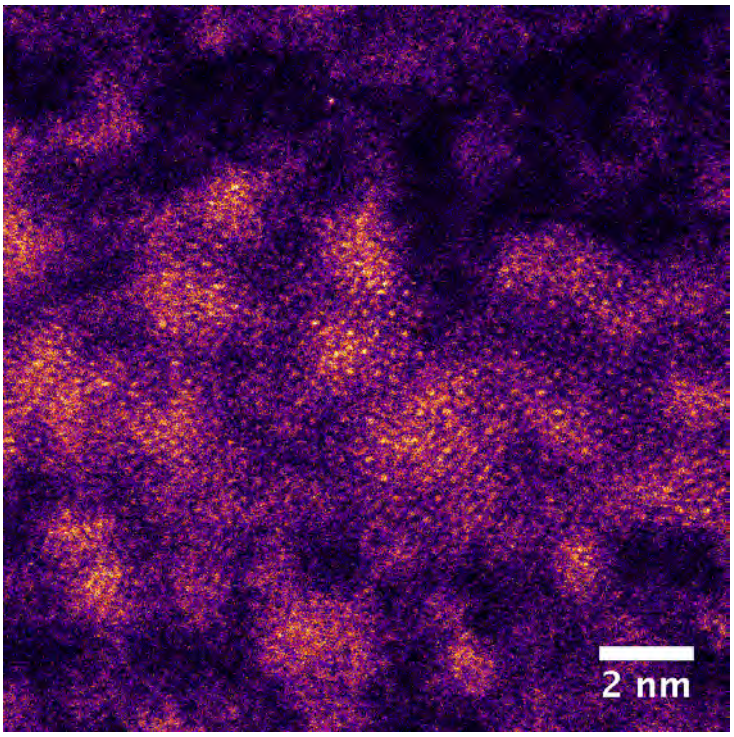

(b) False colour highlights the features

Figure 5.11: HAADF-STEM images reveal areas of long range iron binding. Single iron atoms can be seen (arrowed), both bound in a structure and 'free' on the carbon substrate.

that the iron oxide particles formed during the physiological incubation can be assumed to be Fe_2O_3.

A useful comparison can also be made between the nanoparticles formed in these samples and that of ferritin. Ferritin, as discussed in previous chapters, has been studied at length and nanodiffraction studies have been performed by Quintana *et. al.* [24]. Although the size of ferritin is slightly bigger, a broad similarity can be found in that both contain iron oxide species surrounded by an organic polymer or protein. This comparison is promising as clearly ferritin is biocompatible, and so if the alginate coated nanoparticles are similar in composition this bodes well for their physiological behaviour.

The diameter distribution was measured and plotted in a histogram (figure 5.13). The mean diameter was 1.78 ± 0.70 nm. The size of the nanoparticles is important, as this will significantly effect their behaviour within a biological environment. The smaller the nanoparticle, the more chance that they will enter into a cell by endocytosis or other means. However, this is less likely if the particle is embedded in a larger alginate network.

If the concentration of the alginate is increased to 0.2% in water, with the same concentration of iron, a different morphology was seen. An example is shown in figure 5.14, where large globular areas of alginate with brighter parts embedded, can be seen. This indicates that with a larger concentration, the alginate stops forming long range networks and instead forms denser, globular areas. This is in contrast to the discrete nanoparticles within a thin film seen previously.

Iron Control

Control samples were made of iron only and were imaged to ensure the particles observed in the alginate + iron samples were not an artefact of either on its own. Figure 5.15 shows a HAADF-STEM image of an iron chloride only solution deposited onto a carbon coated TEM grid using

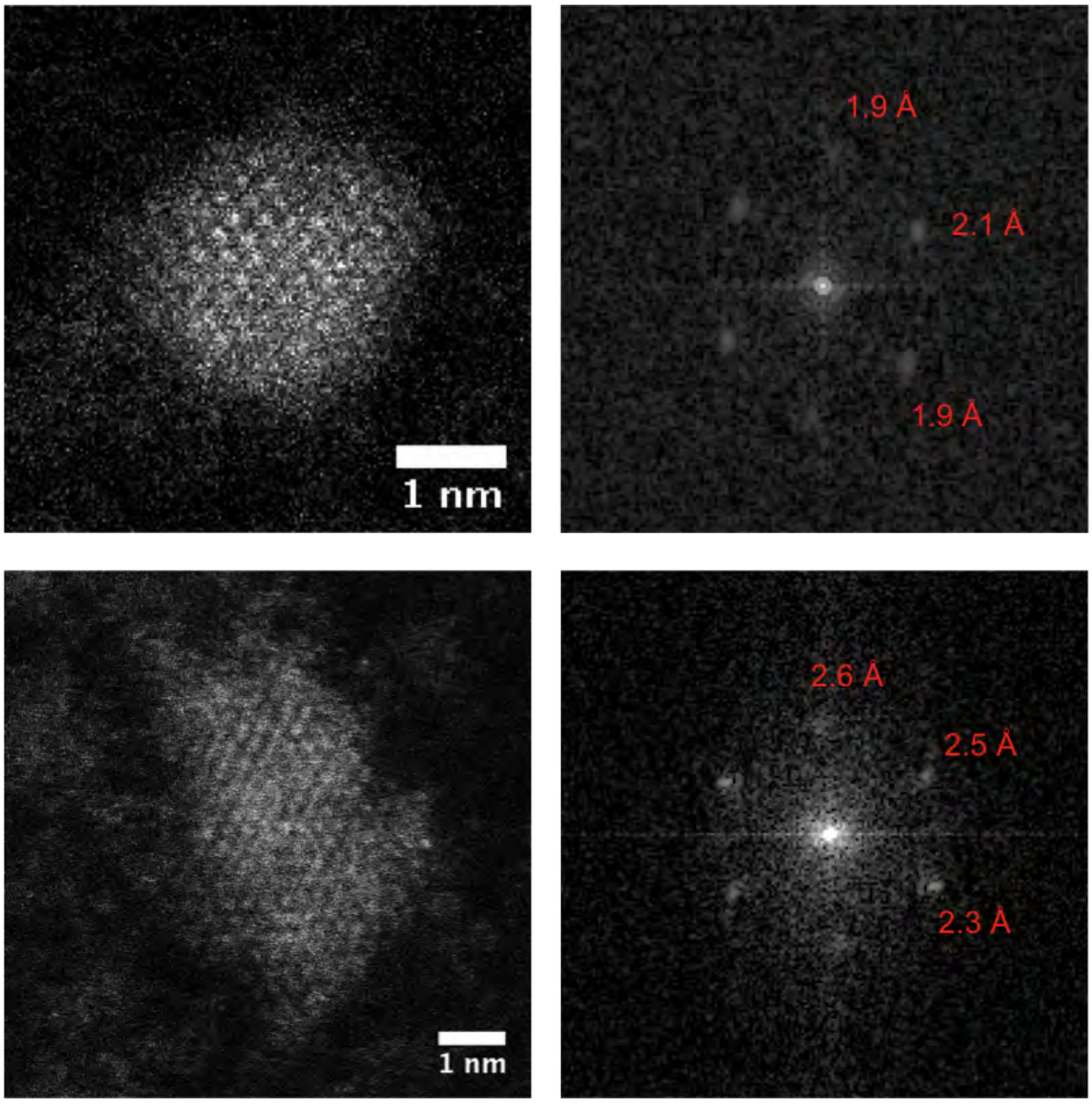

Figure 5.12: Fourier transform analysis of HAADF-STEM images of single nanoparticles reveals the same Fe_2O_3 structure as found by Ziolo *et al.*[14].

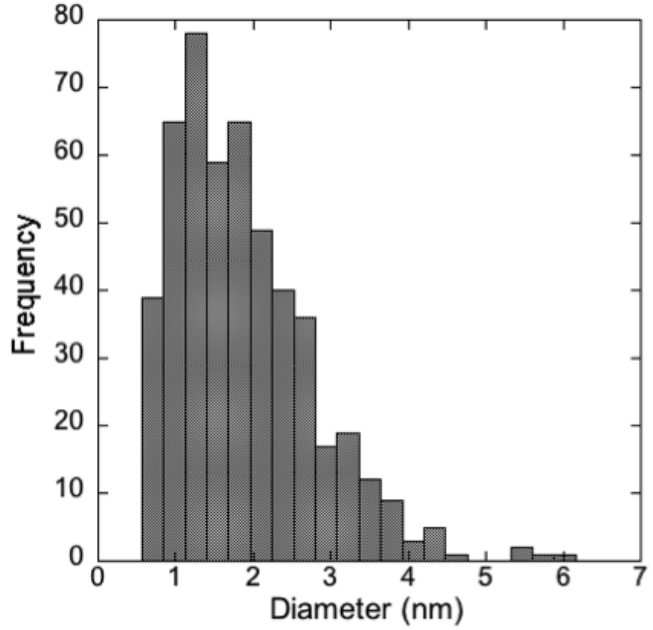

Figure 5.13: A wide range of nanoparticle diameters was found

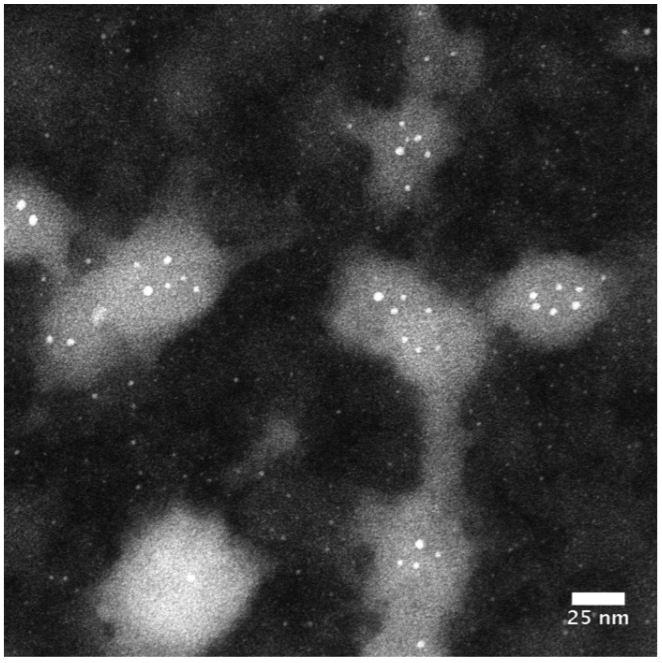

Figure 5.14: A higher concentration (0.2%) of alginate results in a morphology change in the network, with globular areas of alginate seen rather than the long range structures seen in figure 5.8

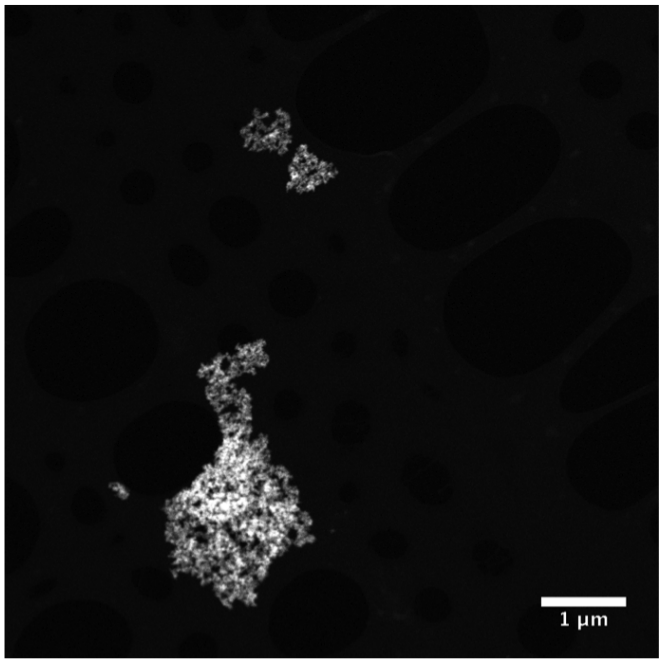

Figure 5.15: HAADF-STEM image of an iron only solution deposited onto a carbon coated TEM grid as a control

the same protocol as described above. It can be seen that large (micrometre) scale iron crystals are formed with no features similar to those found when iron is incubated with alginate.

5.4.4 EDX of Alginate/Iron Complexes

STEM-EDX was carried out on the higher concentration (0.2%) sample. Figure 5.16 demonstrates that both iron and oxygen is localised in the same region as the alginate/iron complex. This gives further evidence that the alginates bind iron as an oxide. Sodium is also highlighted as it is a component of the alginate and copper as a control signal, given that a copper EM grid was used. As this is a higher concentration sample, the morphology of the gel is slightly different, in that it is more globular on the substrate. This means that beyond the circle of gel is only carbon film. This enhances the effect of the EDX map.

When examining the samples with 0.1% alginate there is a surprising lack of localisation of iron in areas where the nanoparticles are surrounded by alginate gel (figure 5.17). It could be proposed that this is due to iron binding across the network that does not always result in

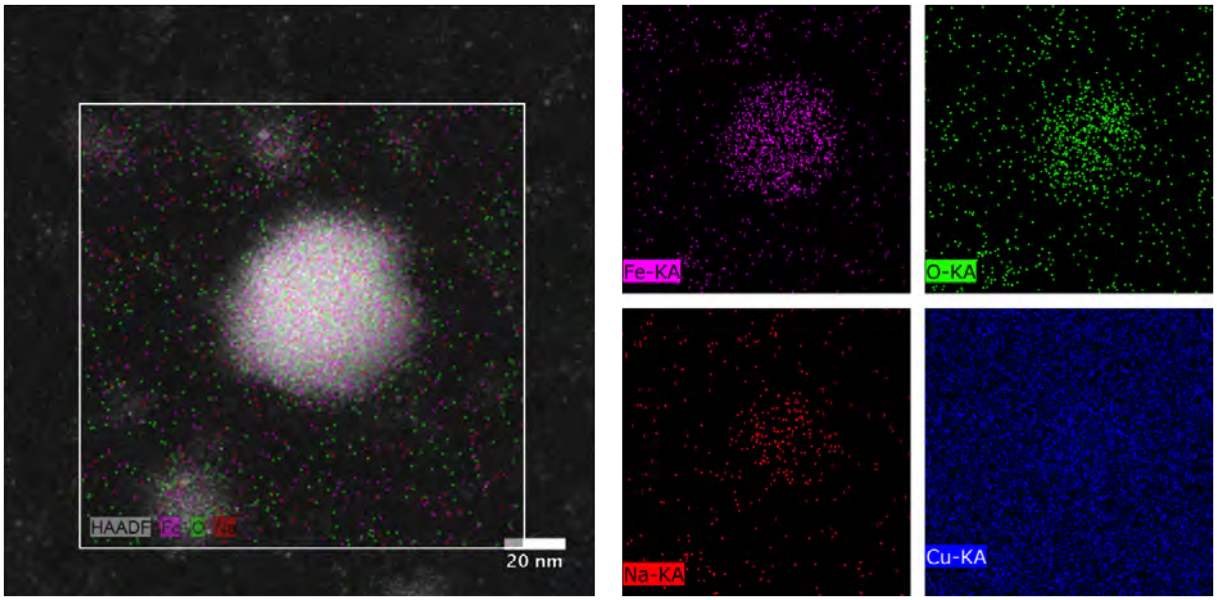

Figure 5.16: EDX mapping of iron/alginate gel with 0.2% alginate concentration. It can be seen that there is iron, oxygen and sodium localisation in the sample area. The copper is present from the copper TEM grid.

nanoparticle formation. This means that the total amount of iron across the region of interest stays constant, it is only the structure in which it is bound that changes. It is important to take into consideration that this is relatively low counts and low magnification that is subject to drift, a general issue with EDX as a technique that means interpretation of the signal is not trivial.

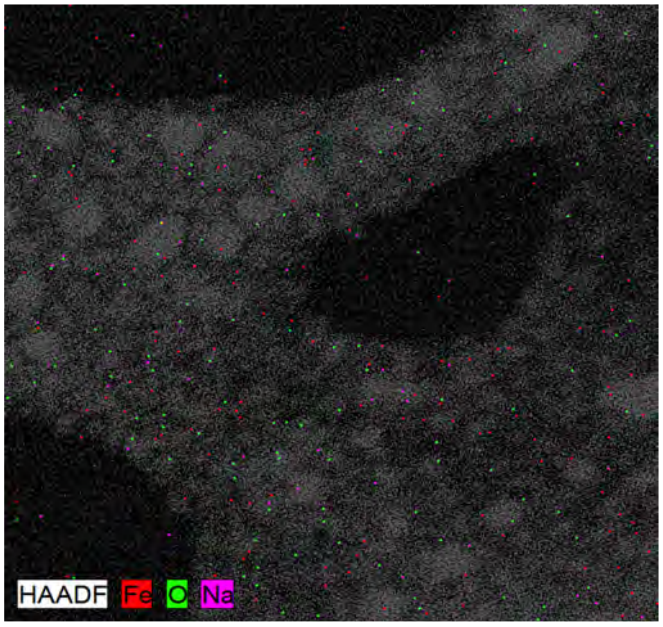

Figure 5.17: EDX mapping of iron/alginate gel with 0.1% alginate concentration. There is no concentration of iron signal in the areas where nanoparticles reside, indicating that there is a more even iron coverage across the gel and not just in the nanoparticles.

5.4.5 The Impact of Calcium

In order to accurately simulate physiological conditions the influence of calcium on the structures formed was investigated. Calcium is present in the bowel and due to the 'egg-box' structure that has been found, it was necessary to see the effect of calcium and whether the preferential binding for calcium effected the iron nanoparticles formed in iron only samples.

The sample was made by adding the same concentration of calcium as iron at the same time as iron into the incubation solution. STEM imaging revealed that the presence of calcium has a significant influence on the structures formed during incubation. Instead of discrete nanoparticles, as in figure 5.8, flake-like formations were found as shown by the typical example given in figure 5.18. These were present across the grid, and embedded in an alginate network, as with the iron-only samples.

A calcium only sample was also made, which was extremely beam sensitive, see Figure 5.19. A large scale film was found with very small bright features within it, which could be single calcium atoms. However, it was difficult to perform further in-depth imaging or analysis because the film was destroyed after less than a minute of imaging. This could be due to a number

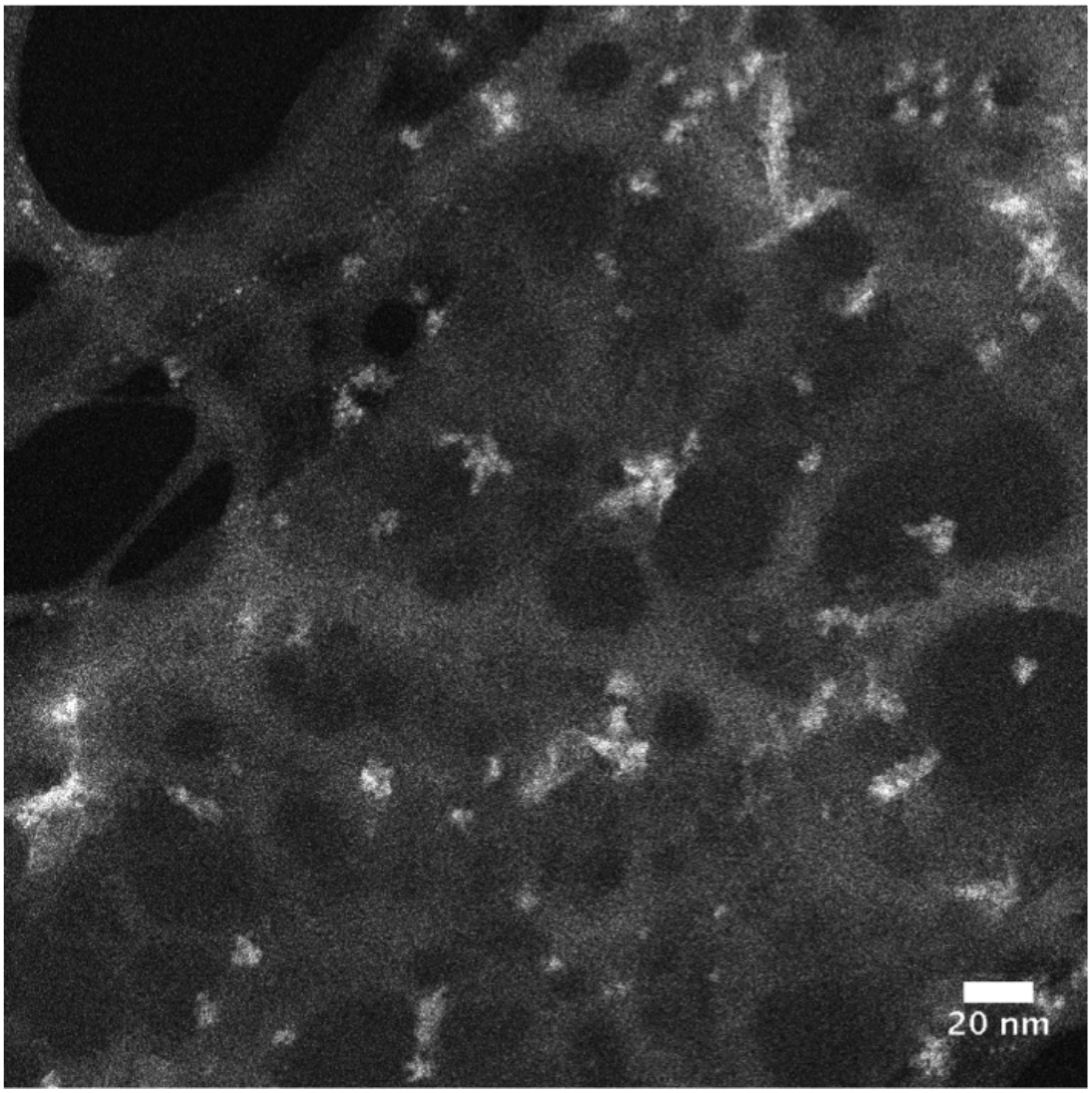

Figure 5.18: The addition of calcium seems to have an effect on nanostructure morphology, with ‘flakes’ rather than spherical particles found.

of reasons, particularly when taking into account the alginate control samples which also show this type of morphology. This indicates that the presence of iron strengthens the alginate gel, making it more resilient to the electron beam.

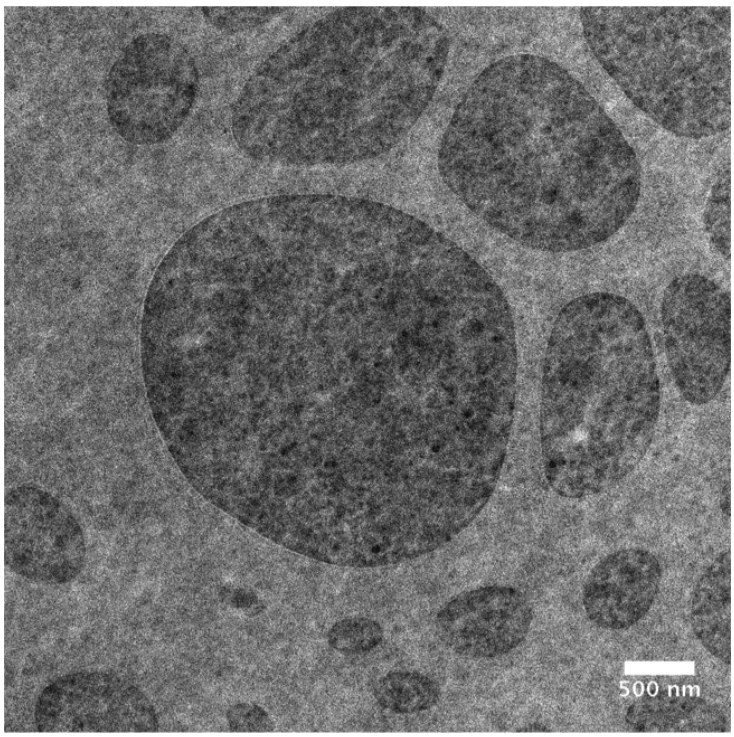

(a) Less structured, even coverage film

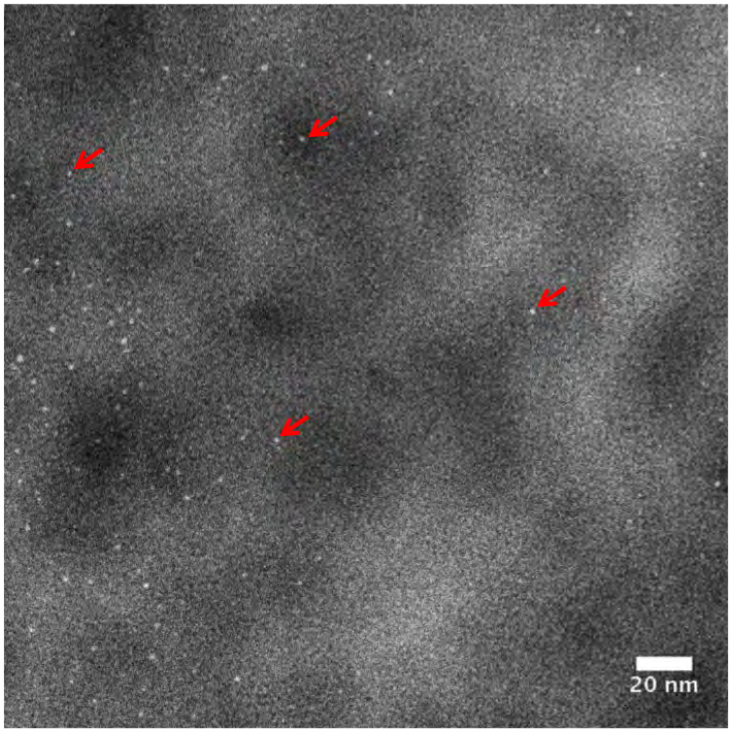

(b) Bright features within the film

Figure 5.19: When calcium is mixed with alginate without iron, there are no particles found and instead a film with very small (possibly atom sized) bright features, some examples are highlighted with red arrows. This sample was particularly beam sensitive.

5.4.6 Supporting Cell Studies

Cell studies have been performed where the effect of alginates and excess iron has been studied. This was performed by collaborator Richard Horniblow from the University of Birmingham and based in the Cancer Sciences and Chemistry departments.

It has been found that when alginates and iron are added to cells in a medium the total amount of iron in a ferrozine assay increases, however there is no increase in ferritin production. This suggests that the extra iron is not entering the cell to induce ferritin production, but instead is being captured by the alginate outside the cell and 'sticking' to the edge. This was further investigated by confocal microscopy imaging of fluorescently labelled alginates. Figure 5.20 shows a confocal image with the fluorescently labelled alginates in green, the nucleus in blue and plasma membrane in purple. It can be seen that the alginates reside around the edge of the plasma membrane although more imaging should be performed to visualise the other cellular components.

Although individual nanoparticles cannot be visualised with confocal microscopy, it could be suggested that the alginate networks seen in the HAADF-STEM imaging presented in this chapter are forming in a cellular environment and capturing iron in the form of nanoparticles, preventing the iron from entering the cell. This is a promising in terms of behaviour in the bowel, as excess luminal iron could be captured via the same mechanism.

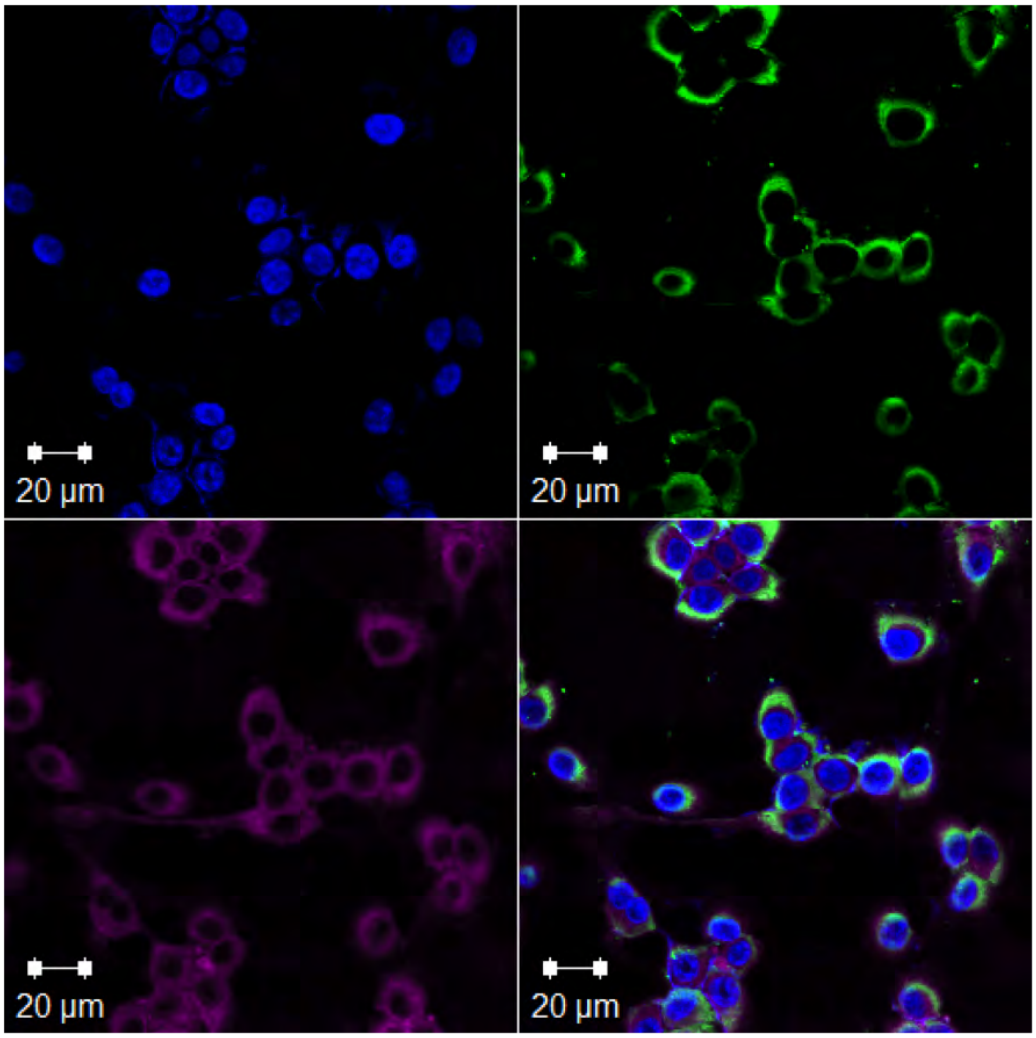

Figure 5.20: Confocal microscopy of fluorescently labelled alginate/iron mixtures (green) in a cellular environment (nucleus - blue, plasma membrane - purple). Please note this work was carried out by RH.

5.5 Conclusions

It has been found that when iron is added to alginate in solution and under physiological constraints, iron oxide nanoparticles are formed. This could be a key discovery if, as is planned, a bowel cancer therapy is developed by exploiting the iron chelating properties of alginates. It is important to re-iterate that the nanostructures found with this HAADF-STEM study are not the only incarnation of iron binding. Long range binding is common, as can be seen in Figure 5.11. Also iron atoms will be bound singularly to alginate molecules. This means that the bond formation is not trivial and supporting physical methods have provided insight into this, more discussion of this is found in section 5.2.5.

Further work needs to be carried out in order to fully characterise the behaviour of alginates within a cellular environment. Towards this and as discussed, some preliminary work has already been performed via confocal microscopy of fluorescently labelled alginate molecules. Conventional TEM will also be performed on fixed cell sections in order to locate any nanoparticles within a cell. In addition to ascertaining whether any nanoparticles formed enter the cell, this will enable them to be located within specific areas of a cell and if so, a rough quantification of how many nanoparticles enter.

More work is required to ascertain the detailed formation mechanism of the particles. It is currently assumed that the iron binds to the polymer backbone and after a certain number of bonds are formed the strand collapses in on itself and a nanoparticle is formed. This could be investigated by looking at different alginate polymers of varying length, and assessing whether this effects particle formation.

More detailed structural characterisation could be performed, including STEM-EELS to allow for the type of iron oxidation state (i.e. 2+ or 3+) on a per particle basis. This requires excellent sample stability and corrector alignment along with detector alignment and the correct area in the spectra being examined. This technique can also be performed at a higher, atomic

level magnification. In terms of sample preparation, glow discharging grids could prove a wise addition to the protocol so that particles wet the substrate and distribute more evenly.

Future clinical work will involve whole mice studies using radioactive iron and alginate to monitor uptake in the body. Early work has been performed by RH and suggests that when mice ingest iron along with alginate, the concentration of iron they excrete is higher than iron only. This suggests that alginate is behaving as expected by capturing the iron and allowing excretion. A clinical trial is now in the early stages of development and the results of this will determine the viability of he iron chelating alginates mechanism as a drug therapy for treating bowel cancer.

References

[1] A. Jemal, F. Bray, M. M. Center, J. Ferlay, E. Ward, and D. Forman. Global cancer statistics. *CA: a cancer journal for clinicians*, 61(2):69–90, 2011.

[2] NHS. Bowel cancer screening programme, July 2013.

[3] S. Radulescu, M. J. Brookes, P. Salgueiro, R. A. Ridgway, E. McGhee, K. Anderson, S. J. Ford, D. H. Stones, T. H. Iqbal, C. Tselepis, et al. Luminal iron levels govern intestinal tumorigenesis after *Apc* loss in vivo. *Cell Reports*, 2012.

[4] P. J. Morin, A. B. Sparks, V. Korinek, N. Barker, H. Clevers, B. Vogelstein, and K. W. Kinzler. Activation of β-catenin-tcf signaling in colon cancer by mutations in β-catenin or APC. *Science*, 275(5307):1787–1790, 1997.

[5] R. Fodde. The *APC* gene in colorectal cancer. *European Journal of Cancer*, 38(7):867–871, 2002.

[6] R. L. Nelson. Dietary iron and colorectal cancer risk. *Free Radical Biology and Medicine*, 12(2):161–168, 1992.

[7] R. L. Nelson. Iron and colorectal cancer risk: human studies. *Nutrition reviews*, 59(5):140–148, 2001.

[8] L. B. Saltz, S. Clarke, E. Díaz-Rubio, W. Scheithauer, A. Figer, R. Wong, S. Koski, M. Lichinitser, T-S Yang, F. Rivera, et al. Bevacizumab in combination with oxaliplatin-based chemotherapy as first-line therapy in metastatic colorectal cancer: a randomized phase iii study. *Journal of Clinical Oncology*, 26(12):2013–2019, 2008.

[9] O. Smidsrød. Molecular basis for some physical properties of alginates in the gel state. *Faraday Discuss. Chem. Soc.*, 57:263–274, 1974.

[10] N. E. Simpson, C. L. Stabler, C. P. Simpson, A. Sambanis, and I. Constantinidis. The role of the $CaCl_2$–guluronic acid interaction on alginate encapsulated β tc3 cells. *Biomaterials*, 25(13):2603–2610, 2004.

[11] G. Li, Y. Du, Y. Tao, H. Deng, X. Luo, and J. Yang. Iron (ii) cross-linked chitin-based gel beads: Preparation, magnetic property and adsorption of methyl orange. *Carbohydrate Polymers*, 82(3):706–713, 2010.

[12] M. A. K. Williams, A. Marshall, R. G. Haverkamp, and K. I. Draget. Stretching single polysaccharide molecules using AFM: A potential method for the investigation of the intermolecular uronate distribution of alginate? *Food Hydrocolloids*, 22(1):18–23, 2008.

[13] P. Sikorski, F. Mo, G. Skjåk-Bræk, and B. Stokke. Evidence for egg-box-compatible interactions in calcium-alginate gels from fiber X-ray diffraction. *Biomacromolecules*, 8(7):2098–2103, 2007.

[14] E. Kroll, F. M. Winnik, and R. F. Ziolo. In situ preparation of nanocrystalline γ-Fe2O3 in iron (ii) cross-linked alginate gels. *Chemistry of materials*, 8(8):1594–1596, 1996.

[15] A. K. Gupta and M. Gupta. Synthesis and surface engineering of iron oxide nanoparticles for biomedical applications. *Biomaterials*, 26(18):3995–4021, 2005.

[16] T. K. Jain, M. A. Morales, S. K. Sahoo, D. L. Leslie-Pelecky, and V. Labhasetwar. Iron oxide nanoparticles for sustained delivery of anticancer agents. *Molecular pharmaceutics*, 2(3):194–205, 2005.

[17] D. L. J Thorek, A. K. Chen, J. Czupryna, and A. Tsourkas. Superparamagnetic iron oxide nanoparticle probes for molecular imaging. *Annals of biomedical engineering*, 34(1):23–38, 2006.

[18] C. Martinez-Boubeta, K. Simeonidis, A. Makridis, M. Angelakeris, O. Iglesias, P. Guardia, A. Cabot, L. Yedra, S. Estradé, F. Peiró, et al. Learning from nature to improve the heat generation of iron-oxide nanoparticles for magnetic hyperthermia applications. *Scientific reports*, 3, 2013.

[19] Y. Lu, Y. Yin, B. T. Mayers, and Y. Xia. Modifying the surface properties of superparamagnetic iron oxide nanoparticles through a sol-gel approach. *Nano Letters*, 2(3):183–186, 2002.

[20] C. Li, T. Chen, I. Ocsoy, G. Zhu, E. Yasun, M. You, C. Wu, J. Zheng, E. Song, C. Z. Huang, et al. Gold-coated Fe3O4 nanoroses with five unique functions for cancer cell targeting, imaging, and therapy. *Advanced Functional Materials*, 2013.

[21] P. Sipos, O. Berkesi, E. Tombácz, T. G. St Pierre, and J. Webb. Formation of spherical iron (iii) oxyhydroxide nanoparticles sterically stabilized by chitosan in aqueous solutions. *Journal of inorganic biochemistry*, 95(1):55–63, 2003.

[22] E. Sourty, S. van Bavel, K. Lu, R. Guerra, G. Bar, J. Loos, et al. High-angle annular dark field scanning transmission electron microscopy on carbon-based functional polymer systems. *Microscopy and Microanalysis*, 15(3):251, 2009.

[23] J. Loos, E. Sourty, K. Lu, G. de With, and S. v. Bavel. Imaging polymer systems with high-angle annular dark field scanning transmission electron microscopy (HAADF- STEM). *Macromolecules*, 42(7):2581–2586, 2009.

[24] C. Quintana, J. M. Cowley, and C. Marhic. Electron nanodiffraction and high-resolution electron microscopy studies of the structure and composition of physiological and pathological ferritin. *Journal of structural biology*, 147(2):166–178, 2004.

[25] G. K. Lewis Jr and H. G. Drickamer. Effect of high pressure on the lattice parameters of CrO and α-FeO. *The Journal of Chemical Physics*, 45:224, 1966.

Chapter 6

Transmission Electron Microscopy of Encapsulated Membrane Proteins

6.1 Introduction

In this chapter, an electron microscopic study exploring the use of self-assembled, membrane-mimicking nano structures to isolate membrane proteins is presented. Transmission electron microscopy (TEM) has provided direct insight into the individual nano structures and the morphology changes induced by the surrounding environment.

All the sample preparation presented in this chapter was performed by collaborators in Cancer Sciences (Michael Overduin and Timothy Knowles), who also developed the self assembling nano structures that are investigated in this chapter. All of the imaging and associated image analysis was conducted by the author.

The work presented in this chapter has contributed towards the following publication:
Characterisation of a hybrid particle that provides a nanoscale lipid membrane environment capable of extracting membrane proteins. Mohammed Jamshad, Vinciane Grimard, Illaria Idini, Tim J. Knowles, Miriam R. Dowle, Naomi Schofield, Yu-Pin Lin, Rachael Finka, Richard E.

Palmer, Michael Overduin, Cdric Govaerts, Jean-Marie Ruysschaert, Karen J. Edler, Tim R. Dafforn. *Submitted to Biophysics.*

6.2 Literature Review

6.2.1 Membrane Proteins

The cell membrane is the gateway to the cell, controlling what enters and leaves and the rate of this transmembrane transport [1]. The membrane itself can also react by performing either endo- or exo-cytosis which changes the shape of the membrane to allow a section to 'bud off' and become a small vesicle that either enters or exits the cellular environment with some cargo. The membrane is a lipid bilayer with integrated proteins that perform many different roles, such as protein folding. Collectively known as membrane proteins, these can either span the whole membrane, be embedded within it or protrude from the cell at either end.

Membrane proteins make up 30% of all proteins and 50% of drug targets [1], this renders understanding their structure in the highest detail essential. Cell signalling is dependant on membrane proteins to provide information through the membrane and help maintain homeostasis. This is the reason that so many drugs target the membrane proteins.

Bacterial cell types can be classified into two groups by their membrane structure: gram positive and gram negative. Gram positive bacteria have a membrane covered in a thick peptidoglycan layer whereas gram negative bacteria have two lipid membranes (inner and outer) separated by the periplasm, illustrated in figure 6.1. They can be identified by their contrasting reaction to gram staining, which is determined by their membrane structure. One of the most extensively studied bacteria is E.coli which is gram negative. One of the proteins associated with the E.coli outer membrane is PagP.

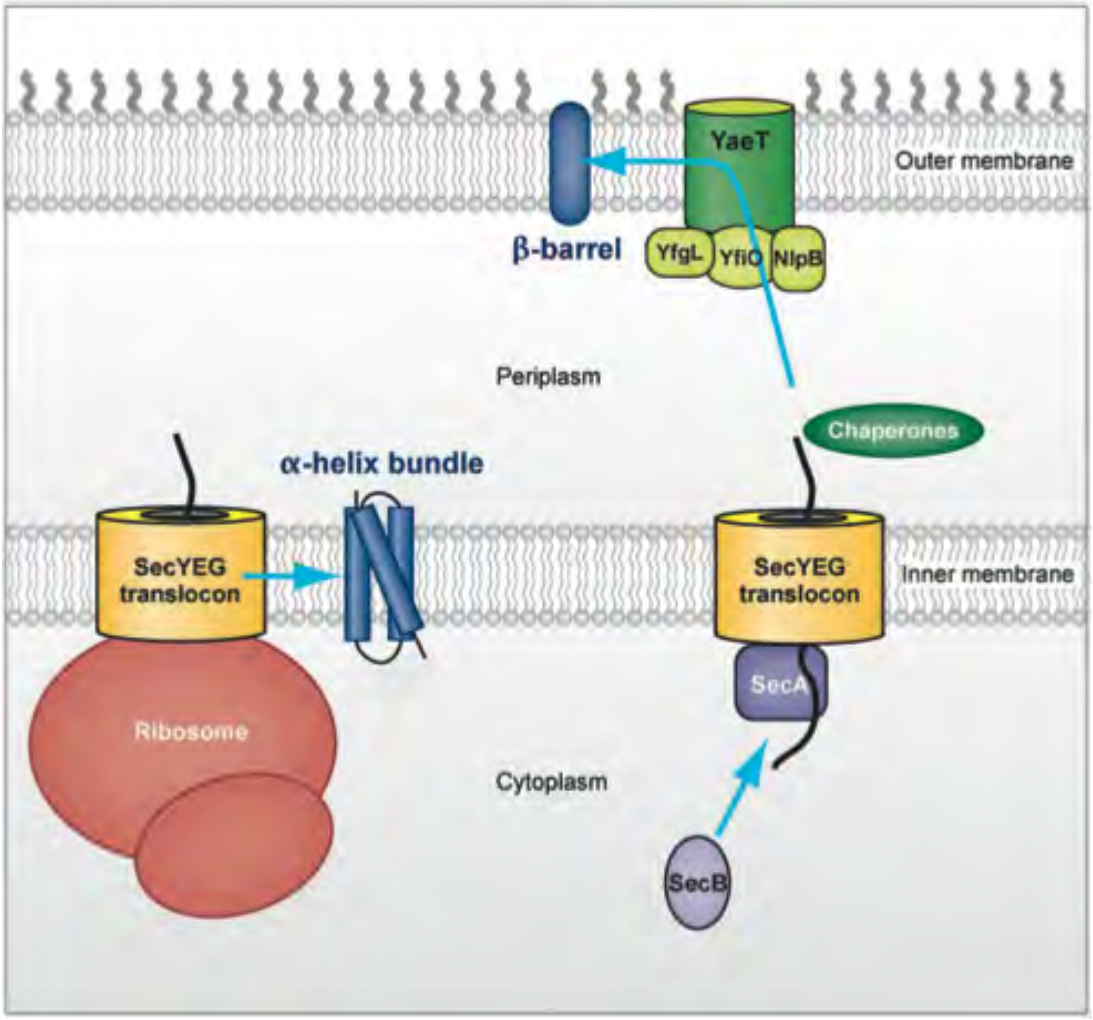

Figure 6.1: Schematic of the gram negative bacterial cell membrane. This shows the lipopolysaccharide layer on the outside surface of the membrane and the double membrane structure. Several different membrane proteins are shown, with some (SecYEG translocon) spanning the inner membrane and others (YaeT) spanning the outer membrane and protruding out of the cell. Figure modified from [2].

6.2.2 The PagP Protein

In this work, the main protein studied is the bacterial outer membrane protein PagP. Involved in eliciting an immune response, PagP has an active site lying outside the membrane [3]. It provides a site for 'palmitoylation' or attachment of fatty acids to lipid A which is a molecule thought to be responsible for toxicity in gram negative bacteria [4, 5]. It acts to maintain lipid asymmetry in the E.coli outer membrane, which is essential for function.

If an inhibitor of PagP can be designed, this would reduce the risk of bacterial infection, however this requires the structure to be fully elucidated first. In order to do this the protein must be purified in solution or crystallised so that physical characterisation such as NMR can be carried out. Membrane proteins are notoriously difficult to isolate due to the fact that they often lose conformation if not residing in a membrane. Novel solutions to this have been sought, discussed in further detail in the following sections.

The structure of PagP has been elucidated [3] and has been found to consist of an eight-stranded -barrel preceded by an amphipathic α helix. However, it is a useful test protein to use in order to refine the solubilization procedures and technique in anticipation of using the nano-disc to isolate an unknown structure.

6.2.3 Standard Characterisation Techniques

Structural characterisation of proteins at an atomic scale is traditionally achieved through crystallisation of the protein and subsequent x-ray diffraction studies [6]. The drawback of this is that the protein first needs to be isolated and then crystallised, both of which are non-trivial for non-membrane proteins. This is because proteins are sensitive to very small changes in conditions (temperature, humidity etc) often precipitate out of solution or lose conformation during the process, let alone those commonly residing within the membrane [7]. There are several

techniques that do not require crystallisation, but instead can be performed on hydrated proteins in solution and are now discussed.

Nuclear magnetic resonance (NMR) spectroscopy can be performed without crystallisation, on proteins in solution. Here the magnetic response of atoms within a protein can be measured, and after complex computation a model of the atomic structure of the protein can be developed. Since it can be performed in solution, this technique is popular however, the major limitation of NMR is that it cannot be used for proteins over 40kDa which limits its applications [8]. For example, the structure of the antibody binding Protein A has been elucidated using NMR [9].

Small angle X-ray scattering (SAXS) exploits the scattering of X-rays from molecules at small angles to calculate the shape and size of the target [10]. The advantage of this technique is that it can be performed on hydrated proteins in liquid, however this does need to be performed at a synchrotron, a resource which is not easily accessible. The resolution limit for this technique is around 5nm [11], which means a rough estimation of size can be performed but detailed structural analysis is not possible.

Dynamic light scattering (DLS) can also be used to calculate the overall size of biological molecules in solution. A laser is used to interrogate a suspension of molecules, and the fluctuation of the scattered light intensity is measured over time to measure the size of particles [12]. This again has the advantage of being able to sample a large number of molecules in liquid and gain a broad size distribution, however detailed (i.e. atomic)structural information is not able to be determined [13].

All the techniques above require the protein in question to be isolated in solution with as little modification to their structure as possible. This is especially true of NMR, where atomic characterisation is possible on solubilized samples. As mentioned, membrane proteins are difficult to solubilize due to their hydrophobicity however, techniques have been developed to try to

overcome this and are discussed below.

6.2.4 Methods of Isolating Membrane Proteins

In order to elucidate the structure of a protein, it is necessary to isolate it, preferably without denaturing or damage occurring. Detergent based methods are the most popular isolation protocols. Detergents are amphiphatic molecules, ie they have hydrophillic and hydrophobic parts and in solution they generally form micelles that mimic a membrane bilayer [7]. The issue with detergents is that often they denature the protein during the isolation process, meaning any subsequent characterisation may not be relevant. Careful selection and extensive screening is required to choose the correct detergent and protein pairing.

Several alternatives to detergents have been developed, namely nano-discs, amphipols and fluoronated surfactants [14]. Amphipols are amphiphatic polymers that assemble around a protein, forming a belt that enables solubilization. Fluoronated surfactants are similar to detergents but without the denaturing effects.

Nanodiscs have been developed as an alternative method to solubilization using membrane scaffold proteins and lipids formed into a disc shape to simulate the membrane environment [15]. However nano discs use detergents for the preliminary steps, which can effect the proteins, as previously discussed. Developed in Birmingham, the SMALP (styrene maleic acid lipid particle) method is a nanotechnological solution to the problem, making use of self assembling nano disks to encapsulate the protein without the use of detergents [16, 17] or membrane scaffold proteins [15]. Instead a polymer is used to act as the building block of the ‘disc’. A schematic showing the assembly process of the nano disk around a membrane protein is shown in figure 6.2. [18]

The SMALP assembly process is pH dependant, when the pH is increased the SMA polymer

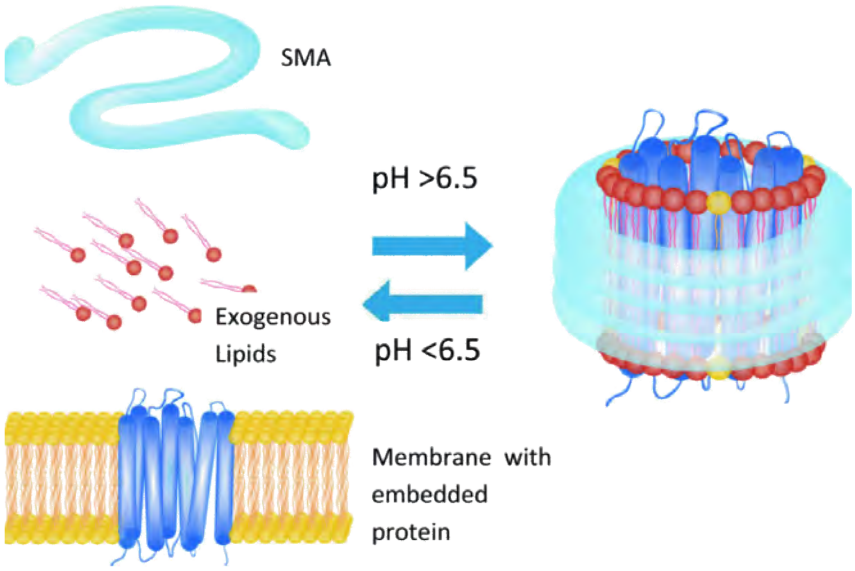

Figure 6.2: A schematic showing the pH dependant assembly of SMALP nanodisks around membrane proteins. With an increase in pH the components self assemble around the membrane to protein, allowing soubilization. Figure from [17].

self assembles around the exogenous lipids and membrane incorporating the protein. This is a straightforward reaction, similar to the formation of micelles or liposomes. Once assembled, the discs are suspended in solution holding the protein solubilized and ready for physical characterization.

SMALPs have been characterised using DLS and negative stain TEM [16]. The DLS studies demonstrated a size increase when the PagP protein is encapsulated by the disc [16]. This increase was from 9.0 ($\pm$1.1 nm) to 11.2 ($\pm$1.4 nm). Using negative stain the average diameter of 'empty' SMALPs was measured to be 10.2nm. However, negative stain tends to overestimate particle size and can interact with the protein changing the conformation. Whereas DLS is unable to measure the shape of a population, only the average size. And so, the aim of this work was to use cryo TEM to image the discs in a hydrated state to eliminate these issues and gain a more accurate measurement of their physical properties.

6.2.5 Electron Microscopy of Nanodisc/Membrane Protein Complexes

Transmission electron microscopy can be used to directly image a specimen, and thus provides distinct advantages over the techniques discussed previously, which involve detailed interpretation of the data in order to construct a model. TEM can often provide complimentary information to that obtained in the liquid-phase. The lack of high atomic number content in the samples means that high resolution HAADF-STEM is not an appropriate technique and so conventional TEM and cryo-TEM have been the principal electron microscopy techniques used in this field.

One of the earliest cryo-TEM studies on lipid vesicles was performed by Walter *et. al* [19]. The various structures of egg phosphatidylcholine and octyl glucoside present as vesicle-micelles which change at different concentrations. The transitions were monitored using cryo-TEM and shown to change from cylindrical vesicles to spherical ones. This was possible without negative staining and in the hydrated state, allowing insight into the structural changes of this system.

Advanced negative stain techniques have been used towards calculating the structure of membrane pore complexes [20]. Two methods were used to solubilise the anthrax pore complex; insertion into vesicles and nano-discs. This allowed a comparison of the two techniques, which found an indentical structure at $22\mathring{A}$ resolution using single particle reconstructions.

Single particle analysis has also been performed using cryo-TEM images of amphipol solubilized membrane proteins [21]. In this work the amphipol belt was directly imaged, and shown to replace the membrane lipid bilayer. A $19\mathring{A}$ cryo-EM map allowed the researchers to accurately map the direction and behaviour of electron transport in the molecule. This would not have been possible without the solubilization provided by the amphipol belt.

6.3 Aims

To conduct a direct imaging study via transmission electron microscopy in order to directly visualise a single nano-disc and the protein residing within it, for the first time. In order to perform this in the hydrated state, a supplementary aim was to develop protocols towards imaging discs containing membrane proteins using cryo-TEM.

Additional aims were to investigate any changes in morphology that occur as a result of the protein entering the disc and to use ligand mediated gold nanoparticle adhesion to aid in identifying proteins within the disc.

6.4 Results and Discussion

6.4.1 Preliminary Protocol Development

Sample Concentration

The concentration of a sample applied to the electron microscopy grid can hugely effect the imaging, as an over or under loaded grid can severely limit the imaging sensitivity. When initially studying the sample it was unclear what the appropriate sample concentration was, so a dilution with buffer solution (50mM sodium phosphate pH 7 + 100mM sodium chloride) was used to ascertain the correct concentration. An initial SMALP concentration of 5mg/ml was acquired as this is similar to that needed for SAXS or DLS studies. In figure 6.3 it can be seen that the sample diluted to $1X10^{-5}$ mg/ml in buffer solution is much less dense than that diluted to $1X10^{-3}$ mg/ml, as one would expect. It is therefore much easier to discern single nano-discs with a lower concentration. This means that the concentrations required for electron microscope samples are much smaller than that needed for solution studies such as SAXS (1-10mg/ml) or DLS (5mg/ml).

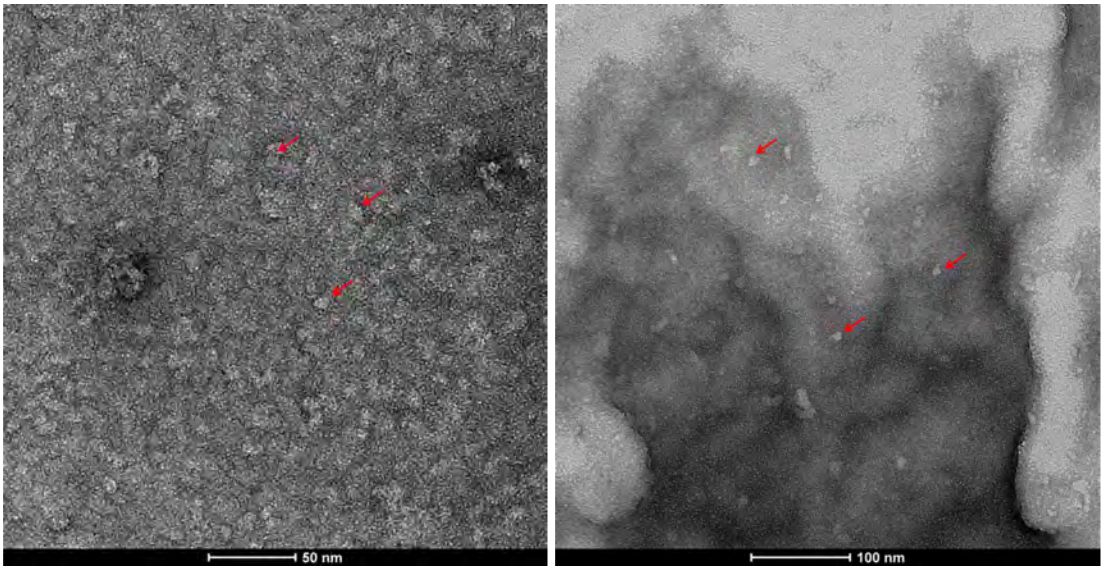

(a) $1X10^{-3}$ mg/ml dense features are seen which cannot be distinguished

(b) $1X10^{-5}$ mg/ml individual features (red arrows) are distinguishable

Figure 6.3: Determining the appropriate concentration of SMALP sample for negative stain TEM imaging. A much lower concentration is needed than that used for other characterisation techniques such as SAXS.

Figure 6.3 also illustrates shows how the sample can distribute unevenly on the substrate, leading to crystallisation and debris on the grid. The solution to this is glow discharging the carbon coated grid, discussed in the next section.

Glow Discharging

Glow discharging is a technique that is often used in the biological sciences to make the carbon coated electron microscopy grid hydrophillic or negatively charged [22, 23]. The grid is placed in a vacuum evaporator, between two parallel electrodes.Voltage is then applied between the two electrodes, causing a glow discharge which renders the grid negatively charged, and so hydrophillic. This means biological molecules, which on the whole are positively charged, adhere much better to the carbon substrate and wet the surface more effectively. Samples were prepared on amorphous carbon coated grids that had been glow discharged and compared to those that had not been through the glow discharge process. The difference between these two is illustrated in figure 6.4 .

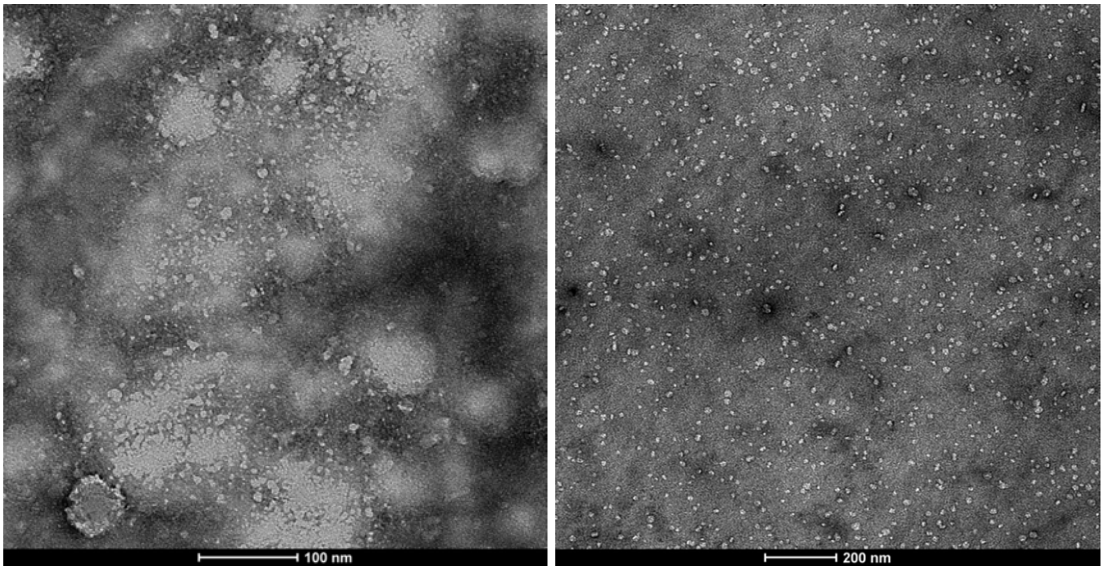

(a) no glow dishcarging (b) glow discharged

Figure 6.4: Demonstrating the effect of glow discharging the carbon film. It can be seen in figure 6.4(a) that the stain is uneven across the substrate and it is difficult to distinguish features whereas in figure 6.4(b) the features are easily seen.

Glow discharging clearly allows the sample not only to wet the substrate on a macro scale, but also on a nano (i.e. individual nano-disc) scale. The stain spreads much easier, resulting in less crystallisation and even coverage. The discs themselves are also distributed and aligned well to the grid. All samples were therefore imaged on glow discharged grids for both cryo and negative stained samples.

Negative Staining

The size of the stain also limits any high magnification work, as the heavy metal atoms mask any substructure. In figure 6.5 a comparison is made between imaging using TEM and cs-corrected STEM of the same sample (in this case the nano-discs studied in Chapter 6). It can be seen that when the higher resolution technique is used the individual atoms of the stain are imaged. This masks the underlying structure of the biomolecule and so for very high resolution work (ie with aberration corrected STEM) it is therefore not advisable to use a negative stain. For TEM however, it is essential to enhance the contrast of biological samples using a negative stain.

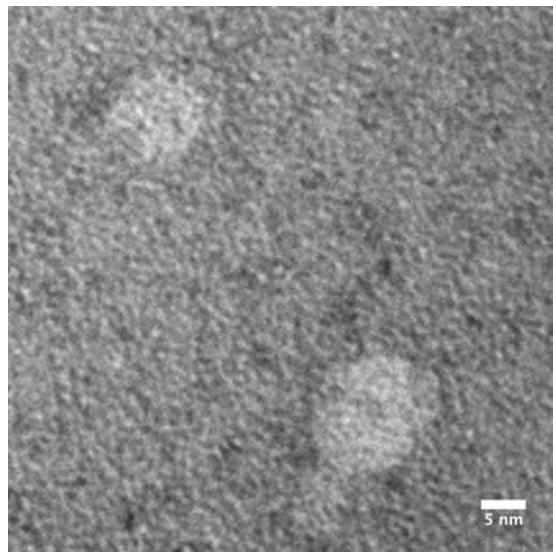

(a) TEM

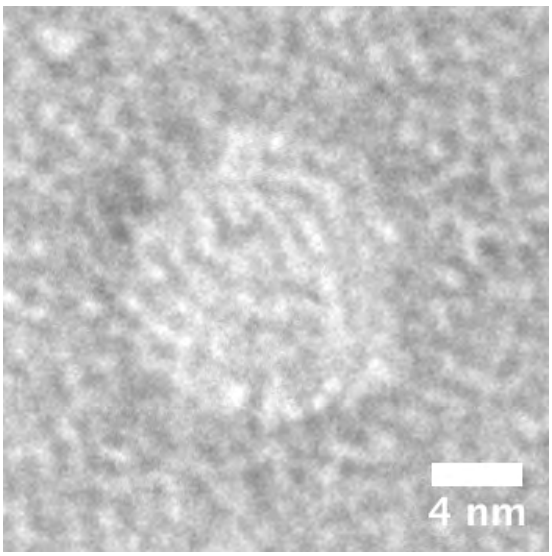

(b) TEM

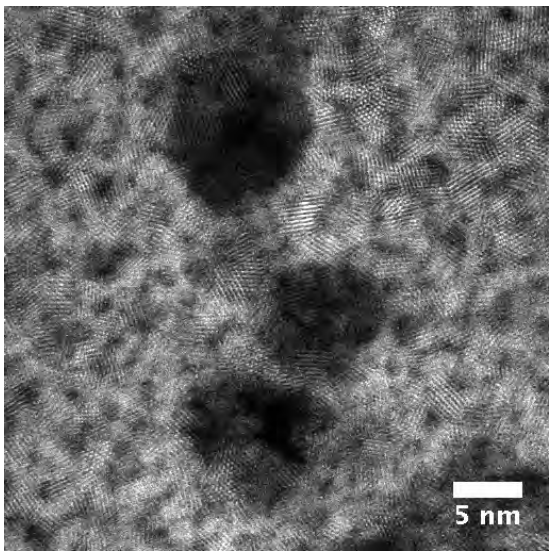

(c) Aberration corrected HAADF-STEM

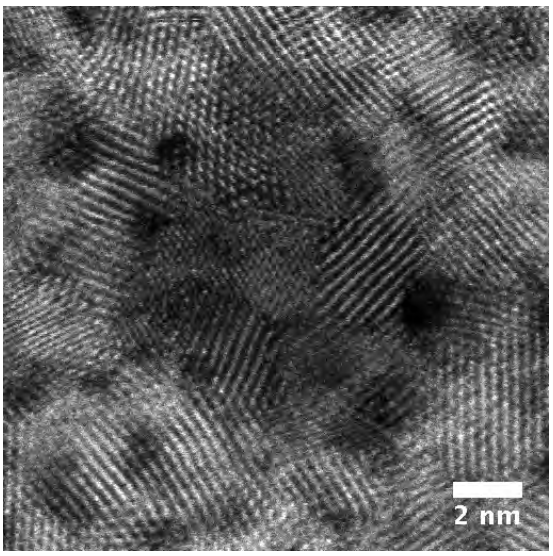

(d) Aberration corrected HAADF-STEM

Figure 6.5: Difference between negative stain in TEM and STEM mode. In the high resolution, aberration corrected STEM images it can be seen that the negative stain atoms mask structure in the sample.

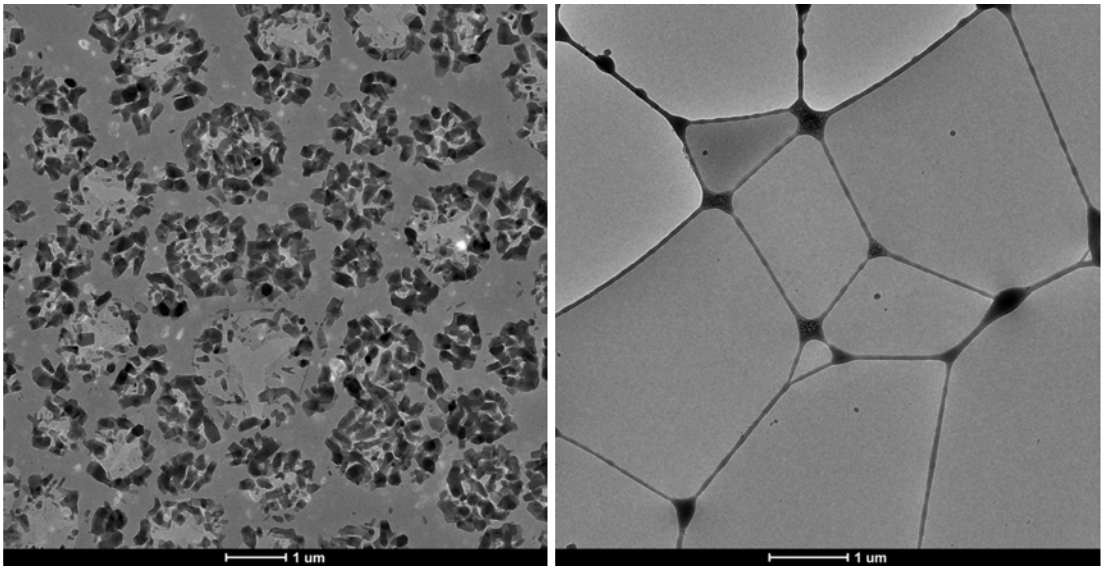

(a) Crystalline Ice (b) Vitreous Ice

Figure 6.6: Both crystalline and vitreous ice films can be formed, vitreous ice preserves the sample without structural damage.

Crystalline vs Vitreous Ice

For the cryo-TEM studies it was necessary to produce vitreous ice. This was relatively straight forward for this sample, with almost all frozen grids having some areas of vitreous ice. Figure 6.6 demonstrates the difference between the two types of ice, with crystalline being recognisable from the large dark crystals. Vitreous is a more even, opaque thin film, within which the preserved discs should reside.

6.4.2 Imaging of 'Empty' SMALPs

Negative Stain TEM

SMALPs can be formed with just lipids and polymer under the same pH reaction in the absence of membrane proteins. These 'empty' nano-discs still form and so were imaged in order to assess any changes in morphology by comparison with discs encapsulating membrane proteins. Imaging of these 'empty' SMALPs has been performed using negative stain as described in chapter 3. Representative images can be seen in Figure 6.7 where roughly circular features with

a broad size distribution can be seen. Some features are more 'rod-like' in shape, presumably disc lying on their side during staining.

The diameter distribution of 56 particles was measured, assuming a circular morphology and plotted in a histogram, which can be found in figure 6.8. The discs are not mono-disperse in size, with diameters ranging from 8 to 23 nm with a mean value of 14nm. However, there are two prominent peaks in the distribution, at 11.1 ($\pm$ 3.3)and 16.0 ($\pm$ 3.0) nm. It is not clear whether these are preferential sizes, or simply indicative of the sample preparation procedure which is not precise, in that no size-selection is performed. It also agrees with previous work performed by collaborators [16], who found an average diameter of 10.2nm for the nano-discs, using TEM.

Cryo TEM

The same sample was then plunge frozen and imaged using methods described in chapter 3. This enables images to be taken of the nano-discs in a hydrated environment, i.e. as close to physiological conditions as you can get in the electron microscope.

It was relatively straight forward to produce vitreous ice from this sample, in most grids it was possible to find an area of clear ice rather than the crystalline ice. However due to the size of the nano-disc and the limited spatial resolution of this technique, locating and imaging on the 'search' mode was challenging and time-consuming.

Figure 6.9 shows images of 'empty' SMALPs suspended in vitreous ice. It can be seen that they have a similar shape to that found by negative stain TEM. The diameter of 47 discs was measured and it can be seen again in figure 6.10 that there is a variation of size, with the smallest diameter being 10.6nm and the largest 24nm. The mean diameter was 16.2 $\pm$ 2.8 nm, which is larger in comparison to the mean diameter found by negative stain. This is the opposite to what one would expect, as negative staining is normally accepted to increase the size of fea-

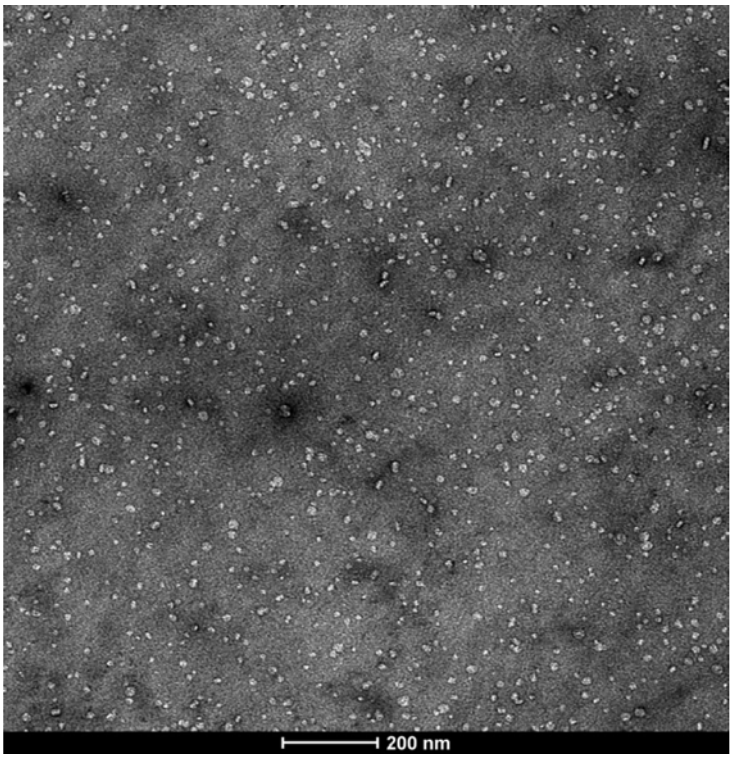

(a)

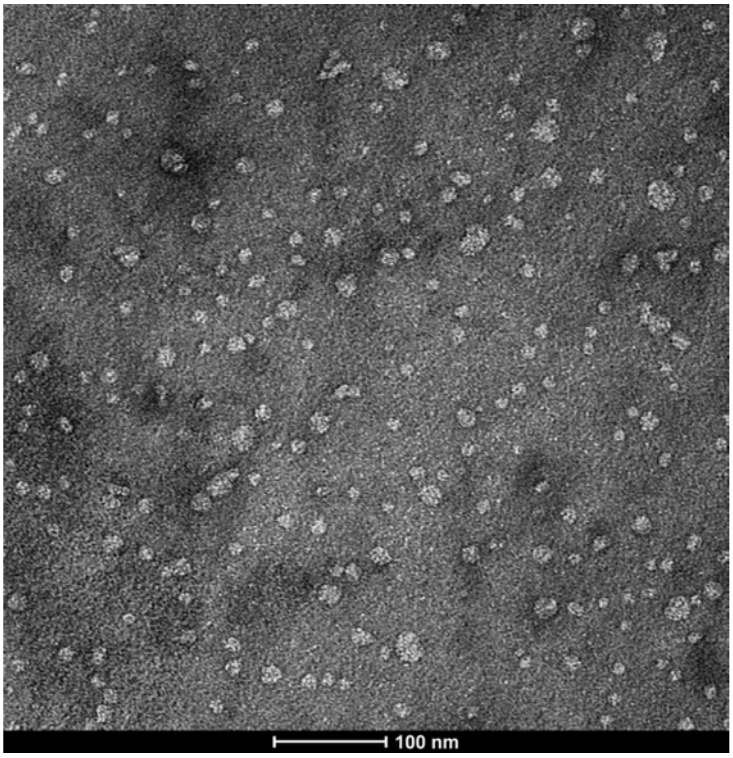

(b)

Figure 6.7: Negative stain TEM of empty SMALPs revealed disc like features of a reasonably broad size distribution.

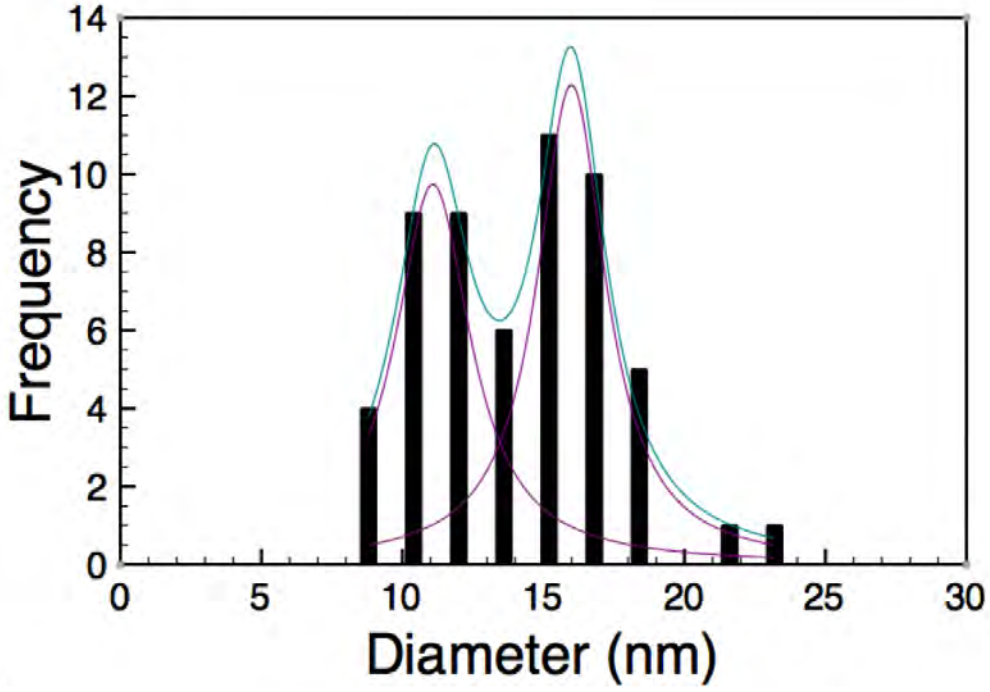

Figure 6.8: Diameter distribution of 56 'empty' SMALPs measured using negative stain TEM. It can be seen there is a variation of size, with the smallest value being 8.4nm and the largest 23.3nm. The mean diameter was 14.1 $\pm$ 3.3 nm, however there are two peaks in the distribution at 11.1 ($\pm$ 3.3)and 16.0 ($\pm$ 3.0) nm.

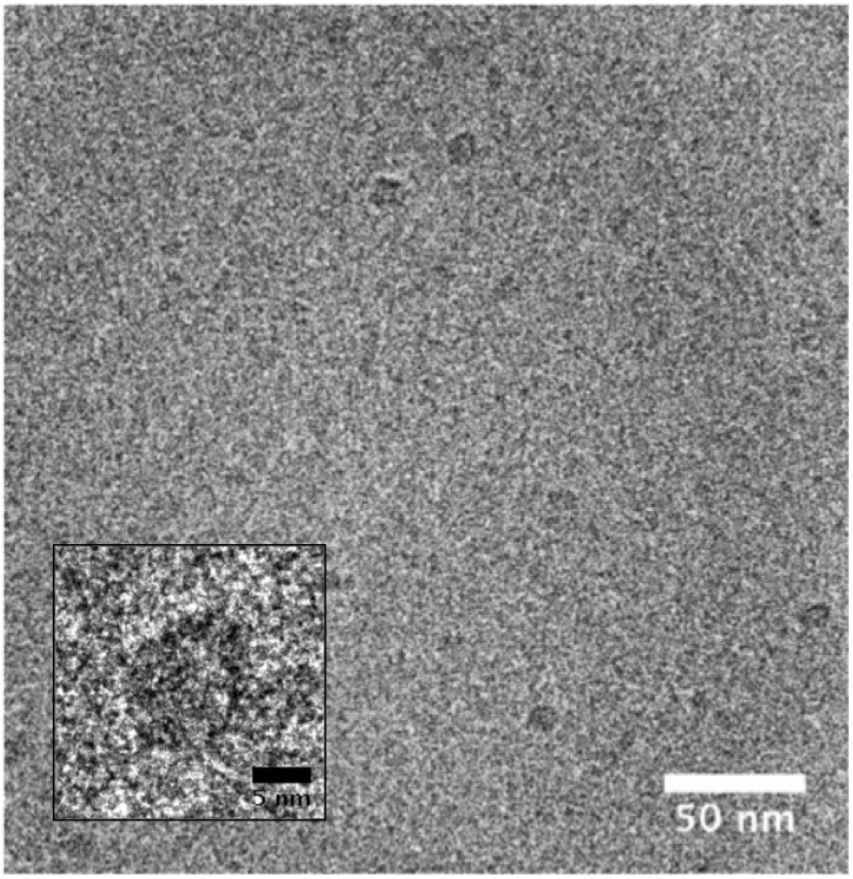

Figure 6.9: Cryo-TEM of hydrated 'empty' SMALPs, a single disc is shown in the inset. This low contrast image is typical of cryo-TEM.

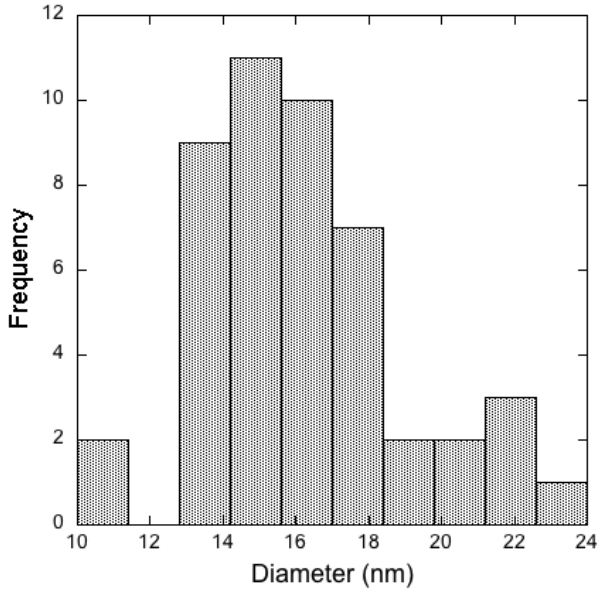

Figure 6.10: Diameter distribution of 'empty' SMALPs. It can be seen there is a variation of size, with the smallest value being 10.6nm and the largest 24nm. The mean diameter was 16.2 $\pm$ 2.8 nm

tures by around 2nm, as discussed in Chapter 2. This suggests that dehydration upon entry to the electron microscope column has a more significant effect on the size of biological samples than negative staining. Cryo-TEM avoids this since the vitrified sample is maintained in the hydrated state.

6.4.3 Imaging of SMALPs + PagP

Negative Stain TEM

Dynamic light scattering has been used to measure a size increase when a membrane protein is encapsulated by the disc [16], as discussed above. However, this technique cannot assess shape and so TEM offers a unique ability to do this. SMALP + PagP samples were prepared and grids were negatively stained as discussed in chapter 3.

Figure 6.11 shows negative stain TEM images of SMALP nanodiscs containing a single PagP

protein. A distinct morphology change can be seen between the empty SMALPs in figure 6.7 and the SMALPs containing the PagP protein. There are two types of structure seen in Figure 6.11, smaller discs and larger 'doughnut-like' features. This indicates that the protein inclusion influences both the size and shape of the nanodisc. The diameters of 23 'discs' and 25 'doughnuts' are plotted in histograms in figure 6.12. It can be seen that the distribution of the 'disc' diameter has two prominent peaks at at 10.2 ($\pm$ 2.3)and 13.9 ($\pm$ 1.6) nm whereas the 'doughnuts' have a single peak around at 27.8 ($\pm$ 5.2) nm, ie roughly 3 times larger. The mean diameter of the discs is 11.7 $\pm$ 2.6 nm which is comparable to the empty value found in the previous section.

This 'doughnut-like' morphology was never seen when imaging 'empty' SMALPs and so it can be concluded that the change is most probably a result of the inclusion of the PagP protein. However, the existence of the discs that are similar in size to the 'empty' SMALPs suggests that either the purification in the Ni-NTA column is not effective or the interaction of the stain with the protein itself is causing changes in the conformation.

Cryo TEM

The same sample was then plunge frozen and imaged using methods described in chapter 3, example images can be found in figure 6.13. If the images found in figure 6.13 are compared with those in figure 6.7 it can be seen there is a distinct morphology change between empty and filled SMALPs.

It is notable that the doughnut structures observed in the negative stain images (figure 6.11) are not seen in the cryo-TEM images. This suggests that the differing sample preparation processes profoundly influence the resulting imaged structure. In particular, that negative stain and drop casting onto a substrate may cause the formation of doughnut structures and that this is not the structure of the protein as it would be in solution. This illustrates the importance of cryo-TEM

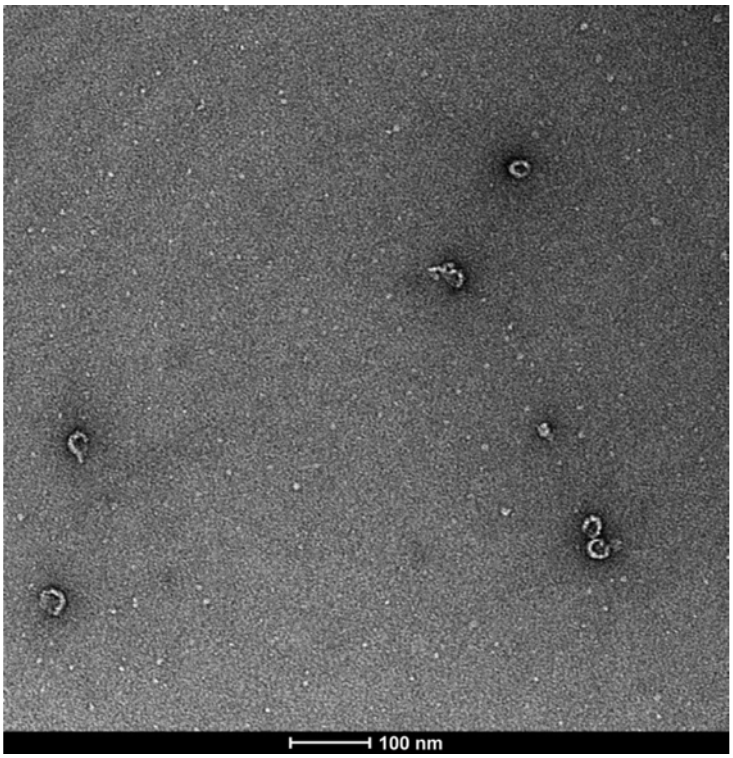

(a)

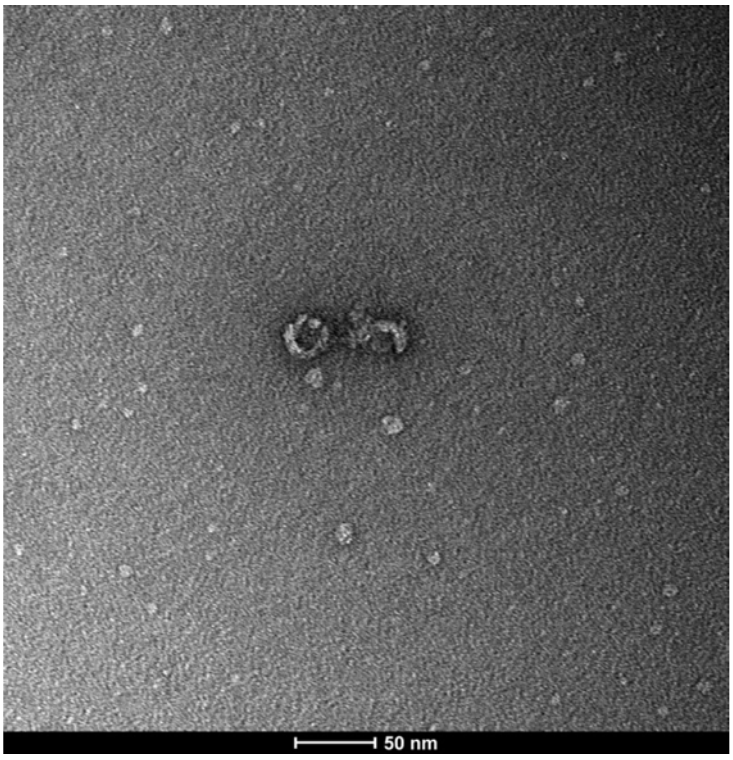

(b)

Figure 6.11: Negative stain TEM of SMALP + PagP protein. A distinct morphology change can be seen, with discs and 'doughnut-like' features clearly visible.

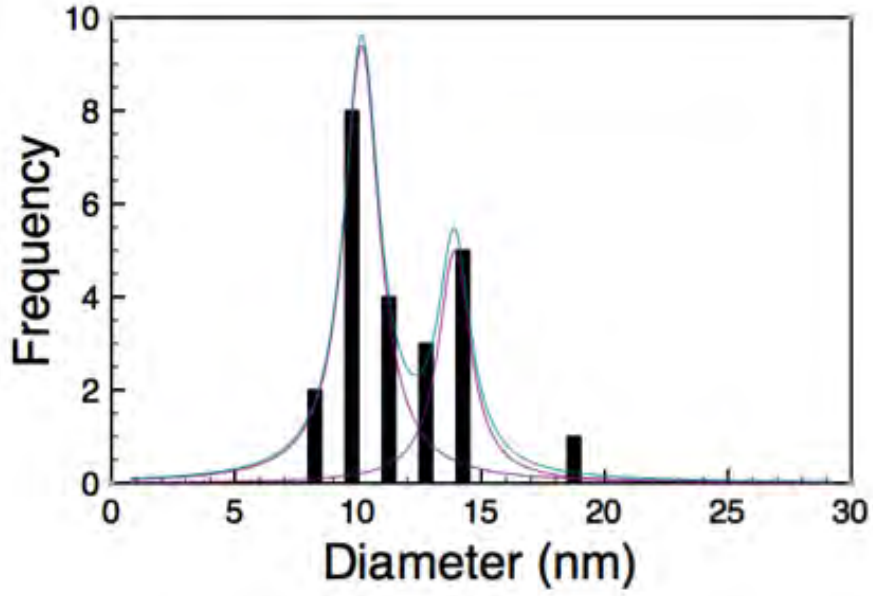

(a) Disc diameter (mean 11.7 $\pm$ 2.6 nm)

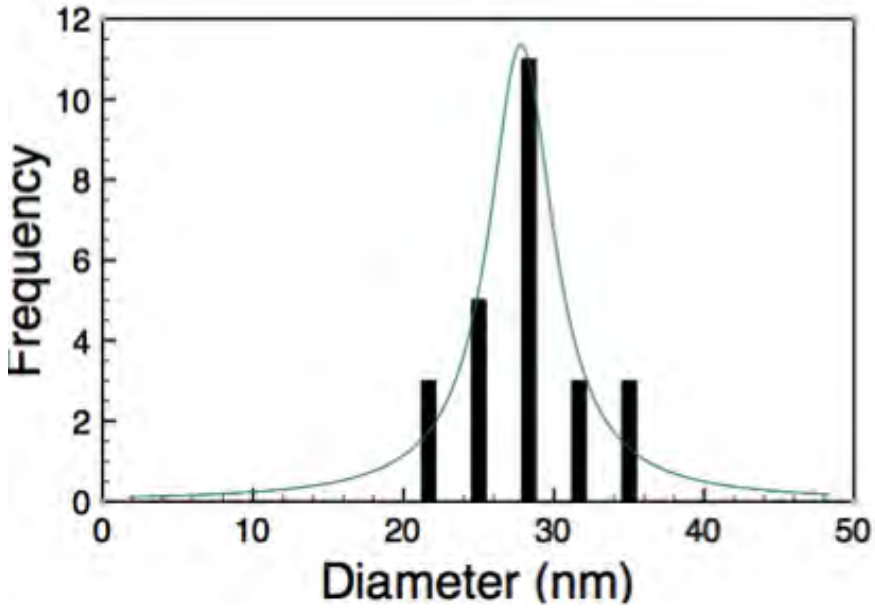

(b) Doughnut diameter (28 $\pm$ 3.9 nm)

Figure 6.12: Histograms comparing size distributions between the 'discs' and the 'doughnuts' seen in Figure 6.11. A significant difference in diameter is observed between the two morphologies. The distribution of the 'disc' diameter has two prominent peaks at at 10.2 ($\pm$ 2.3)and 13.9 ($\pm$ 1.6) nm whereas the 'doughnuts' have a single peak around at 27.8 ($\pm$ 5.2) nm

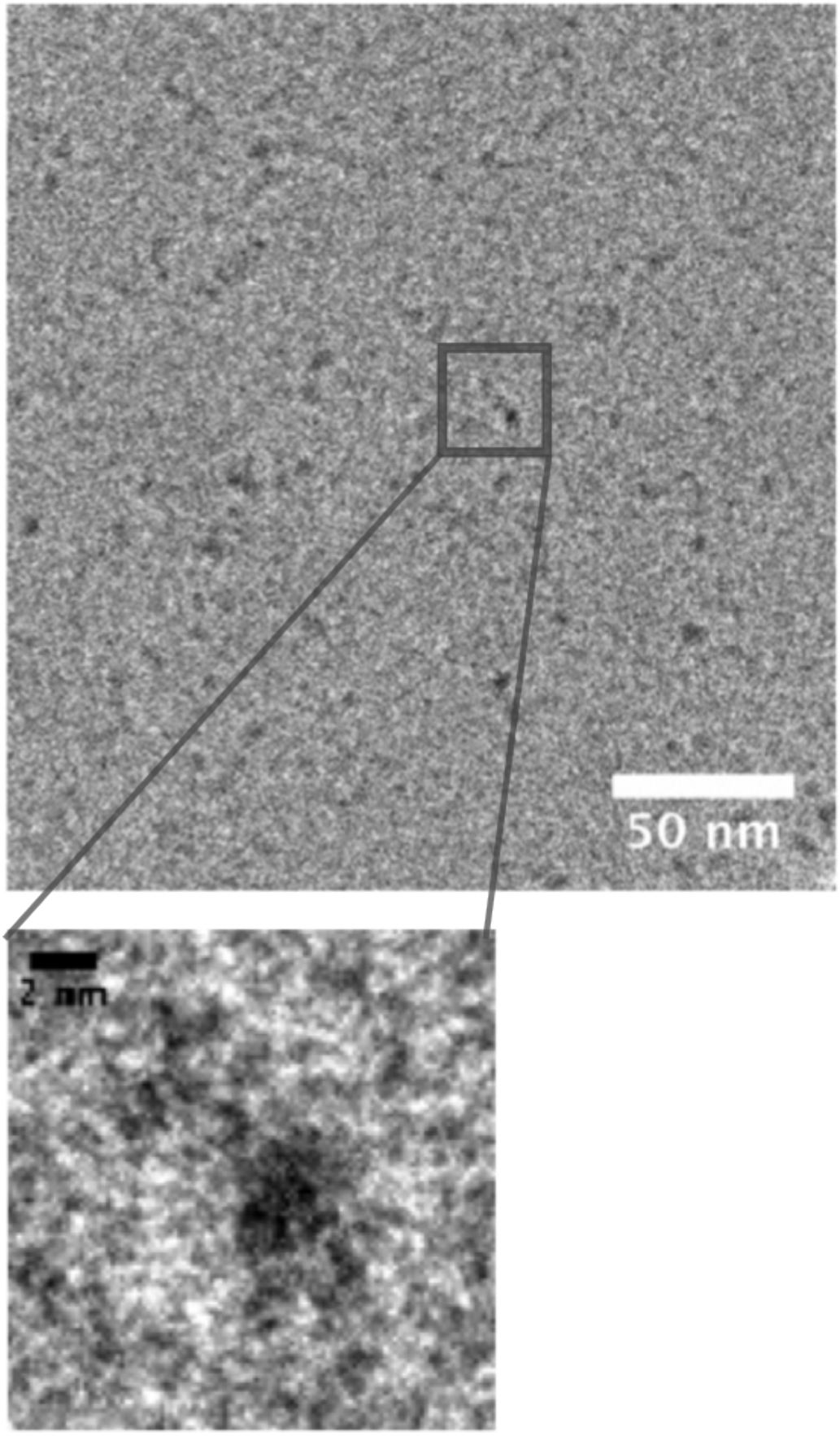

Figure 6.13: Cryo-TEM of SMALP nano-disc with incorporated PagP protein.

in revealing structures as near as possible to those seen in solution.

6.4.4 Imaging of SMALPs + PagP + NanoGold Label

In order to understand the system more thoroughly and keeping the aim of imaging a single protein within a SMALP in mind, gold labelling was used as an imaging aid. This was performed using Ni-NTA Nanogold (Nanoprobes inc.) of 5nm diameter. These gold nanoparticles are surrounded by the Ni-NTA ligand which will selectively bind to his tags within the protein. Since the PagP protein contains one his tag, this allows one gold particle per protein and therefore one per disk. In figure 6.14 an image of the SMALP+PagP incubated with Ni-NTA-Nanogold is presented.

It can be seen that the gold particle does associate with the discs, however there are some gold particles that are not near a disc or discs without a gold particle. This could indicate problems with either the nano-gold rinsing protocol or empty SMALP purification.

In figure 6.14 the glow discharged SMALP can be seen, with a clear localisation of gold particles around the doughnut features. This supports the hypothesis that the doughnut structure is as a result of protein incorporation to the nano-disc.

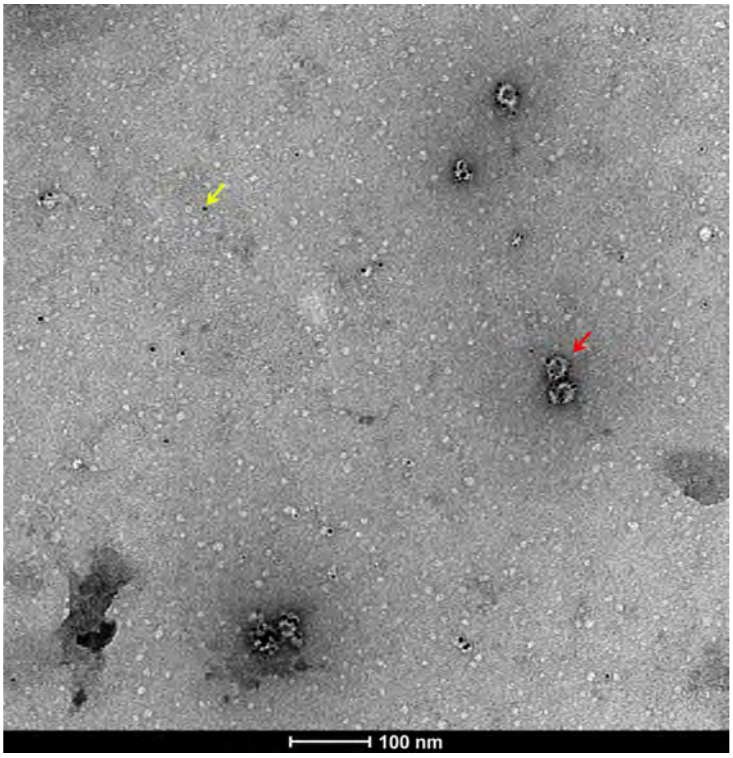

(a)

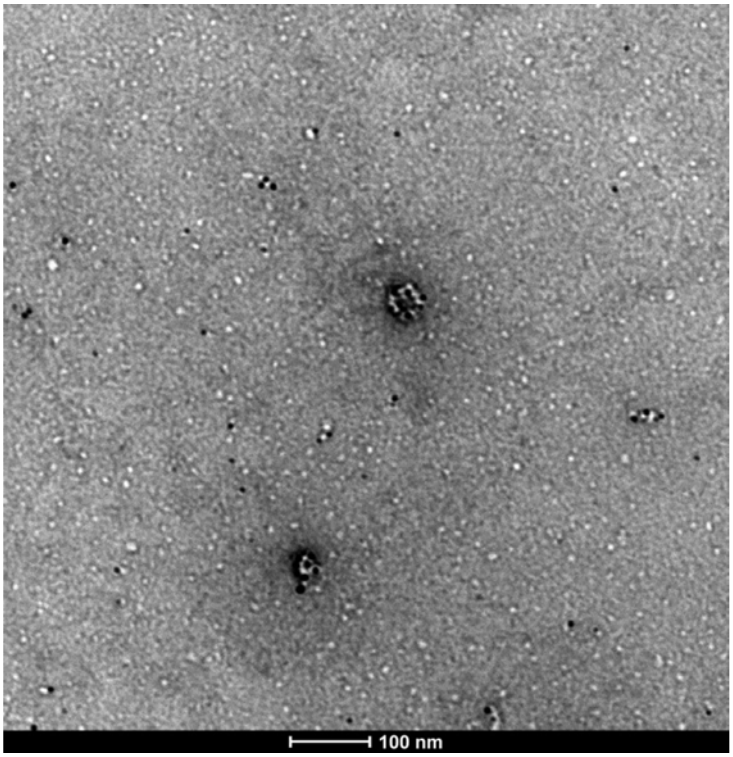

(b)

Figure 6.14: Negative stain of SMALP + PagP protein + Ni-NTA-Nanogold. The gold particles are highlighted with the yellow arrow, the PagP + SMALP + nanogold are highlighted with the red arrow.

6.5 Conclusions and Future Work

TEM imaging has been performed on self-assembled nano discs that can be used for solubilising membrane proteins. Successful sample preparation and imaging protocols were developed in order to perform negative stain TEM and reveal a disperse sizing with a mean diameter of 14.1 ± 3.3 nm, within which a protein can reside.

The outer membrane protein PagP has been imaged when encapsulated within a self-assembled nanodisc using negative stain and cryo TEM. In the negatively stained images a change in morphology has been observed between the empty disc and that encapsulating the PagP protein. When the PagP protein is incorporated, there is a doughnut like shape that is not seen in the empty SMALP images. This suggests the protein is indeed inducing morphological change in the discs when it is incorporated inside them. However, this doughnut morphology is not observed in the cryo-TEM imaging, but rather a different morphology again. This highlights the difference in imaging with negative stain and cryo TEM and suggests that the stain may be interacting with the protein containing nanodiscs to change the morphology from that found in solution.

Nanogold attachment has been used to enhance contrast and confirm whether protein is present in the disc. It was seen that with PagP present the gold attaches to the 'doughnut' shapes much more frequently than the discs. This is further evidence that the protein does successfully reside in the nano-disc, inducing a morphology change as it does so.

Cryo-TEM procedures need to be refined in order to gain better quality samples and thus better consistency in the image quality. This would allow more in depth, statistically significant studies to be performed or perhaps even single particle experiments to determine the three dimensional structure of the discs and protein residing within. The draw back to single particle studies would be heterogeneity in the structure of the discs within a sample set, which has been demonstrated in this work by the variation in the mean diameter.

An alternative method to obtain a three dimensional view of a disc incorporating a protein would be cryo-tomography of a single disc, avoiding averaging images of many discs and therefore allowing for any heterogeneity in the sample. The drawback to this technique is the beam damage induced by multiple projections taken through the same disc. This would be challenging to overcome and would involve minimising the time spent acquiring each projection whilst maintaining image contrast. However, single particle cryo-tomography has been demonstrated in the literature, as discussed in Chapter Two and three dimensional imaging in the hydrated state could provide deeper insight into the position and orientation of the protein within the disc.

References

[1] U. H. N Durr, M. Gildenberg, and A. Ramamoorthy. The magic of bicelles lights up membrane protein structure. *Chemical reviews*, 112(11):6054–6074, 2012.

[2] A. Elofsson and G. von Heijne. Membrane protein structure: prediction versus reality. *Annu. Rev. Biochem.*, 76:125–140, 2007.

[3] P. M. Hwang, W-Y Choy, E. I. Lo, L. Chen, J. D. Forman-Kay, C. R. H Raetz, G. G. Privé, R. E. Bishop, and L. E. Kay. Solution structure and dynamics of the outer membrane enzyme PagP by NMR. *Proceedings of the National Academy of Sciences*, 99(21):13560–13565, 2002.

[4] R. E. Bishop, H. S. Gibbons, T. Guina, M. S. Trent, S. I. Miller, and C. R. H. Raetz. Transfer of palmitate from phospholipids to lipid A in outer membranes of gram-negative bacteria. *The EMBO journal*, 19(19):5071–5080, 2000.

[5] A. Aderem and R. J. Ulevitch. Toll-like receptors in the induction of the innate immune response. *Nature*, 406(6797):782–787, 2000.

[6] R. A. Engh and R. Huber. Accurate bond and angle parameters for x-ray protein structure refinement. *Acta Crystallographica Section A: Foundations of Crystallography*, 47(4):392–400, 1991.

[7] A. M. Seddon, P. Curnow, and P. J. Booth. Membrane proteins, lipids and detergents: not just a soap opera. *Biochimica et Biophysica Acta (BBA)-Biomembranes*, 1666(1):105–117, 2004.

[8] O. F. Lange, P. Rossi, N. G. Sgourakis, Y. Song, H-W Lee, J. M. Aramini, A. Ertekin, R. Xiao, T. B. Acton, G. T. Montelione, et al. Determination of solution structures of proteins up to 40 kDa using CS-Rosetta with sparse nmr data from deuterated samples. *Proceedings of the National Academy of Sciences*, 109(27):10873–10878, 2012.

[9] A. Arora, F. Abildgaard, J. H. Bushweller, and L. K. Tamm. Structure of outer membrane protein a transmembrane domain by NMR spectroscopy. *Nature Structural & Molecular Biology*, 8(4):334–338, 2001.

[10] P. Bernadó, E. Mylonas, M. V. Petoukhov, M. Blackledge, and D. I. Svergun. Structural characterization of flexible proteins using small-angle x-ray scattering. *Journal of the American Chemical Society*, 129(17):5656–5664, 2007.

[11] G. L. Hura, A. L. Menon, M. Hammel, R. P. Rambo, F L Poole I., S. E. Tsutakawa, F. E. Jenney Jr, S. Classen, K. A. Frankel, R. C. Hopkins, et al. Robust, high-throughput solution structural analyses by small angle X-ray scattering (SAXS). *Nature methods*, 6(8):606–612, 2009.

[12] B. J. Berne and R. Pecora. *Dynamic light scattering: with applications to chemistry, biology, and physics*. Courier Dover Publications, 2000.

[13] J. Moradian-Oldak, M. L. Paine, Y. P. Lei, A. G. Fincham, and M. L. Snead. Self-assembly properties of recombinant engineered amelogenin proteins analyzed by dynamic light scattering and atomic force microscopy. *Journal of structural biology*, 131(1):27–37, 2000.

[14] J-L Popot. Amphipols, nanodiscs, and fluorinated surfactants: three nonconventional approaches to studying membrane proteins in aqueous solutions. *Annual review of biochemistry*, 79:737–775, 2010.

[15] T. H. Bayburt and S. G. Sligar. Membrane protein assembly into nanodiscs. *FEBS letters*, 584(9):1721–1727, 2010.

[16] T. J. Knowles, R. Finka, C. Smith, Y. P. Lin, T. Dafforn, and M. Overduin. Membrane proteins solubilized intact in lipid containing nanoparticles bounded by styrene maleic acid copolymer. *Journal of the American Chemical Society*, 131(22):7484–7485, 2009.

[17] M. Jamshad, Y. P. Lin, T. J. Knowles, R. A. Parslow, C. Harris, M. Wheatley, D. R. Poyner, R. M. Bill, O. R. T. Thomas, M. Overduin, et al. Surfactant-free purification of membrane proteins with intact native membrane environment. *Biochemical Society Transactions*, 39(3):813, 2011.

[18] S. Rajesh, T. Knowles, and M. Overduin. Production of membrane proteins without cells or detergents. *New Biotechnology*, 28(3):250–254, 2011.

[19] P. K. Vinson, Y. Talmon, and A. Walter. Vesicle-micelle transition of phosphatidylcholine and octyl glucoside elucidated by cryo-transmission electron microscopy. *Biophysical journal*, 56(4):669–681, 1989.

[20] H. Katayama, J. Wang, F. Tama, L. Chollet, E. P. Gogol, R. J. Collier, and M. T. Fisher. Three-dimensional structure of the anthrax toxin pore inserted into lipid nanodiscs and lipid vesicles. *Proceedings of the National Academy of Sciences*, 107(8):3453–3457, 2010.

[21] T. Althoff, D. J. Mills, J-L Popot, and W. Kühlbrandt. Arrangement of electron transport chain components in bovine mitochondrial supercomplex I1III2IV1. *The EMBO journal*, 30(22):4652–4664, 2011.

[22] U. Aebi and T. D. Pollard. A glow discharge unit to render electron microscope grids and other surfaces hydrophilic. *Journal of electron microscopy technique*, 7(1):29–33, 1987.

[23] J. Dubochet, M. Ducommun, M. Zollinger, and E. Kellenberger. A new preparation method for dark-field electron microscopy of biomacromolecules. *Journal of ultrastructure research*, 35(1):147–167, 1971.

Chapter 7

Conclusions and Outlook

Electron microscopy is a unique technique, allowing detailed structural analysis of individual molecules. Advances in techniques such as aberration-corrected STEM and cryo TEM have demonstrated that significant results can be gained. Three different biological systems have been studied using electron microscopy techniques, ranging from atomic structure measurements of ferritin cores to imaging of hydrated membrane proteins encapsulated by nano-discs.

HAADF-STEM of Ferritin

Aberration corrected HAADF-STEM has been used to measure the iron content of ferritin using novel size-selected clusters as a mass balance. This is, to the authors knowledge, the first example of application of this mass measurement technique to a biological molecule. The quantitative studies have not only provided insight into the iron binding states of ferritin, but also the preferential loading.

In the future, sequential iron loading of ferritin coupled to continuous mass measurement should be performed, to assess any preferential binding at certain loading states. The technique could also be applied on ferritin 'from the clinic', i.e. as purified from the blood samples of patients, for example those suffering from anaemia. The mass measurement technique could also be

extended to other metal containing proteins, such as transferrin. The major advantage of this compared to existing mass measurement techniques would be that the shape of a molecule can be cross-referenced with its mass.

STEM Characterisation of a Novel, Alginate Based Cancer Therapy

A prospective alginate based therapy for colorectal cancer has been further investigated by the imaging and characterisation of iron nanopaticles formed in *physiological conditions* using ac-STEM and EDX for the first time. The verification of iron nanoparticle formation has enabled further research into the transport and ultimate fate of these particles *in vivo*.

In the future, the structures formed using alginates with varying m to g ratios could be compared to ascertain whether there are any nanoparticle morphology changes due to the use of different alginates. A similar study could also be performed with varying length of alginate polymer, to assess the effect of this property. This is particularly pertinent as cell studies are ongoing focusing on several alginate candidates.

The application of aberration-corrected STEM to biological molecules is rare to date, and the studies presented here confirm its relevance, particularly where metal binding is concerned. This provides motivation for more use of ac-STEM in the biological sciences, with applications to, for example, such as metalloproteins, ultra-small immuno gold labelling and metal ion transport studies.

TEM of Membrane Proteins Encapsulated by Nano-Discs

A combination of negative stain TEM, cryo-TEM and gold labelling has been used to localise single proteins encapsulated by membrane-mimicking nano-discs. This has also allowed structural studies of the morphological changes induced by protein inclusion, which will potentially

lead to better understanding of the system.

In the future, cryo-TEM procedures for imaging hydrated SMALP nanodiscs could be refined to allow more consistent image quality reducing the reliance on negative stain TEM, which could interact with the sample. Three dimensional imaging could also be performed on the nano-discs / membrane protein samples to elucidate detailed, perhaps even near-atomic level, structure. Cryo-TEM tomography would require detailed computational reconstructions and well defined cryo-TEM images whilst minimising beam damage to the sample.

Overall, the relevance of advanced electron microscopy techniques to the study of biological molecules has been proven, both in terms of fundamental structural analysis and clinically relevant systems.